

NOVEL NANOSTRUCTURED METAL OXIDE MATERIALS FOR WATER TREATMENT
AND ADVANCED RECHARGEABLE BATTERIES

by

Jingwan Huo

A Dissertation Submitted in
Partial Fulfillment of the
Requirements for the Degree of

Doctor of Philosophy
in Engineering

at

The University of Wisconsin-Milwaukee

May 2018

ABSTRACT

NOVEL NANOSTRUCTURED METAL OXIDE MATERIALS FOR WATER TREATMENT AND ADVANCED RECHARGEABLE BATTERIES

by

Jingwan Huo

The University of Wisconsin-Milwaukee, 2018
Under the Supervision of Professor Chris Yuan and Professor Yin Wang

Clean water and energy shortage problems are pressing issues human facing today, as they not only cause many problems including public health and environmental deteriorations, but also threaten sustainable development of human society. It is urgent and critical to address and solve these problems.

Among various technologies, photocatalysis and adsorption applications in water and wastewater catch a lot of attention in recent years, for their low costs and for no requirement for chemical additives or thermal inputs. Photodegradation of contaminants by nanomaterials as catalysts is an important method in water and wastewater treatment. The adsorption is mainly through complexation between dissolved metals and the oxygen in metal oxides. Nano-adsorbents offer significant improvement with extremely high specific surface area and associated sorption sites, short intraparticle diffusion distance, tunable pore size and surface chemistry. Metal oxides such as iron oxide, titanium oxide, aluminum oxide and zirconium oxide are effective, low cost adsorbents for heavy metals and radionuclides.

Same as the situation of clean water supply, energy shortage is another urgent problem. As energy demand and consumption of conventional fossil fuel increase constantly, the resulting energy crisis and environmental problems caused by combustion of fossil fuel drive us to look for

more sustainable energy sources. Renewable energy resources appear to be an effective and promising solution. To overcome the variability for better renewable energy utilization, suitable energy storage devices are required.

Nanotechnology and nanomaterials are actively pursued to both improve existing technologies and develop new technology. TiO₂ nanomaterials have been intensively investigated in various applications, as photoelectrode, catalyst, sensor, energy storage. TiO₂ nanomaterials possess fascinating properties such as biological and chemical inertness, photostability, low cost, nontoxicity and superior oxidization ability. However, the wide electronic band gap and fast electron recombination rate limit the photocatalytic application and energy conversion efficiency of TiO₂ nanomaterials. Though TiO₂ can retain capacity at fast charge/discharge rates, and it is also electrochemical stable in common electrolytes and lack of harmful solid-electrolyte interfacial layer, the capacity of TiO₂ is relatively low. Zirconium oxide has valuable chemical and physical properties, including high melting point, mechanical and thermal resistance, low electrical conductivity, biocompatibility, chemical inertness (resistant to oxidant agent and acids/bases, non-toxic, and not dissolvable in water) is a widely used inorganic material. ZrO₂ is practical applied in fuel-cell technology, catalyst or catalyst support, oxygen sensor, thermal-barrier coatings and so on.

In this study, different modification strategies are carried out to improve the performance of TiO₂ and ZrO₂ in water treatment and energy storage applications. There are three objectives in this proposal. The first objective is to demonstrate high-efficiency photocatalysts using innovative hybrid nanostructures that consist of Pt nanoparticles and rGO co-modified three-dimensionally ordered microporous (3DOM) TiO₂. The excellent charge-separation property and high adsorption capacity of rGO increased the charge carrier lifetime and affinity to organic molecules. The

introduction of Pt nanoparticles increased spectral response to visible light through surface plasmon resonance and suppressed charge recombination. This study entails the synthesis and characterization of Pt/rGO-TiO₂ for application in methyl orange photodegradation. The second objective of this study is to demonstrate high-performance Lithium-ion battery electrode using hybrid nanomaterials consist of Fe₂O₃ nanospindles assembled on 3DOM TiO₂ with carbon coating. The carbon coated TiO₂@Fe₂O₃ material showed good electrochemical performance with exhibits a large reversible capacity about 570 mAh g⁻¹, which is about four times of the reversible capacity of 3DOM TiO₂. In addition to the high reversible capacity, the obtained material also exhibits good cycle performance and superior rate capacity. This rationally designed composite benefits from both good stability of TiO₂, high capacity of Fe₂O₃, and good electron conductivity of carbon. The third objective is to study zirconium modified clays as adsorbents of phosphate from aqueous solution. Comparing three clays, zirconium modified MT (2:1), VT (2:1) and KT (1:1) exhibit different structure and surface properties, and thus performance differently toward phosphate adsorption. The adsorption kinetics data of phosphate on zirconium modified clays could be well described by the pseudo-second-order model, indicating that the adsorption was through chemisorption. The experimental equilibrium data of phosphate adsorption on modified clays were fitted better by Langmuir isotherm model than the Freundlich, implying monolayer adsorption. The effect of water chemistry (pH, co-existing anions, ionic strength, DOC) was also studied. These low-cost, abundant and effective are easily synthesized and have potential for practical wastewater treatment.

© Copyright by Jingwan Huo, 2018
All Rights Reserved

TABLE OF CONTENTS

LIST OF FIGURES	viii
LIST OF TABLES	x
LIST OF ABBREVIATIONS	xi
ACKNOWLEDGEMENTS	xiii
CHAPTER 1 Introduction and research objectives.....	1
1.1 Research background	1
1.2 Water treatment through photocatalysis and adsorption	3
1.3 Lithium ion batteries	5
1.4 Summary and literature review	6
1.5 Objectives of study.....	11
CHAPTER 2 Pt/rGO-TiO ₂ photocatalyst for degradation of MO	14
2.1 Introduction.....	14
2.2 Experimental	17
2.3 Results and discussion.....	21
2.4 Conclusion.....	33
CHAPTER 3 Carbon coated Fe ₂ O ₃ /TiO ₂ composite as anode material for LIBs	35
3.1 Introduction	35
3.2 Experimental	37

3.3	Results and discussion.....	39
3.4	Conclusion.....	52
CHAPTER 4 Adsorption removal of phosphorus by zirconium modified clays.....		53
4.1	Introduction.....	53
4.2	Experimental.....	57
4.3	Results and discussion.....	60
4.4	Conclusion.....	75
CHAPTER 5 Summary of research work and proposed future work.....		77
5.1	Summary of research work.....	77
5.2	Future work.....	78
References.....		80
Appendix: Supporting information for Chapter 2.....		92
Curriculum Vitae.....		94

LIST OF FIGURES

Figure 1-1 (a) Global water demand in 2000 and 2050 and (b) predicted water scarcity and stress in 2025

Figure 1-2 (a) World energy consumption, 1990-2040, (b) comparative primary energy consumption over the past 15 years

Figure 2-1 Schematic illustration of fabrication processes of 3DOM TiO₂ modified with Pt NPs and rGO

Figure 2-2 SEM images of (a) 3DOM TiO₂, (b) Pt-TiO₂, (c) rGO-TiO₂, (d) Pt/rGO-TiO₂

Figure 2-3 (a)-(b) TEM images of Pt-TiO₂ with different magnifications and (c) HRTEM image of Pt-TiO₂

Figure 2-4 XRD patterns of as-prepared catalysts with 2 theta between (A) 10° and 70° and (B) 37° to 50°; Raman spectra of as-prepared catalysts with wavelength (C) 250-1800 cm⁻¹ and (D) 1100-1800 cm⁻¹. a) TiO₂, b) Pt-TiO₂, c) rGO-TiO₂, d) Pt/rGO-TiO₂

Figure 2-5 Fitted XPS spectra (A) O 1s, (B) C 1s, (C) Ti 2p and (D) Pt 4f of Pt/rGO-TiO₂ composite

Figure 2-6 UV-vis diffuse reflectance spectra (A) and Kubelka-Munk transformed reflectance spectra (B) of a) TiO₂, b) Pt-TiO₂, c) rGO-TiO₂, d) Pt/rGO-TiO₂. (A) shows simultaneously the absorbance spectra of 3DOM catalysts (left) and the reflectance spectrum of 3DOM TiO₂ with stop band maxima at 400 nm (right)

Figure 2-7 (A) Photocatalytic degradation curve and (B) kinetic curves of MO over different catalysts under visible light irradiation a) TiO₂, b) Pt-TiO₂, c) rGO-TiO₂, d) Pt/rGO-TiO₂

Figure 2-8 Recycling test of MO degradation over Pt/rGO-TiO₂ within 90 min visible light irradiation

Figure 2-9 Schematic illustration of charge separation and transportation in Pt/rGO-TiO₂ photocatalyst under light illumination.

Figure 3-1 Schematic illustration of fabrication processes of carbon coated TiO₂@Fe₂O₃ material

Figure 3-2 SEM images of (a)-(b) 3DOM TiO₂, (c)-(d) TiO₂@Fe₂O₃, (e)-(f) carbon coated TiO₂@Fe₂O₃

Figure 3-3 (a) TEM image and (b) HRTEM image of TiO₂@Fe₂O₃, (c) TEM image and (d) HRTEM image of carbon coated TiO₂@Fe₂O₃

Figure 3-4 (a) XRD patterns of TiO₂, TiO₂@FeOOH and TiO₂@Fe₂O₃, (b) Raman spectrum of carbon coated TiO₂@Fe₂O₃

Figure 3-5 Fitted XPS spectra (a) Fe 2p, (b) Ti 2p, (c) C 1s and (d) O 1s of carbon coated TiO₂@Fe₂O₃ composite

Figure 3-6 CVs at a scan rate of 1 mV s⁻¹ for the first four cycles of (a) 3DOM TiO₂, (b) TiO₂@Fe₂O₃, (c) carbon coated TiO₂@Fe₂O₃ electrodes

Figure 3-7 Lithium-ion battery performance of 3DOM TiO₂, TiO₂@Fe₂O₃ and carbon coated TiO₂@Fe₂O₃. (a) comparative cycling performance, taken between 0.05-3V at a current density of 50 mA g⁻¹, (b) rate capacity of electrodes at different current densities from 50 mA g⁻¹ to 800 mA g⁻¹

Figure 3-8 Galvanostatic discharge/charge profiles of (a) 3DOM TiO₂, (b) TiO₂@Fe₂O₃, (c) carbon coated TiO₂@Fe₂O₃ electrodes at a constant current density of 50 mA g⁻¹

Figure 4-1 Diagrammatic sketch of the (a) tetrahedral sheet and (b) octahedral sheet

Figure 4-2 Classification of clays

Figure 4-3 SEM images of (a) MT, (b) Zr0.62-MT, (c) VT, (d) Zr0.62-VT, (e) KT, (f) Zr0.62-KT

Figure 4-4 XRD patterns of zirconium modified (a) MT, (c) VT, (e) KT between 2 theta 3-70° and (b) MT, (d) VT, (f) KT between 2 theta 3-20°

Figure 4-5 Zeta potentials of unmodified and zirconium modified clays

Figure 4-6 The adsorption equilibrium isotherm of phosphorus on zirconium modified clays at pH 7 and 25 °C. (a) MT, (b) VT, (c) KT (adsorbent dose 1g/L, pH 7, 25 °C)

Figure 4-7 The phosphorus uptake of zirconium modified clays with the change of contact time, (a) Zr/clay ratio 0.62 mmol/g, (c) Zr/clay ratio 1.24 mmol/g. The fitting curves by the pseudo-second-order rate model of the kinetic study (b) Zr/clay ratio 0.62 mmol/g, (d) Zr/clay ratio 1.24 mmol/g (adsorbent dose at 1g/L, pH 7, 25 °C)

Figure 4-8 Effect of pH on phosphorus adsorption by Zr0.62-MT (initial phosphorus concentration at 5 mg P/g, adsorbent dose at 1 g/L, 25 °C, contact time 24 h)

Figure 4-9 Effect of coexisting anions on the phosphorus adsorption by Zr0.62-MT with phosphorus concentration at 5 mg P/L, adsorbent dose at 1 g/L, pH 7, contact time 24 h

Figure 4-10 Effect of ionic strength on phosphorus adsorption by Zr0.62-MT, with phosphorus concentration at 5 mg P/L, adsorbent dose at 1 g/L, pH 7, contact time 24 h

Figure 4-11 Effect of humic acid concentration on phosphorus adsorption by Zr0.62-MT, with phosphorus concentration at 5 mg P/L, adsorbent dose at 1 g/L, pH 7, contact time 24 h

LIST OF TABLES

Table 4-1 Classification of clay minerals according to Grim

Table 4-2 Zeta potentials of unmodified and zirconium modified clays

Table 4-3 Langmuir and Freundlich isotherm constants for phosphorus adsorption on zirconium modified clays at pH 7 and T about 25 °C

Table 4-4 The kinetic model parameters for the adsorption of phosphorus on zirconium modified clays at pH 7 and T about 25 °C

LIST OF ABBREVIATIONS

3D	Three-dimensional
3DOM	Three-dimensionally order macroporous
ACAC	Acetylacetone
BE	Binding energy
CB	Conduction band
CCT	Colloidal crystals templating
CV	Cyclic voltammogram
CEC	Cations exchange capacity
DOC	Dissolved organic carbon
DRS	UV-vis diffused reflectance spectroscopy
EDCs	Endocrine disrupting compounds
E_g	Band gap energy
EIS	Electrochemical impedance spectroscopy
FCC	Face-centered-cubic
HA	Humic acid
HRTEM	High resolution transmission electron microscopy
ICP-OES	Inductively coupled plasma-optical emission spectroscopy
KT	Kaolinite
LIBs	Lithium-ion batteries
MMA	Methyl methacrylate
MO	Methyl orange
MT	Montmorillonite
NF	Nanofiltration
NOM	Natural organic matter

NPs	Nanoparticles
PMMA	Poly(methyl methacrylate)
PPCPs	Personal care products
PS	Polystyrene
rGO	Reduced graphene oxide
SEI	Solid-electrolyte interface
SEM	Scanning electron microscopy
SPR	Surface plasmon resonance
TEM	Transmission electron microscopy
UV	Ultraviolet
UV-vis	Ultraviolet-visible
VB	Valence band
VT	Vermiculite
XPS	X-ray photoelectron spectroscopy
XRD	X-ray diffraction

ACKNOWLEDGEMENTS

First, I would like to express my appreciation to my advisor, Dr. Chris Yuan for his guidance and support during my study. Dr. Yuan provides me the opportunity to study and work in UWM, where I have gained not only knowledge in labs and research, but also enhanced my skills in teaching students and cooperating with colleagues. Also, I want to thank my committee members, Dr. Yin Wang, Dr. Junhong Chen, Dr. Deyang Qu, Dr. Ben Church for their friendly guidance. Especially thank Dr. Yin Wang, my co-advisor, for the time and effort he spent on providing me guidance on conducting better research and for pursuing my degree.

I am grateful to all members in Dr. Yuan's group. Particularly, I thank Dr. Xianfeng Gao and Dr. Dongsheng Guan, for their help with experiment and all the discussion we had. Also, I want to thank Xiaopeng Min in Dr. Wang's lab, who offered a lot of help on experiment design and discussion. I would like to thank Mr. Donald Roberston for his assistance in TEM and HRTEM analyses, Dr. Heather A. Owen at the Biology Department for technical support with SEM analyses, and Mr. Patrick Anderson in School of Freshwater Science for water chemistry measurement.

Finally, I want to express my deepest love for my parents, they are always by my side and give me unconditional support and courage all the time. My best friends, Wen Zeng, Shuwen Tang, Weixi Shi, Xin Guan, Yue Huang, their company and friendship are fabulous during the years. The group of friends, Shiqi Chu, Mingguang Tuo, Yifei Zhang, Dongqing Shao, Haoyue Wu, Tianshu He, I feel so lucky to meet all of you, the conversations and friendship among us are fantastic and bring me so much courage and support. I hope all of you have bright future because you deserve it.

CHAPTER 1 Introduction and research objectives

1.1 Research background

Clean water supply is a major problem worldwide. As shown in Figure 1-1, the worldwide water demand is increasing from 2000 to 2050, and two-thirds of the world population will face water scarcity by 2025 [1, 2]. About half of the world's population (2.6 billion) lacks access to basic sanitation, and 1.1 billion people are using water without improved sources [3]. The shortage of clean water causes many problems including public health and environmental deteriorations. Furthermore, with increasing population and industrialization practices, the rate of contamination of water supplies has been accelerated, water pollution becomes more complex and difficult to remove, which amplifies the public and environmental problems [4-6]. There is an urgent need to provide effective and affordable water treatment in developing countries.

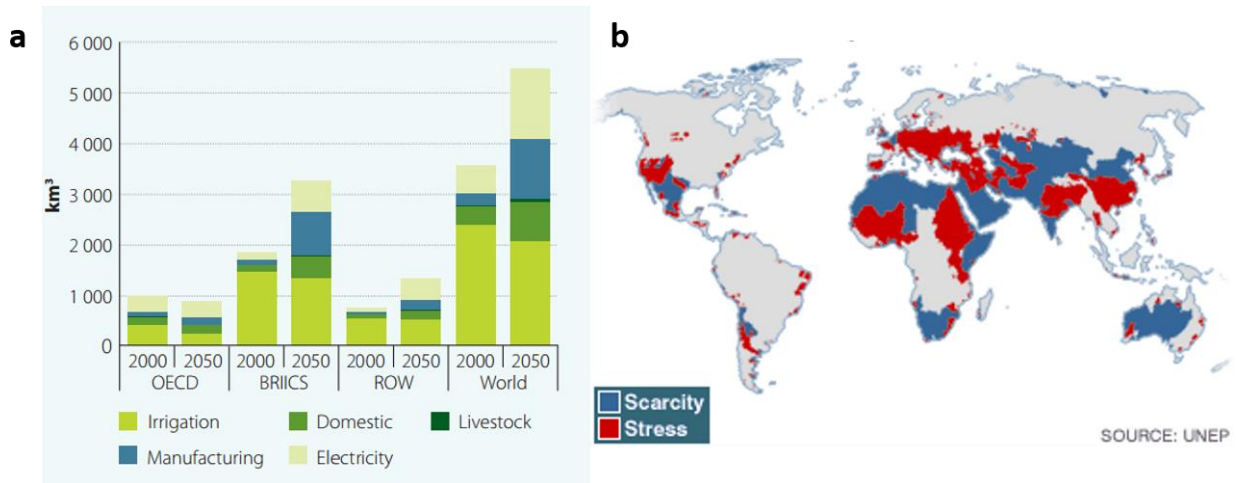


Figure 1-1 (a) Global water demand in 2000 and 2050 [1] and (b) predicted water scarcity and stress in 2025 [2]

To address these issues, various water treatment technologies have been developed, including coagulation and flocculation, filtration, disinfection, lime and soda softening, ion exchange, evaporative processes, adsorption, membrane filtration, photodegradation, etc. [7, 8].

Regardless, numerous research has been conducted on the development of more effective and low-

cost methods and materials for water treatment. Nanotechnology is actively pursued to enhance the performance of existing treatment processes and to develop new processes. Nanotechnology-enabled water and wastewater treatment promises not only to overcome major challenges faced by existing treatment technologies, but also to provide new treatment capabilities that could allow economic utilization of unconventional water sources to expand the water supply [9]. Nanomaterial properties that are desirable for water and wastewater applications include high surface area for adsorption, high activity for photocatalysis, and other unique optical and electronic properties that find use in novel treatment processes and sensors for water quality monitoring.

As Professor Richard E. Smalley of Rice University gave in his presentation “Top Ten Problems of Humanity for Next 50 Year” on Energy & NanoTechnology Conference in 2003, energy and water are at the top of the list, followed by food, environment, poverty, etc. Professor Smalley also envisioned several problems are interlinked, such as the lack of people entering the fields of science and engineering, the need of alternative to fossil fuels and the need to address global warming. Same as the situation of clean water supply, energy supply shortage is another challenge that humans are facing today. According to International Energy Outlook 2016 by US Energy Information Administration (EIA), energy demand worldwide is projected to grow significantly over the 28-year period from 2012 to 2040. Total world consumption of marketed energy expands from 549 quadrillion British thermal units (Btu) in 2012 to 629 quadrillion Btu in 2020 and to 815 quadrillion Btu in 2040, a 48% increase from 2012 to 2040, as shown in Figure 1-2(a) [10]. Current primary energy consumption sources are still fossil fuels (oil, gas and coal), which is more than 85% of total energy consumption sources in 2015, according to World Energy Council, Resources 2016 Summary (Figure 1-2(b)). Such ever increasing energy demand could force the world to face energy crisis on non-renewable fossil fuels. What’s more, effluent gas

emissions from combustion of fossil fuels (CO, CO₂, SO₂, NO_x) could potentially damage world environmental healthy and global warming [11]. Renewable energy resources appear to be a promising alternative to fossil fuel, which is an effective and efficient solution to reduce greenhouse emission from fossil fuel consumption and address the global warming problem. As known, renewable energy resources are generated by natural resources, such as sunlight, wind, hydropower and geothermal energy, of which utilization is extensively limited by variable weather conditions. Thus, to overcome its variability and to use renewable energy, the availabilities of suitable energy storage devices, namely batteries, are required [12].

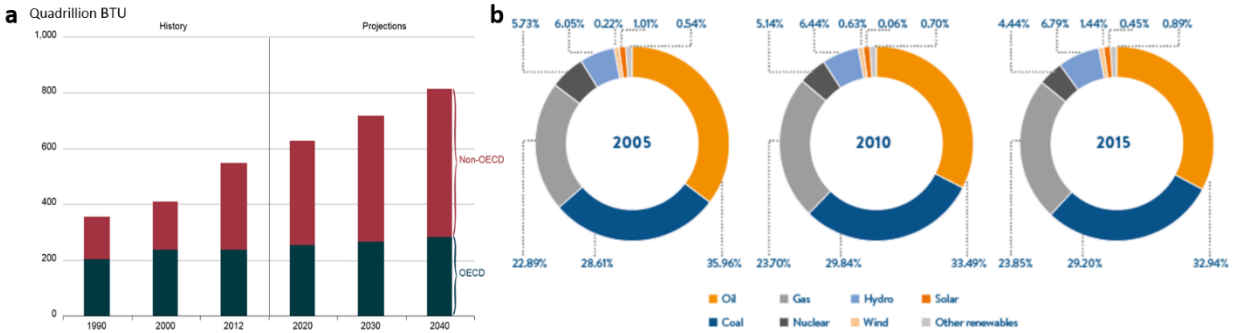


Figure 1-2 (a) World energy consumption, 1990-2040 [10], (b) comparative primary energy consumption over the past 15 years [13]

1.2 Water treatment through photocatalysis and adsorption

Removal of inorganic and organic substances in water to meet certain standard for reuse or drink is the goal for water treatment [14]. Typical inorganic solutes include heavy metals, oxyanions, radionuclides, fluoride, and cations that cause water hardness. Heavy metals such as Pb (II), Cd (II), Cr (VI), Cu (II), As (III) and so on, are serious environmental contaminants, due to their environmental persistence, high toxicity and tendency to accumulate in body tissues [15]. Most heavy metals are known to be carcinogenic agents, even a short-term exposure to heavy metal at trace level is a risk for human beings. For instance, the presence of lead in blood can damage various bodily systems, including the nervous and reproductive systems and kidney. Long

term exposure to arsenic via drinking water causes cancer of the skin, lungs, urinary bladder and the kidney [8]. Nitrogen and phosphorus are needed for aquatic organisms to grow, but the excessive presence of nitrogen and phosphorus in water bodies can cause eutrophication. As a result, heavy metals and phosphorus are targets to be removed from water, especially freshwater bodies [16].

Organic matters in water can be categorized as natural organic matter (NOM) and synthetic organic compounds. As an important component of organic matter, NOM is present in all sources of surface water and groundwater as a heterogeneous mixture of a variety of complex organic and slightly water-soluble materials, including humic substances (hydrophobic), hydrophilic acids, proteins, lipids, carboxylic acids, amino acids, and hydrocarbons [17]. In addition to NOM, many synthetic organic micro-pollutants, such as pesticides, endocrine disrupting compounds (EDCs), and pharmaceutical and personal care products (PPCPs) are also found in water sources [18-21]. Removing these types of synthetic organic matters from drinking water has gained increasing attention to reduce the potential risk to human and wildlife.

Among the various treatment techniques and processes for water and wastewater treatment, photodegradation and adsorption are conventional but efficient techniques for removing contaminants from water [8]. Photodegradation of contaminants by nanomaterials as catalysts is an important method in water and wastewater treatment. Utilizing sunlight and nano-photocatalysts to degrade organic contaminants is important in the area of water and wastewater treatment, especially for the wastewater containing small amounts of organic substance [22]. Photodegradation process possesses several advantages over competing processes, such as complete mineralization, no waste disposal problem, low cost and mild temperature and pressure conditions. The initial process for heterogeneous photocatalysis of organic and inorganic

compounds by semiconductors is the generation of electron-hole pairs in the semiconductor particles. Under light irradiation, the photocatalyst absorbs light with energy equal to or greater than the band gap of the semiconductor, an electron is excited from the valence band to the conduction band. The photoinduced electron transfer to adsorbed organic or inorganic compounds at the surface of semiconductor, and reduce dissolved oxygen in solution; while a hole can migrate to the surface, reacting with adsorbed water or surface hydroxyl groups (-OH) to produce hydroxyl radical ($\bullet\text{OH}$) [22, 23].

Adsorption offers flexibility in design and operation, in many cases it will produce high-quality treated effluent. What's more, most adsorption processes are reversible, the adsorbents can be regenerated for multiple use [24]. The adsorption is mainly through complexation between dissolved metals and the oxygen in metal oxides. The adsorption process can be divided into two steps: fast adsorption of metals ions on external surface of the adsorbent, and rate-limiting intraparticle diffusion along the micropore walls [9]. Nano-adsorbents offer significant improvement with extremely high specific surface area and associated sorption sites, short intraparticle diffusion distance, tunable pore size and surface chemistry. Metal oxides such as iron oxide, titanium oxide, aluminum oxide and zirconium oxide are effective, low cost adsorbents for heavy metals and radionuclides. Besides, clays, activated carbon, zeolites and other nano-structure materials are of great interest in application as support of nano-adsorbents in water and wastewater treatment [25].

1.3 Lithium ion batteries

Lithium ion batteries (LIBs) have become the predominant power source for portable electronics for many years, with the advantages of high energy density, long lifespan and environmental benignity. There is desire for LIBs with high energy density and power density,

long cycle life, and high rate capability to meet the increasing demand [26, 27]. Rechargeable LIBs are considered as a reliable and promising source to store energy for hybrid electric vehicles (HEV) and plug-in hybrid electric vehicles (PHEV) [28]. Currently, graphite-based anodes are used in most commercially available rechargeable LIBs, which provides a theoretical capacity of about 372 mAh g⁻¹ [28, 29]. Due to the low theoretical capacity, graphite electrode can only supply relatively low energy-storage ability and cannot meet the increasing power demand. The design and synthesis of new anode materials are necessary to reach higher performance. Transition metal oxides have shown high theoretical capacity (~500-1000 mAh g⁻¹), which is much higher than graphite material, making them promising anode materials for high performance LIBs. However, most of the transition metal oxides usually suffer from the problem of poor electronic conduction. Another challenge in using transition metal oxide is their poor cycling performance. Therefore, more efforts are needed to improve transition metal oxide anode materials.

1.4 Summary and literature review

1.4.1 Nanostructured TiO₂ material

Titanium is the second most abundant transition metal in the Earth's crust, and its oxide, TiO₂, finds use in a wide array of applications, such as photoelectrode, catalyst, pigment, sensors, energy storage. Among various oxide semiconductor photocatalysts, TiO₂ has been intensively investigated due to its fascinating properties such as biological and chemical inertness, photostability, low cost, nontoxicity and superior oxidization ability [30-32].

Bhatkhande et al. reviewed photocatalytic degradation for environmental applications. In the review they summarized that almost all types of organic and inorganic substances can be degraded using photocatalysis [22]. Introducing photo-catalytic properties into a membrane helps reduce organic fouling by promoting the degradation of organic matters on the membrane surface.

Nanomaterials (e.g., gold nanoparticles, TiO_2) have been widely applied to modify nanofiltration (NF) membranes and their photo-catalytic property have been investigated [33, 34]. Rajesh et al. impregnated poly(amide-imide) and TiO_2 nanoparticle into polysulfone NF membranes and reported a significant improvement in membrane performance including antifouling properties [35]. In a separate study, a TiO_2 nanowire membrane prepared through hydrothermal methods exhibited satisfied photocatalytic activity that nearly 100% humic acid removal was obtained by photocatalytic degradation and filtration [36]. Zhang et al. synthesized anti-fouling $\text{Fe}_2\text{O}_3/\text{TiO}_2$ nanowire membrane, the photocatalytic activity of hybrid membrane improved humic acid removal under solar irradiation (98% removal in 12 h), much higher than TiO_2 nanowire membrane (55% removal in 12 h) [37]. Modification of TiO_2 NF membrane through grafting methyl, phenyl or phosphonic acid groups onto the membrane surface has been shown to reduce membrane fouling by organic matters [38]. TiO_2 and silver nanoparticles have also been applied to modify polymeric membranes to reduce biofouling [39-42] .

However, applications of TiO_2 as photocatalyst is limited by its fast electron recombination rate, which results in low photocatalytic reaction efficiency significantly. What's more, bare TiO_2 has wide electronic band gap (3.2 eV), so it can only be excited by UV light which only accounts for 2-3% of the solar spectrum [32]. Numerous effects have been done to increase light response in visible light region and to reduce the recombination for enhancing light conversion efficiency. For example, Zhou et al. synthesized $\text{Ag}_2\text{O}/\text{TiO}_2$ nanobelts, which showed enhanced degradation of methyl orange under ultraviolet and visible light [43]. Ag/reduced graphene oxide (rGO) co-decorated TiO_2 nanotube arrays as a new photocatalyst, exhibited almost 100% photocatalytic removal of typical herbicide 2,4-dichlorophenoxyacetic acid under simulated solar light irradiation

[44]. Under UV light irradiation, carcinogenic Cr(VI) in aqueous solution was photocatalytic reduced to less toxic form of chromium, Cr(III), over ZnO semiconductor catalyst [45].

A variety of TiO₂ nanomaterials, such as nanotubes, nanowires, nanoparticles, nanocrystal films, nanotube arrays, and more, have been reported. Three-dimensionally ordered macroporous (3DOM) materials are well-known for uniform pore size, high surface area and controllable, ordered porosity. 3DOM TiO₂ has attracted intensively attention in applications as catalyst or catalyst support, adsorptions, battery electrode materials and photonic materials. 3DOM structure has been demonstrated to enhance the light absorption and to improve light conversion efficiency, the periodic structure forbids the propagation of light with certain energies, increase the path length of light through slow-light effect and result in a stop-band reflection because of coherent Bragg diffraction [46-48]. Wu et al. studied optical and photocatalytic properties of 3DOM TiO₂ with different pore sizes, and they found when photonic bandgap edges match the electronic bandgap of TiO₂, slow photons effect at the photonic bandgap edges improved light absorption [49]. What's more, when the photonic band gap is close to photocatalysis irradiation wavelength, light absorption by the material and photochemical process could be enhanced [50].

While application of TiO₂ in photocatalysis has been extensively studied for years, interests on TiO₂ as an anode material in LIBs developed several years ago, due to its electrochemical stability in common electrolytes and the lack of harmful solid-electrolyte interfacial (SEI) layers, resulting in better overcharge protection and safety [51]. Another key advantage of TiO₂ is that it can retain its capacity at fast charge/discharge rates [52]. 3DOM TiO₂ has been reported to possess excellent initial capacity of 248 mAh g⁻¹ at 0.2 C and 208 mAh g⁻¹ at 1C, and delivers a stable capacity (over 170 mAh g⁻¹ at a rate of C/2) over 100 cycles [51, 52].

Besides the photonic and electrochemical properties, hierarchical porosity of 3DOM systems are beneficial for heterogeneous catalytic applications, as they provide small pores for nanoparticle immobilization and the presence for larger pore networks reduces mass transport limitations [53]. In 3DOM structure, the macro-sized ball-shaped pores are closely packed with a high degree of order and interconnected to each other through small windows. The large pores in these materials have been found to improve the accessibility of reactants to the active sites of the material.

Based on literature review, as functional material or support, TiO₂ based nanomaterials have advantages as photocatalyst and anode material in LIBs. There are still some drawback limiting its application, such as large band gap, high recombination rate as photocatalyst, relatively low capacity compared to graphite-based anode materials.

1.4.2 Nanostructured ZrO₂ material

Zirconium oxide has valuable chemical and physical properties, including high melting point, mechanical and thermal resistance, low electrical conductivity, biocompatibility, chemical inertness (resistant to oxidant agent and acids/bases, non-toxic, and not dissolvable in water is a widely used inorganic material [54, 55]. ZrO₂ is practical applied in fuel-cell technology, catalyst or catalyst support, oxygen sensor, thermal-barrier coatings and so on [56].

Zirconium oxide exhibits specific binding affinity toward fluoride through metal-ligand interaction [57], strong affinity toward phosphate and arsenic through inner-complex [16, 54, 58], as a result, ZrO₂ is widely studied as adsorbents. Amorphous ZrO₂ demonstrates high adsorptive capacity due to the porous and highly hydrated structure, which allow ions to diffuse into the structure rather than restricted to just the external surface site. Shang's group studied adsorption removal of arsenic and phosphate onto amorphous ZrO₂ NPs, which were synthesized by a simple

hydrothermal reaction [16, 54]. In their studies, the am-ZrO₂ NPs were found to have very strong adsorption on arsenic species and phosphate, through inner-complex mechanism. Mesoporous ZrO₂ was synthesized and showed maximum phosphorus adsorption capacity of 29.71 mg P/g [59]. Hydrous ZrO₂ NPs were reported strong arsenic adsorption for both As (III) and As (V) in both lab synthesized and natural water samples [58].

Usually presented as fine or ultrafine particles, zirconium oxide as adsorbents are difficult to separate and recover from water by filtration or centrifugation. Also, when directly used in fixed-bed or any other flow-through systems, the pressure drop during operation being technical bottleneck [57]. Therefore, supporting nanosized ZrO₂ onto substrate provides an attractive alternative to overcome the disadvantage of NPs. What's more, dispersion of metal oxides over support with high surface area is an effective method to enhance the adsorption capacities of active species. Magnetic mesoporous SiO₂, SBA-15, ion exchanger, cotton fiber, graphite oxide, polymer resin have been studied as support of ZrO₂ nanomaterials, in environmental applications [57, 60-64]. Nano-hydrous zirconium oxide was encapsulated as the active species on an anion exchange resin, the supporting resin and hydrous zirconium oxide NPs captured phosphate through nonspecific electrostatic affinity and inner-sphere complexes, respectively [62]. The nanocomposite adsorbent exhibited highly preferable removal of phosphate from water, even other commonly occurring anions at greater levels presented in aqueous solution. Clays are known as low cost, abundance, high sorption properties and potential for ion-exchange, clays minerals are interesting materials for use as adsorbents, and have been studied as support for nanoparticles [65-69].

1.5 Objectives of study

The overall objective for the proposed study is to synthesize and modify nanostructured TiO_2 and ZrO_2 , in order to improve the performance in water treatment and energy storage applications. The first objective is to demonstrate novel TiO_2 -based photocatalysts with hybrid composites structures and enhanced activity for organic compounds degradation in water, and contribute more information about the reaction mechanism. The second objective is to incorporate TiO_2 and Fe_2O_3 with novel structure to obtain a stable anode material for LIBs. The third objective is to prepare zirconium modified clays for phosphorus removal from water through adsorption, adsorption performance as kinetics and equilibrium isotherms was studied to understand the process. To achieve the research objectives, the work is divided into three major tasks, which are summarized below.

Task 1. Nanostructure Pt/rGO-TiO₂ photocatalyst for degradation of MO (Chapter 2)

The objective of this task is to synthesize Pt/rGO-TiO₂ nanocomposite, with Pt and rGO decoration on 3DOM TiO₂ simultaneously, which could help improve visible light absorbance and facilitate electron-hole separation to enhance photocatalytic activity. Three subtasks will be carried out:

- 3DOM TiO₂ will be synthesized by CCT and sol-gel method.
- Pt nanoparticles will be deposited on TiO₂ using impregnation method, and rGO will be thermo-reduced from GO, to obtain Pt/rGO-TiO₂ photocatalyst. And Pt-TiO₂ and rGO-TiO₂ will be synthesized as comparison.
- The resulting nanomaterials will be characterized using various techniques, such as scanning electron microscopy (SEM), transmission electron microscopy (TEM), high-resolution TEM (HRTEM), X-ray diffraction (XRD), X-ray photoelectron spectroscopy

(XPS), and UV-vis diffuse reflectance spectra. Finally, the nanomaterials will be applied to methyl orange (MO) photodegradation as model pollutant.

Task 2. Carbon coated Fe₂O₃/TiO₂ anode material for LIBs (Chapter 3)

The objectives of this task are to fabricate and characterize carbon coated Fe₂O₃/TiO₂ composite and apply the materials to LIBs anode. The electrochemical performance of Carbon coated Fe₂O₃/TiO₂ hybrid material will be evaluated. Three subtasks will be carried out:

- 3DOM TiO₂ will be synthesized by CCT and sol-gel method.
- Fe₂O₃ nanospindles will be assembled onto 3DOM TiO₂, and the resulted material will be carbon coated using glucose as carbon source.
- The obtained materials will be characterized using various techniques, such as scanning electron microscopy (SEM), transmission electron microscopy (TEM), high-resolution TEM (HRTEM), X-ray diffraction (XRD), X-ray photoelectron spectroscopy (XPS), Raman spectrum. And the nanomaterials will be tested as anode material for LIBs.
- Electrodes and half-coin cells will be prepared, and their performance will be investigated.

Task 3. Zirconium modified clays for phosphorus removal from aqueous solution through adsorption (Chapter 4)

The objective of this task is to fabricate and characterize zirconium modified clays, which could adsorb phosphate in water as low-cost adsorbents. To study phosphate removal performance of zirconium oxide on different supports, three clays with different structure are chosen to be studied. Three subtasks will be carried out:

- A series of zirconium modified clays with different Zr/clay ratios will be synthesized through simple reaction, using ZrOCl₂ as zirconium source.

- The resulting materials will be characterized using various techniques, such as scanning electron microscopy (SEM), X-ray diffraction (XRD), zeta-potential measurement.
- Phosphorous adsorption capacity of different zirconium modified clays will be evaluated by equilibrium isotherm and kinetic study at neutral pH. The equilibrium isotherms and kinetic results will be analyzed by appropriate models to understand the adsorption process.
- The impact of clay structure as support of zirconium oxide will be discussed.

CHAPTER 2 Pt/rGO-TiO₂ photocatalyst for degradation of MO

2.1 Introduction

Semiconductor-based heterogeneous photocatalysis has been increasingly applied to deal with environmental pollution problems [30]. Photocatalytic oxidation of organic pollutants in water is a promising technique for water and wastewater treatment [70]. Under light irradiation, the photocatalyst absorbs light with energy equal to or greater than the band gap of the semiconductor, an electron is excited from the valence band (VB) to the conduction band (CB), leaving a positively charged hole (h^+) at the band edge of the VB. The photoinduced electrons (e^-) transfer to adsorbed organic or inorganic compounds at the surface of semiconductor, and reduce dissolved oxygen in solution; while a hole can migrate to the surface, reacting with adsorbed water or surface hydroxyl groups (-OH) to produce hydroxyl radical (\bullet OH) [22, 23]. Among various oxide semiconductor photocatalysts, titanium oxide (TiO₂) has been intensively investigated due to its fascinating properties such as biological and chemical inertness, photostability, low cost, nontoxicity and superior oxidization ability [30-32]. However, applications of TiO₂ as photocatalyst is limited by its fast electron recombination rate, which results in low photocatalytic reaction efficiency significantly. What's more, bare TiO₂ has wide electronic band gap (3.2 eV), so it can only be excited by UV light which only accounts for 2-3% of the solar spectrum [32]. To achieve effective light conversion efficiency with TiO₂-based photocatalysts, more effects are still required to extend light response in visible light region and reduce the recombination.

Among a variety of TiO₂ nanomaterials, three-dimensionally ordered microporous (3DOM) structure is drawing increasing attention for its advantageous properties, including unique periodic structure, optical properties and favored mass transfer. 3DOM materials, also known as inverse opal, are commonly synthesized through colloidal crystals templating (CCT) method. The

colloidal crystals are self-assembled from monodisperse microspheres, such as poly(methyl methacrylate) (PMMA), polystyrene (PS), silica, to a face-centered close-packed or opal arrangement. A liquid precursor penetrates the opal and fills the voids of the templates. After solidification of the precursor, the colloidal templates are removed by calcination or extraction, yielding an inverse opal replica of the array of ordered spheres. Where the original microspheres made contact, the macropores are interconnected by windows.

3DOM structure has been demonstrated to enhance the light absorption and improve light conversion efficiency, the periodic structure forbids the propagation of light with certain energies, increase the path length of light through slow-light effect and result in a stop-band reflection because of coherent Bragg diffraction [46-48]. Wu et al. studied optical and photocatalytic properties of 3DOM TiO₂ with different pore sizes, and they found when photonic bandgap edges match the electronic bandgap of TiO₂, slow photons effect at the photonic bandgap edges improved light absorption [49]. What's more, when the photonic band gap is close to photocatalysis irradiation wavelength, light absorption by the material and photochemical process could be enhanced [50]. Besides the photonic properties, hierarchical porosity of 3DOM systems are beneficial for heterogeneous catalytic applications, as they provide small pores for nanoparticle immobilization and the presence for larger pore networks reduces mass transport limitations [53].

In order to reduce the electron recombination and widen the light absorption spectrum of TiO₂, studies have been done about modifications on TiO₂. Doping with other elements or incorporating with electron-accepting materials, such as loading noble metals like Au or Pt to enhance the separation of the photogenerated electrons and holes, or carbon nanotubes or graphene to increase the visible-light adsorption [71, 72]. Owing to its excellent catalytic property, Pt is the most widely used active catalyst, and decoration of TiO₂ by Pt has been studied [73]. In aspect of

photocatalyst, Pt nanoparticles respond strongly to visible light due to their surface plasmon resonance (SPR), which refers to a collective oscillation of conduction electrons induced by the electric field of light [74-76]. By incorporating Pt nanoparticles on the surface of inverse TiO₂ opals, more light is absorbed and the lifetime of the light-excited electron and holes are extended. Liang et al studied synthesized 3DOM Pt/TiO₂ as catalyst for water-gas shift reaction, and they observed very good catalytic performance due to better mass transfer of 3DOM porous structure and high intrinsic activity of Pt/TiO₂ [77]. Synergy of slow photon effect and chemically amplified photochemistry in Pt loaded 3DOM TiO₂, as photocatalyst of methyl orange (MO) degradation. The improved photocatalytic activity is attributed to the existence of metallic Pt, which facilitates the scavenging of the excited electron and increases efficient electron-hole separation [71].

However, the catalytic activity of noble metal/TiO₂ materials is severely limited by the ultrafast relaxation of hot electrons (<160 fs) and rapid charge recombination. Coupling with graphene - an electron acceptor material with high electron mobility, has been reported to maximize the charge separation [73, 78]. Graphene is known with excellent conductivity, large specific surface area, and high hydrophobicity, not only can significantly suppresses recombination of photogenerated electron-hole pairs of TiO₂ and increasing charge transfer rate of electrons, but also can extend light absorption spectrum, and increase surface-adsorption capacity to organic molecules [32, 44, 79, 80]. Combining noble metal nanoparticles and graphene materials to improve TiO₂ catalytic activity has been studied, based on different TiO₂ structure, including nanoparticles, nanotubes and 3DOM TiO₂ [44, 78, 81, 82]. The ternary hybrid catalysts based on different structures of TiO₂ (3DOM, nanotube arrays and nanosheets) all showed significantly improved catalytic activity and stability, which provides some new hints for improving TiO₂ photocatalytic activity under visible light.

Recently Boppella et al. reported Au nanoparticles and reduced graphene oxide (rGO) incorporated TiO₂ inverse opal photoelectrodes, focusing on solar-to-energy application as photoelectrochemical (PEC) water splitting devices [78]. The literature reports provide a guide for rational design a novel and effective visible-light driven photocatalyst in water treatment. In the present work, a new Pt/rGO-TiO₂ photocatalyst was designed and prepared by Pt nanoparticles and rGO co-modification on 3DOM TiO₂. 3DOM TiO₂ was synthesized through colloidal crystals templating (CCT) method using poly(methyl methacrylate) (PMMA) as sacrificial template and sol-gel method using Ti(OBu)₄ as precursor. The obtained 3DOM TiO₂ was modified with Pt nanoparticles and reduced graphene oxide for improved visible-light photocatalytic ability, as illustrated by the photocatalytic degradation of methyl orange (MO) as a representative dye. Pt/rGO-TiO₂ showed higher light absorption and photocatalytic degradation efficiency toward MO under visible light, compared to 3DOM TiO₂, Pt-TiO₂ and rGO-TiO₂. In the stability test, the prepared photocatalyst maintained high photocatalytic activity after 3 cycles. Thus, this new ternary hybrid photocatalyst has potential applications in environmental purification.

2.2 Experimental

2.2.1 Chemicals and materials

All chemicals were reagent grade and used without further purification. Methyl methacrylate (MMA), titanium butoxide (Ti(OBu)₄), acetylacetone (ACAC), ethanol, chloroplatinic acid hexahydrate (H₂PtCl₆·2H₂O), methyl orange (MO) were purchased from Sigma-Aldrich. Single layer graphene oxide was purchased from ACS Material. Potassium persulfate (K₂S₂O₈) was purchased from Alfa Aesar. Ultrapure water (resistivity > 18.0 MΩ) was used for all experiments.

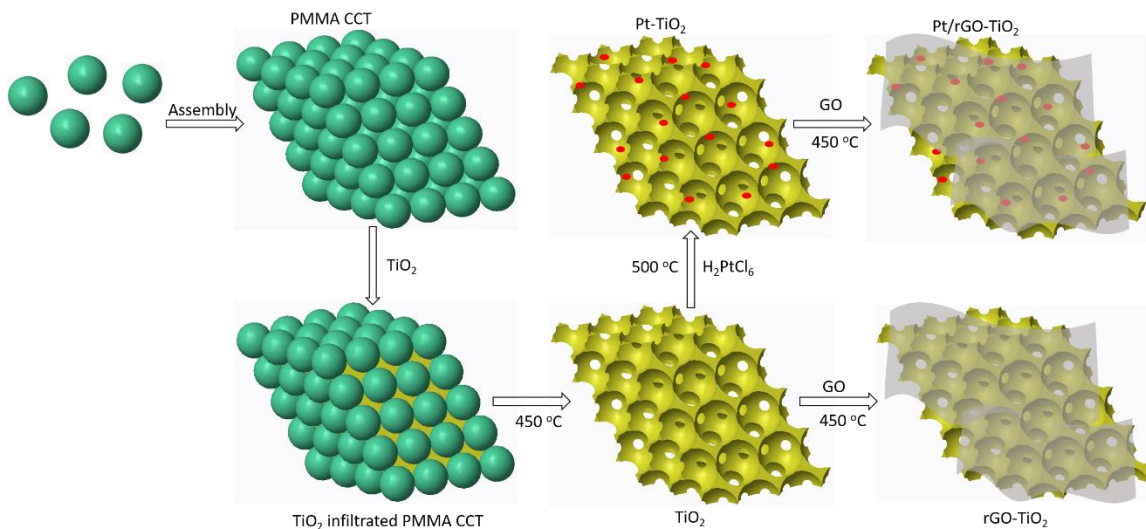


Figure 2-1 Schematic illustration of fabrication processes of 3DOM TiO₂ modified with Pt NPs and rGO

2.2.2 Preparation of PMMA template

Monodisperse PMMA nanospheres were synthesized using surfactant-free emulsion polymerization according to literature techniques [83]. In a typical synthesis, a mixture of ultrapure water (165 mL) and methyl methacrylate (MMA, 18.6 mL) was prepared in a three-neck round-bottom flask, with a water-cooled condenser. The mixture was stirred at 350 rpm, while being heated to 70 °C and purged with nitrogen gas to deactivate the inhibitors. After stabilization of the temperature, K₂S₂O₈ (0.5 × 10⁻³ mol/L, 0.0236g) was added into mixture as initiator dissolved in 10 mL water. The reaction was sustained for 2 hours, producing colloidal PMMA spheres. PMMA colloidal crystals were formed by centrifuging the colloid at 1500 rpm for 24 h, decanting the water and allowing the solid dry for 3 days.

2.2.3 Preparation of 3DOM TiO₂

TiO₂ precursor was prepared by mixing Ti(OBu)₄, ACAC, H₂O and ethanol in molar ratio: 1:1:3:20 in open air at room temperature for 2 hours. The obtained solution was stored in brown glass bottle for future use. Dried PMMA colloidal crystals were crushed to a powder and deposited in millimeter-thick layers on filter paper in a Büchner funnel. With suction applied to the Büchner

funnel, the precursor solution was applied dropwise to completely wet the PMMA powder. The infiltration was repeated by 5 times. After dried at room temperature for 2 hours, the samples were calcined at 300 °C at a step of 2 °C per min for 3 hours to remove PMMA template and then at 450 °C at a step of 2 °C per min for 4 hours to calcine TiO₂.

2.2.4 Preparation of Pt-TiO₂

Pt was loaded on 3DOM TiO₂ with impregnation method using H₂PtCl₆ solution as precursor [77, 84, 85]. 1.5 mL of 7mM H₂PtCl₆ aqueous solution was dropped onto 0.1 g 3DOM TiO₂ sample and dried under air at 70 °C for 12 h and subsequently calcined at 500 °C for 3 h.

2.2.5 Pt/rGO-TiO₂ and rGO-TiO₂ composite catalysts

In a typical synthesis, desired amount of graphene oxide (0.127 mL, 10 mg/L) solution were made into 20 mL aqueous solution, and the mixture was ultrasonicated for 1 hour (Branson, 2510). Then certain amount of Pt-TiO₂ (0.0636g) were added in to GO solution and ultrasonicate for 1 hour, the ratio of GO/Pt-TiO₂ was 2 wt%. Pt/GO-TiO₂ was filtered with FP-200 membrane (Paul Life Sciences, PVDF) and dried in air. The obtained material was calcined at 500 °C for 2 h to reduce GO to graphene. rGO-TiO₂ was obtained by the same method by adding TiO₂ instead of Pt-TiO₂.

2.2.6 Material characterization

The morphology and of sample were imaged with scanning electron microscopy (SEM) using a Hitachi S-4800 SEM microscope and Hitachi H9000NAR transmission electron microscopy (TEM). The composition of the obtained material was examined by Energy-dispersive X-ray spectroscopy (EDS) integrated with SEM. The content of Pt was analyzed by dissolving Pt nanoparticles in HCl and HNO₃ completely and measure the concentration of Pt in solution using inductively coupled plasma-optical emission spectroscopy (ICP-OES) (Perking Elmer Optima

2100 DV). The crystal structure and phase state of Pt-TiO₂ were determined by X-ray diffractometry (XRD) using Bruker D8 Discover A25 diffractometer with copper K_α radiation. Raman spectra were taken on a Reinshaw 1000B Raman spectrometer with a 632.8 nm HeNe laser source. X-ray photoelectron spectroscopy (XPS) was employed to characterize the chemical states of prepared photocatalyst using Perkin Elemer PHI 5440 ESCA system with an Al K_α X-ray source. The UV-Vis diffuse reflectance spectra were tested using a Shimadzu UV-2600 UV-Vis spectrophotometer, with BaSO₄ as reference.

2.2.7 Photocatalytic activity test

The photocatalytic activity of 3DOM TiO₂, Pt-TiO₂, rGO-TiO₂ and Pt/rGO-TiO₂ was quantified by monitoring the degradation of MO under visible light irradiation. A 300 W Xenon lamp was used as the light source (CEL-HXF300, Beijing China Education Au-light Co., Ltd). The photocatalytic reaction was performed in a reactor, which was surrounded by water-cooled jacket. A cut-off filter (>420 nm) was mounted before the output of light to removes UV light and admit only visible light to enter the reactor. For these MO degradation tests, 20 mL aqueous suspensions of MO (10 mg/L) and 20 mg photocatalyst powders were placed in reactor. The dispersions were kept in the dark for 30 minutes with magnetic stir to achieve adsorption-desorption equilibrium. Aliquots (1 mL) were collected and centrifuged to remove catalyst particles every 15 min during visible-light illumination. The concentration of residual MO was determined by monitoring its UV-visible absorption peak at absorption at 464 nm [86]. The concentration of MO is proportional to its absorbance. MO degradation was expressed as C/C_0 vs irradiation time, where C_0 is the concentration of the original MO solution after 30 min adsorption, and C is the concentration of MO solution after every 15 min reaction.

To test the reusability of the Pt/rGO-TiO₂ sample, the photocatalytic test was repeated three times. The experimental conditions were the same as previously described, except the reaction time was limited to 90 min. After each round of the reaction, the mixture was recovered by centrifuged and rinsed by ultrapure water.

2.3 Results and discussion

2.3.1 Synthesis and characterization of materials

Pt/rGO-TiO₂ composite was synthesized in three steps (Figure 2-1): (1) synthesis of 3DOM TiO₂ through CCT and sol-gel method, (2) Pt nanoparticles were loaded onto 3DOM TiO₂ through impregnation method using H₂PtCl₆ as precursor and (3) modification and reduction of GO in Pt/rGO-TiO₂ composite. A combination of techniques, described individually in detail in the Experimental Section, were used in the synthesis process, including CCT, sol-gel processing, impregnation method.

As shown in Figure 2-2(a), 3DOM TiO₂ exhibits a highly ordered microporous structure, which replicate the three-dimensional closely-packed PMMA opals in Figure S2-1 (Appendix), with pore diameter about 210 nm and 25 nm wall thickness. The pore size of 3DOM TiO₂ is smaller than PMMA spheres (~330 nm) due to a shrinkage during the calcination. The small windows between the opal pores can be clearly observed in Figure 2-2(b), which replicates from the contact bridges between the neighboring PMMA spheres. The underlying layer of pores and porous walls can be clearly observed, indicating that the sample possesses a three-dimensionally well-open, ordered and interconnected microporous network. Figure 2-2(b) shows that Pt nanoparticles have been successfully deposited on the surface of 3DOM TiO₂ by the impregnation method. Pt nanoparticles are well dispersed on TiO₂ surface and uniform in size. Pt content of 1.7 wt% was confirmed by ICP-OES, which is close to the experimental design (2 wt%). After deposition and

reduction of GO on TiO_2 , a continuous and transparent rGO film is formed on the surface of 3DOM TiO_2 (Figure 2-2(c)). When using Pt- TiO_2 instead of bare 3DOM TiO_2 , the ternary Pt/rGO- TiO_2 composite was obtained (Figure 2-4(d)).

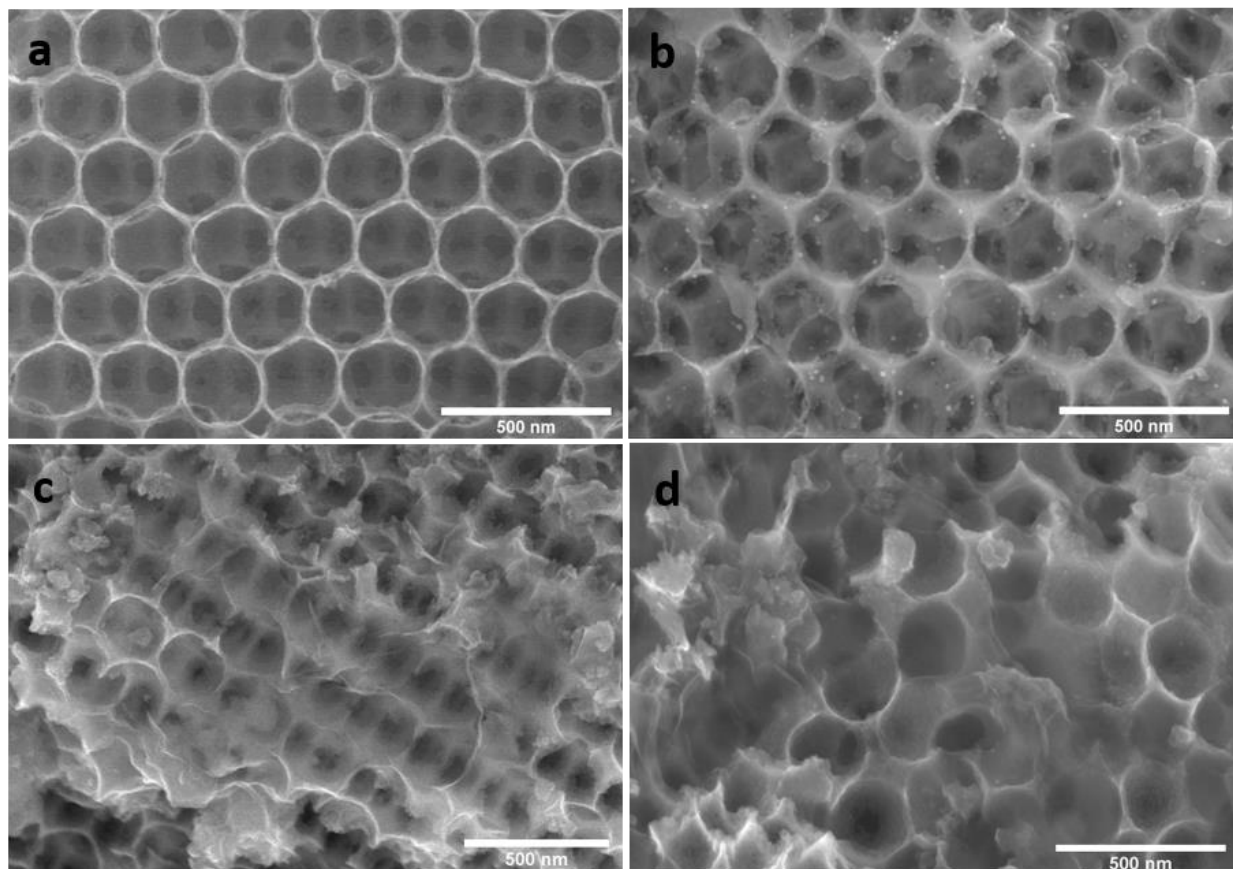


Figure 2-2 SEM images of (a) 3DOM TiO_2 , (b) Pt- TiO_2 , (c) rGO- TiO_2 , (d) Pt/rGO- TiO_2

The Pt- TiO_2 sample was further characterized using TEM to confirm the phase of TiO_2 and the existence of Pt nanoparticles. From Figure 2-3(a) the well-defined 3DOM structure with overlapped pores can be easily observed, and the porous skeleton of 3DOM TiO_2 are composed of many nanoparticles. At higher magnification (Figure 2-3(b)), it is clear to see Pt nanoparticles are highly dispersed on 3DOM TiO_2 wall and sizing range from 3-6 nm. HRTEM image (Figure 2-3(c)) shows the lattice fringes of both TiO_2 and Pt, which indicates the highly crystalline nature of TiO_2 and Pt nanoparticles. The lattice fringe with a d-spacing of 0.352 nm can be assigned to the

(101) lattice plane of anatase TiO_2 , and the fringe with d-spacing of 0.224 nm belongs to the (111) lattice plane of Pt nanoparticles.

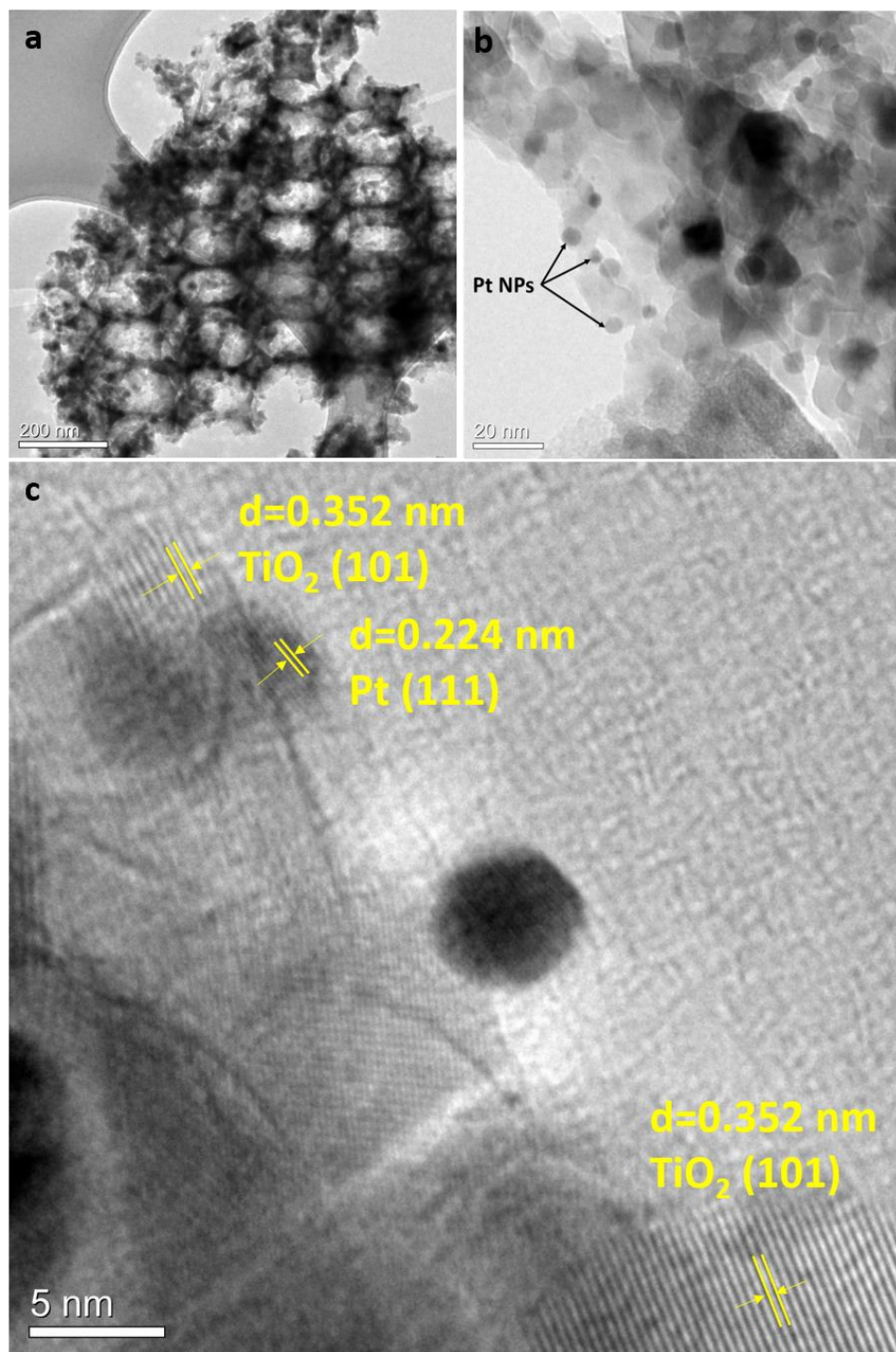


Figure 2-3 (a)-(b) TEM images of Pt-TiO₂ with different magnifications and (c) HRTEM image of Pt-TiO₂

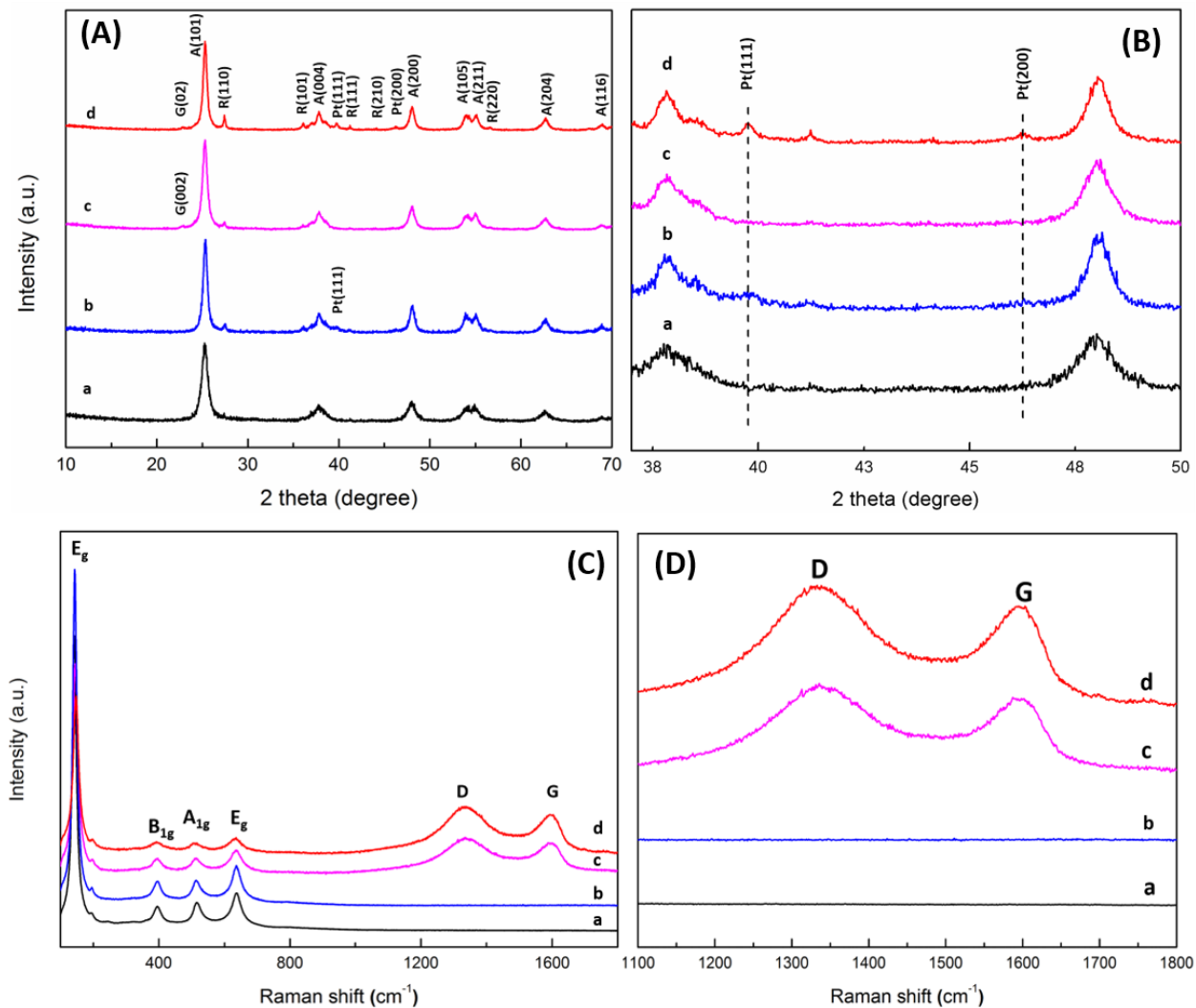


Figure 2-4 XRD patterns of as-prepared catalysts with 2 theta between (A) 10° and 70° and (B) 37° to 50°; Raman spectra of as-prepared catalysts with wavelength (C) 250-1800 cm^{-1} and (D) 1100-1800 cm^{-1} . a) TiO_2 , b) Pt- TiO_2 , c) rGO- TiO_2 , d) Pt/rGO- TiO_2

The structure of catalysts was characterized by XRD, as shown in Figure 2-4(A). XRD patterns show the main phase of TiO_2 in all four samples are anatase, characteristic peaks at 25.3°, 36.9°, 37.8°, 48.0°, 53.1°, 55.1°, 62.7°, 68.8° can be assigned to the plane (101), (004), (200), (105), (211), (204), (116) of anatase (JCPDS 21-1272), respectively. The peaks at 27.5°, 36.1°, 41.2°, 44.1°, 56.6°, represent planes (110), (101), (111), (210), and (220) of rutile (JCPDS 21-1276). With both Pt- TiO_2 and Pt/rGO- TiO_2 samples, the weak peak at 39.7° and 46.2° could be indexed to the (111) and (200) planes of the Pt nanoparticles (JCPDS 65-2868), respectively

(Figure 2-4(B)). The weak peak at 22.8° in rGO-TiO₂ and Pt/rGO-TiO₂ deviates from the characteristic (002) plane reflections of graphitic carbon at 26.3° [87]. The broad diffraction peak of rGO indicates poor ordering of the sheets in the stack direction, which may due to mainly single or only a few layers of rGO in composites [88]. The main characteristic peak of rGO (ca. 25) has low intensity and overlap with the peak of anatase TiO₂ at 25.3° [89].

The crystalline structure of TiO₂ and rGO were further investigated by Raman spectroscopy, as shown in Figure 2-4(C)-(D). For all samples, the characteristic peaks at 146 (E_g), 396 (B_{1g}), 515 (A_{1g}) and 637 cm⁻¹ (E_g) are attributed to anatase TiO₂, which corroborate XRD results [30]. The peaks at 146 cm⁻¹ is derived from the bending vibration of O-Ti-O bond, the other three peaks are related to Ti-O-Ti bending types [48]. The weak peaks at 197 cm⁻¹ are assigned as rutile TiO₂. Characteristic bands at 1340 and 1590 cm⁻¹ were assigned to D and G peaks for rGO. D band represents the dispersive and defect-induced vibrations and G peak is related to the in-plane vibration of sp² bonded carbon atoms. The similarity of D and G peaks in intensity indicates the rGO contains a large amount of disordered sp² carbons, which are related to the defects that may be generated during the reduction process [90, 91].

XPS was employed to study the chemical states of elements and the interaction between TiO₂ and rGO in Pt/rGO-TiO₂ composite. The curve fitting of O 1s, C 1s, Ti 2p and Pt 4f peaks of XPS spectra for the composite are shown in Figure 2-5(a)-(d). The O 1s spectrum was fitted with two peaks at 530.1 eV and 531.9 eV. The former is the characteristic of the lattice oxygen of TiO₂, and the other one with 1.8 eV higher binding energy can be assigned to the surface-adsorbed component of the hydroxyl group (Ti-OH) [92]. Two types of carbon with different binding energies at 285.2 eV and 287.4 eV were observed, which were assigned to the sp²-hybridized C, the carbonyl C (C=O), respectively. The absence of C in C-O bonds and carboxylate C (O=C-O)

and low intensity of carbonyl C (C=O) indicate that GO was mainly reduced by removing C-O and C=O bonds and a high crystalline degree of graphene [78, 81, 90, 93]. There are two characteristic peaks at 459.3 eV (Ti 2p_{3/2}) and 465.0 eV (Ti 2p_{1/2}) on Ti 2p XPS spectrum, which correspond to spin-orbital splitting photoelectrons in anatase TiO₂ structures. The peaks shifted toward higher binding energy end comparing to pure TiO₂ (458.5 eV and 464.2 eV), the red-shift suggested the formation of strong electronic interactions between TiO₂ and rGO. The electronic interactions caused change in chemical state and/or coordination environments of Ti⁴⁺, suggesting a charge transfer from TiO₂ to rGO [78, 94, 95]. The Pt 4f spectrum was fitted into three sets of peaks. The strongest set at 70.9 eV and 74.3 eV are assigned to metallic Pt. The second set of peaks at 72.7 eV and 75.9 eV is due to Pt (II), and the last set with lowest intensity at 75.2 eV and 77.6 eV could be from a small amount of Pt (IV) [71, 84].

The optical property of 3DOM catalysts, UV-vis diffuse reflectance spectroscopy (DRS) studies were performed on all samples, the results are shown in Figure 2-6(A). 3DOM-TiO₂ exhibits a wider light absorption region comparing to the commercial P25, owing to the slow photon effect and multiple scattering of the 3DOM structure. As shown in reflectance spectrum (Figure 2-6(A)-a), 3DOM TiO₂ has a strong stop band maximum at 400 nm which is near the electronic absorption edge. The strong reflection peak indicates a high-quality inverse opal structure in wide range [96]. According to modified Bragg equation, the photonic stop band of 3DOM TiO₂ was estimated at about 527 nm (Appendix) [97, 98]. When stop-band is in visible range, the visible light absorption by the material and photochemical process would be enhanced [50].

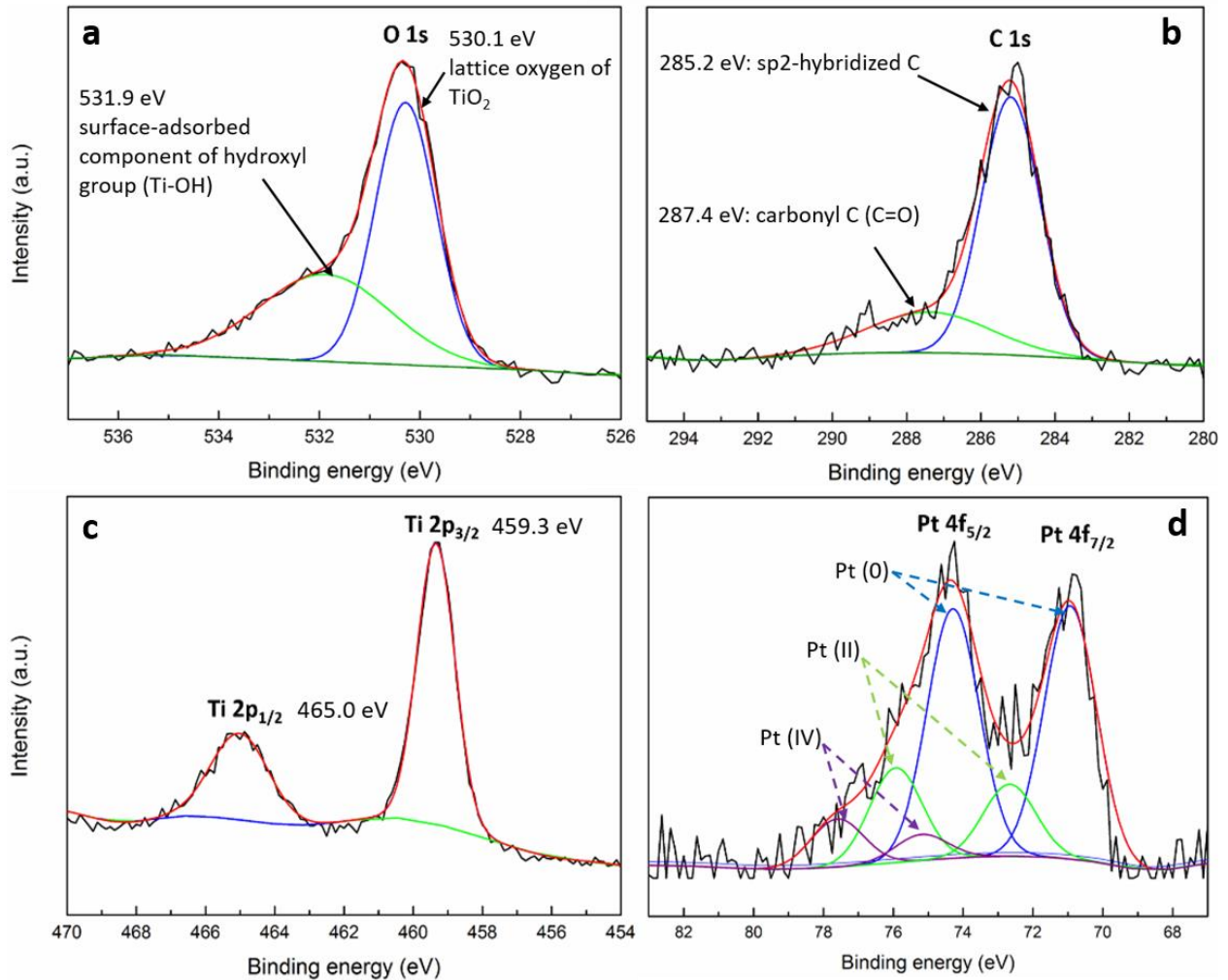


Figure 2-5 Fitted XPS spectra (A) O 1s, (B) C 1s, (C) Ti 2p and (D) Pt 4f of Pt/rGO-TiO₂ composite

The modification of Pt obviously increased light adsorption in the visible light range owing to the surface plasmon resonance (SPR) effect and photosensitizing effect of Pt. Unlike other plasmon metal, no Pt SPR peak observed, because small Pt nanoparticles always exhibit broad extinction below 450 nm, without observable peaks [74-76]. It can be observed a red-shift in absorption edge and enhanced light absorption across the visible region for rGO-TiO₂. The addition of rGO extends visible light adsorption properties, may be attributed to the chemical bonding between TiO₂ and rGO, formation of Ti-O-C bond, similar to C-doped TiO₂ composites [79, 99]. Visible light adsorption is further improved by adding rGO into Pt-TiO₂, due to the

overlapping of extended adsorption properties by rGO and Pt plasmonic adsorption. This simultaneous modification of Pt and rGO could attribute to enhance the photoexcitation efficiency of TiO₂ and therefore its photocatalytic activity in theory.

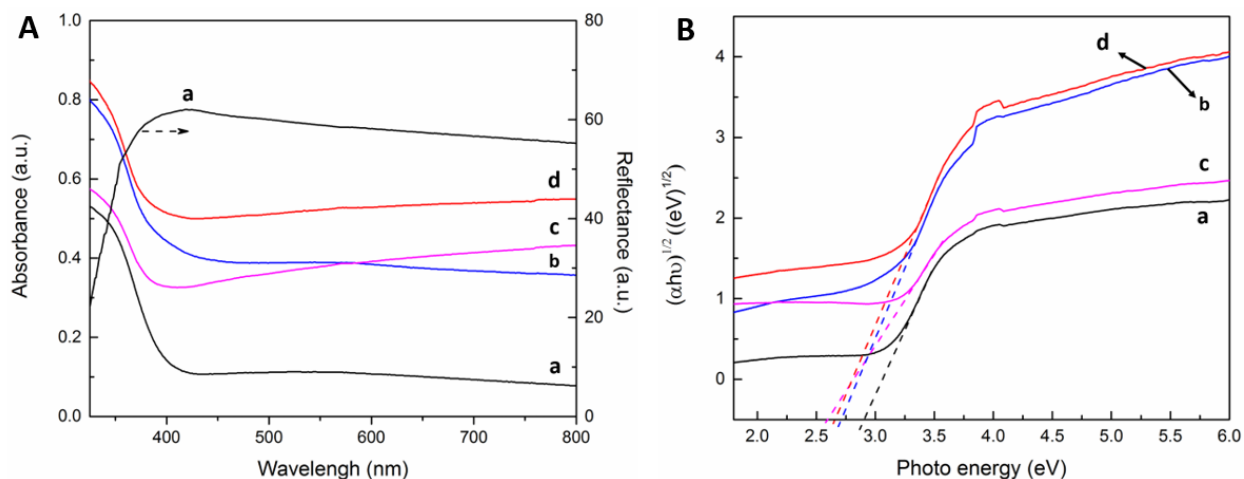


Figure 2-6 UV-vis diffuse reflectance spectra (A) and Kubelka-Munk transformed reflectance spectra (B) of a) TiO₂, b) Pt-TiO₂, c) rGO-TiO₂, d) Pt/rGO-TiO₂. (A) shows simultaneously the absorbance spectra of 3DOM catalysts (left) and the reflectance spectrum of 3DOM TiO₂ with stop band maxima at 400 nm (right)

The band gap energy (E_g) of photocatalysts are estimated according to the Kubelka-Munk equation: $\alpha hv = \text{const}(hv - E_g)^2$, where $\alpha = (1-R)^2/2R$, $R = 10^{-A}$ and A is an optical absorption [78, 99]. Plotting $(\alpha hv)^{1/2}$ vs $h\nu$ based on the spectral response in Figure 2-6(A) gives the extrapolated intercept corresponding to the E_g value, as shown in Figure 2-6(B). E_g value of 3DOM TiO₂ was calculated as 2.90 eV, which is smaller than anatase TiO₂ (3.2 eV). E_g values of Pt-TiO₂, rGO-TiO₂ and Pt/rGO-TiO₂ catalysts are 2.75, 2.59 and 2.67 eV, which are much smaller than that of 3DOM TiO₂ (2.90 eV) [48, 100]. After modification of Pt or rGO, the band gap was significantly narrowed in these hybrid materials, due to electronic interaction between TiO₂ and Pt nanoparticles and/or rGO [79].

2.3.2 Photodegradation of methyl orange

The photocatalytic performance of the samples has been examined in terms of degradation of MO in an aqueous solution under visible-light irradiation. The degradation curves of MO over

time are shown in Figure 2-7(A). The photocatalytic performance can be affected by many factors, including light adsorption, electron-hole pairs life, morphology, crystallinity, crystallite size, etc. The overall photocatalytic performance results from a synergistic effect of several key factors [101]. 3DOM structure not only extends TiO₂ light adsorption, but also provides more active surface area and improved mass transfer, therefore, in 120 min about 25% MO degraded over 3DOM TiO₂. 3DOM TiO₂ modified by only Pt NPs or rGO showed enhanced photocatalytic activity, and by comparison, rGO-TiO₂ (53% removal) exhibited better photocatalytic performance than Pt-TiO₂ (32% removal), which was presumably benefited from the high charge separation and adsorption capacity of rGO relative to Pt NPs. Pt/rGO-TiO₂ showed highest photocatalytic degradation efficiency about 80% after 120 min, indicating a synergetic effect between Pt NPs and rGO.

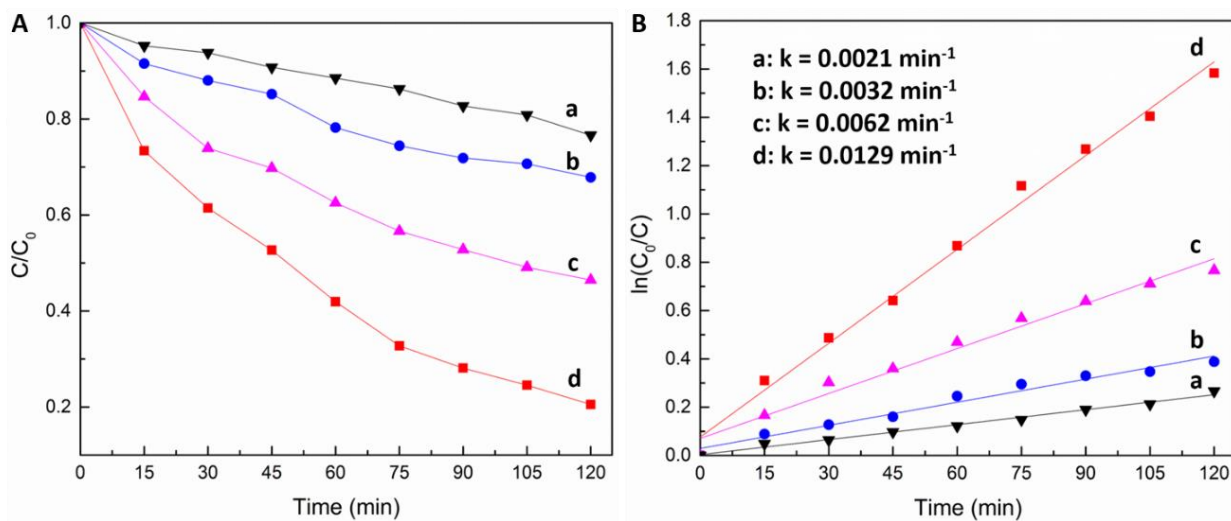


Figure 2-7 (A) Photocatalytic degradation curve and (B) kinetic curves of MO over different catalysts under visible light irradiation a) TiO₂, b) Pt-TiO₂, c) rGO-TiO₂, d) Pt/rGO-TiO₂

A first-order kinetic model was employed to fit the degradation data by using the linear transformation: $\ln(C_0/C) = kt$, where C_0 and C are MO concentrations initially and after time t respectively and k (min^{-1}) is the kinetic constant. The rate constants were determined from plot of $\ln(C_0/C)$ versus irradiation time and presented in Figure 2-7(B). As can be seen, MO degradation

kinetic constants over 3DOM TiO₂, Pt-TiO₂, rGO-TiO₂ and Pt/rGO-TiO₂ are about 0.0021, 0.0032, 0.0062 and 0.0129 min⁻¹, respectively. The photodegradation reaction kinetic constant over Pt/rGO-TiO₂ was improved about 6, 4 and 2 times, comparing to those of 3DOM TiO₂, Pt-TiO₂ and rGO-TiO₂, respectively. In accord with UV-vis diffuse reflectance spectra, Pt nanoparticle and rGO modified 3DOM TiO₂ showed improved photocatalytic activity, resulted from extended light response. What's more, simultaneous modification of Pt nanoparticles and rGO further improved light absorption and charge transfer, improved MO photodegradation by 6 times than pristine 3DOM TiO₂.

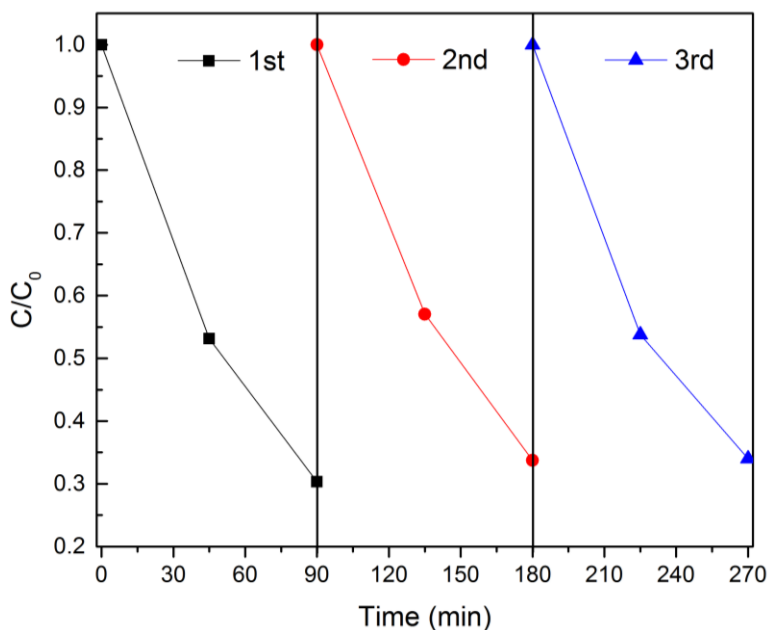


Figure 2-8 Recycling test of MO degradation over Pt/rGO-TiO₂ within 90 min visible light irradiation

The reusability of Pt/rGO-TiO₂ catalyst was tested by the photodegradation of MO under visible light. Pt/rGO-TiO₂ catalyst exhibits stable photocatalytic activity as shown in Figure 8, after three runs, the photodegradation efficiency reached 66% within 90 min, which is 5% lower than the first round. The recycling test demonstrating the good stability and high reusability of the catalyst, which may favor practical applications in water treatment.

2.3.3 Mechanism

As shown in results, the enhanced photocatalytic activity of MO photodegradation over Pt/rGO-TiO₂ composite can be ascribed to improved visible light absorbance and improved charge transfer efficiency.

First, the slow photon enhancement of 3DOM structure plays an importance role for improving photocatalytic activity. Based on the UV-vis DRS spectra, the introduction of Pt NPs and rGO can effectively extend the spectral response from UV to visible region. TiO₂ can be excited by visible light to generate electrons and holes. In the composite system, rGO acts as an acceptor of photogenerated electrons from TiO₂ and transporter to separate the photogenerated electron-hole pairs [30, 31, 79, 89, 90, 95, 102]. The work function of rGO (4.4 eV) is higher than the energy level of conduction band (CB) of anatase TiO₂ (4.2 eV), charge transfer from TiO₂ to rGO is thermodynamically favorable than recombination with holes [103, 104]. Furthermore, when Pt and rGO are in contact, the photogenerated electrons transfer from rGO to Pt is energetically favorable, due to higher work function of Pt (5.64 eV) than rGO [103, 104]. Being a high work function material with excellent electron-accepting and transport properties, rGO acts as a superhighway for the transportation of the electrons, leading to hole-electron separation. Consequently, the vectorial electron transfer route of Pt/rGO-TiO₂ can be realized along TiO₂→rGO→Pt [105].

Meanwhile, due to the formation of Schottky barrier at the interface of Pt nanoparticles and TiO₂, and larger working function of Pt than CB energy level of TiO₂, Pt nanoparticles can capture the generated electrons from TiO₂ [23, 96]. As a result, the electron-hole pairs efficiently separate and lifetime of the charge carriers is effectively lengthened. The assumed synergism between Pt

nanoparticles, rGO and 3DOM TiO₂ and the possible charge transfer mechanism in the Pt/rGO-TiO₂ composite is presented in Figure 2-9.

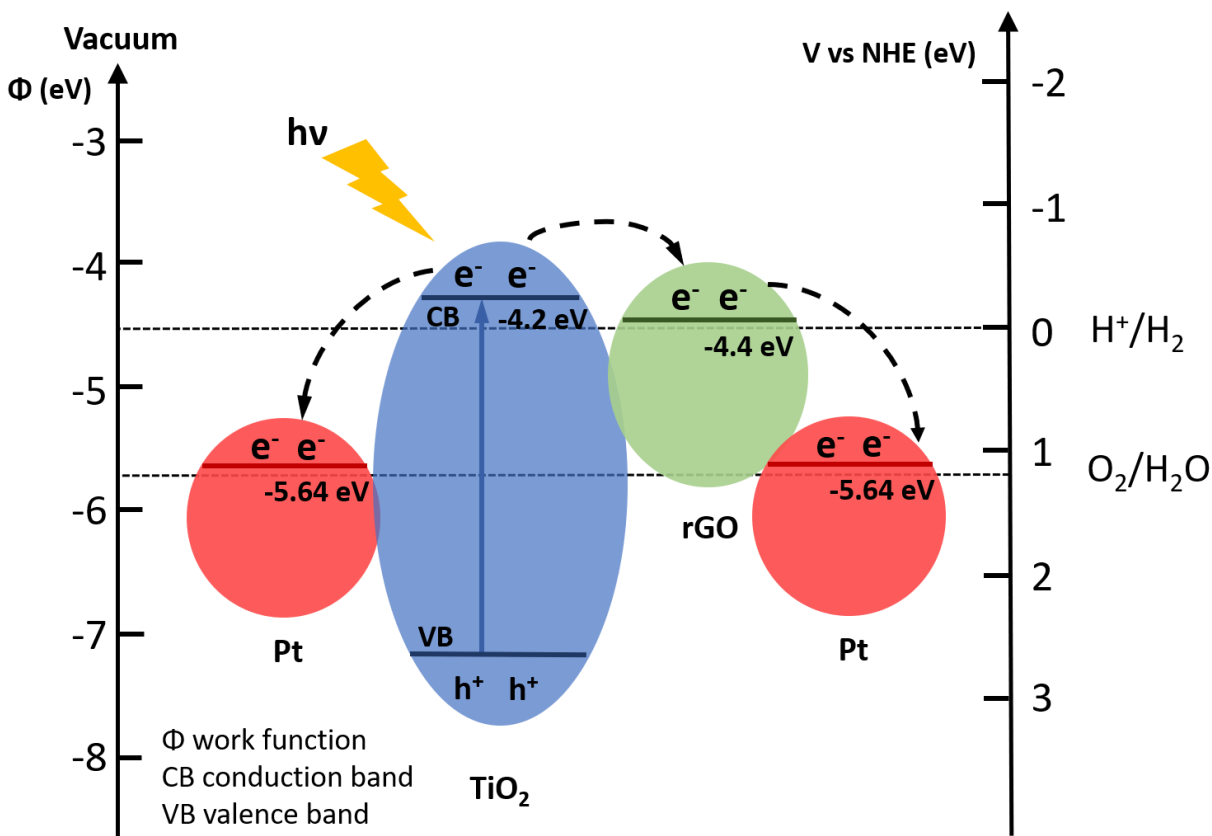
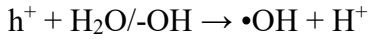
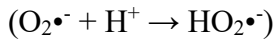
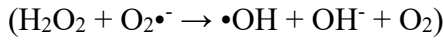
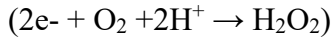
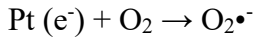
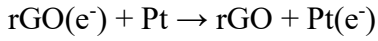
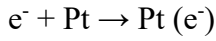
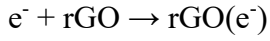
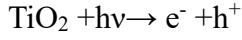


Figure 2-9 Schematic illustration of charge separation and transportation in Pt/rGO-TiO₂ photocatalyst under light illumination.

Briefly, photogenerated electrons transfer from TiO₂ through rGO to Pt nanoparticles, or directly to Pt nanoparticles though junction of Pt/TiO₂. The accumulated electrons are good reductants that could be transferred to dissolved oxygen to form superoxide anion radical (O₂^{•-}). Then O₂^{•-} subsequently transformed to active oxygen species, such as •OH, HO₂[•] and H₂O₂ [22, 70]. The remaining holes at the valence band (VB) of TiO₂ with a strong oxidation power reacted with adsorbed water or surface hydroxyl groups (-OH) to produce •OH [96, 106]. These active species possess a high oxidation power that will result in the oxidative degradation of MO [107].

Under visible light irradiation, holes play a predominant role over hydroxyl radicals in degradation of dye molecules [101]. The reaction processes are summarized as follows:



As discussed in the proposed mechanism, both rGO and Pt nanoparticles play importance roles in improving the photocatalytic activity of 3DOM TiO₂. Moreover, MO molecules are concentrated near the catalyst surface due to the high adsorption capacity of rGO, further promoted photocatalytic reaction over the ternary Pt/rGO-TiO₂ composite [31, 44, 79, 108].

2.4 Conclusion

In summary, by incorporating Pt nanoparticles and rGO with 3DOM TiO₂, a new effective photocatalyst was facilely synthesized. The excellent charge-separation property and high adsorption capacity of rGO increased the charge carrier lifetime and affinity to organic molecules. The introduction of Pt nanoparticles increased spectral response to visible light through surface plasmon resonance and suppressed charge recombination. The synergism between rGO and Pt

nanoparticles results in the novel ternary photocatalyst effective to remove MO under visible light, the photodegradation rate toward MO of resulting material is 6 times higher than 3DOM TiO₂. Moreover, the photocatalysis process is stable and reusable, making it a promising photocatalyst for practical water treatment.

CHAPTER 3 Carbon coated Fe₂O₃/TiO₂ composite as anode material for LIBs

3.1 Introduction

As mentioned in Chapter 1.3, titanium dioxide (TiO₂) is an anode material in LIBs that shows promise in high-power applications due to its highly reversible lithiation process, lack of solid electrolyte interface (SEI) formation, and relatively small volume expansion. TiO₂ is also a highly abundant material, relatively non-toxic, and chemically stable [109]. 3DOM TiO₂ has an interconnected structure which allows for efficient mass transfer, electron transfer, and contact between the electrode and electrolyte [109].

Among transition metal oxides, iron oxides are attractive anode materials for rechargeable LIBs because their high theoretical capacities of about 900-1000 mAh g⁻¹, nontoxicity, low cost and worldwide abundance. The lithium storage mechanism of iron oxides is based on a redox conversion reaction, where iron oxides are reduced to metallic nanoclusters dispersed in a Li₂O matrix upon lithiation and are then reversible restored to their initial oxidation states during delithiation. For example, the reaction mechanism of Fe₂O₃ can be described as: Fe₂O₃ + 6Li⁺ + 6e⁻ ↔ 3Li₂O + 2Fe [110]. However, capacity degradation of Fe₂O₃ anode due to its large volume expansion, low conductivity limits its application in LIBs. To overcome capacity degradation of iron oxide, optimization on Fe₂O₃ nanomaterials with different structures and modification have been studied as anode material for LIBs. Mesoporous α-Fe₂O₃ showed a high specific capacity of 1360 mAh g⁻¹ with excellent cycling stability (50 cycles) and high rate capacity [111]. Reddy et al. synthesized α-Fe₂O₃ nanoflakes on Cu foil through thermal treatment, the resulting material exhibited a stable capacity of 680 mAh g⁻¹ with no noticeable capacity fading up to 80 cycles [112]. Lin et al. Reported hydrothermally synthesized single-crystalline α-Fe₂O₃ nanorods, which

retained capacities after numerous cycles. The nanorod structure provided a short path for lithium-ion diffusion and effective accommodation of the strain generated from volume expansion [113].

Three-dimensional (3D) nanostructure enhances diffusion kinetics for lithium storage by ensuring better lithium ion transport across the electrode and more efficient electron transport. 3D structure also provides tolerance for the volume variation of the entire electrode during lithium storage. Yu employed TiO₂ nanotube arrays as 3D substrate for Fe₂O₃ nanorods, and such hierarchical architecture exhibited capacity of 400 mAh g⁻¹ over at for 50 cycles [114]. Nanosized Fe₂O₃ were loaded on single-walled carbon nanotube membrane were used as a flexible, binder-free anode of LIBs, showed a high reversible capacity of 1243 mAh g⁻¹ at a current density of 50 mA g⁻¹ and an excellent cyclic stability over 90 cycles at 500 mA g⁻¹ [115].

The introduction of carbonaceous materials has been generally accepted due to their high electronic conductivity, excellent buffering effect and mechanical strength [116]. Carbon coated Fe₂O₃ nanoparticles was loaded onto graphene nanosheets, the resulting material showed reversible capacity of 900 mAh g⁻¹ after 50 cycles, and 82% capacity retention rate [116]. Carbon coated Fe₃O₄ coaxial nanotubes showed excellent cycling performance with a specific capacity of 1020 mAh g⁻¹ after 150 cycles. The carbon coating on the surface of Fe₃O₄ nanotube improved the electronic conductivity, also prevented direct contact between organic solvent and Fe₃O₄, which contributed to high capacity retention [117]. Besides, carbon coating on Fe₂O₃ rods provided a protection for active materials from structural destruction and agglomeration, porous Fe₂O₃@C rods exhibited rate capability and cyclic stability as anode of LIBs, capacity retained at 639 mAh g⁻¹ after 500 cycles at 500 mA g⁻¹ [118].

Herein, we design a new anode material for LIBs, in which nanosized Fe_2O_3 are assembled onto 3DOM TiO_2 and further modified with carbon coating, for a high energy storage capacity and long-term stability.

3.2 Experimental

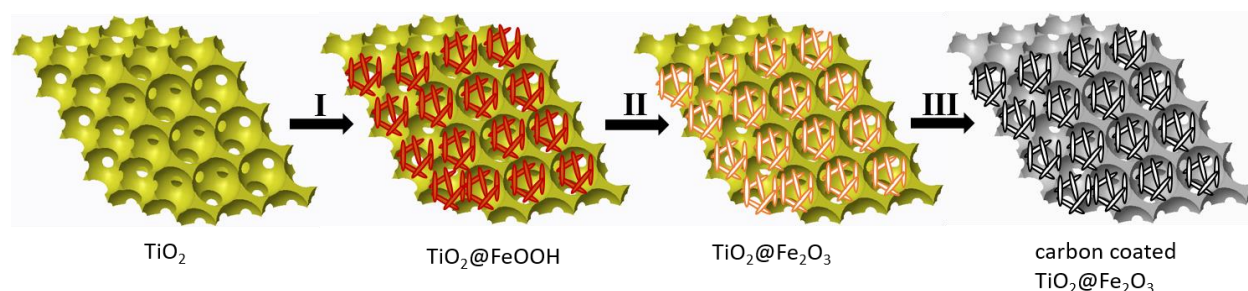


Figure 3-1 Schematic illustration of fabrication processes of carbon coated $\text{TiO}_2@Fe_2O_3$ material

3.2.1 Chemicals and materials

All chemicals were reagent grade and used without further purification. Methyl methacrylate (MMA), titanium butoxide ($\text{Ti}(\text{O}Bu)_4$), acetylacetonate (ACAC), ethanol, iron chloride hexahydrate ($\text{FeCl}_3 \cdot 6\text{H}_2\text{O}$), glucose were purchased from Sigma-Aldrich. Potassium persulfate ($\text{K}_2\text{S}_2\text{O}_8$) was purchased from Alfa Aesar. Deionized (DI) water (resistivity $> 18.0 \text{ M}\Omega$) was used for all experiments.

3.2.2 Preparation of PMMA and 3DOM TiO_2

Preparation of PMMA template and 3DOM TiO_2 are the same with method mentioned in Chapter 2.2.2 and 2.2.3

3.2.3 Preparation of $\text{TiO}_2@Fe_2O_3$

The growth of $\beta\text{-FeOOH}$ nanospindles on 3DOM TiO_2 was conducted by immersing the as-obtained 3DOM TiO_2 in 250 mL of aqueous FeCl_3 solution (80 mM) at 80°C for 6 h. The final products were washed with DI water several times before being fully dried in air at 60°C . Then the $\text{TiO}_2@FeOOH$ composite is annealed in air at 400°C for 3h with a slow ramp rate of $1^\circ\text{C}/\text{min}$.

3.2.4 Preparation of carbon coated TiO₂@Fe₂O₃

Certain amount of TiO₂@Fe₂O₃ was immersed in 10 mL glucose solution (containing same amount of glucose) for 24 h, and dried at 60 °C in air, followed by annealing at 500 °C for 3 h under Ar flow, with ramp rate of 5 °C min⁻¹. The carbonization temperature was chosen as 500 °C, because at this temperature the generated carbon could be partially graphitized to benefit the LIB performance [29].

3.2.5 Coin cell fabrication

The Li-ion battery electrode was made by mixing the carbon coated TiO₂@Fe₂O₃ composite with carbon black and alginate binder to form a uniform slurry in a weight ratio of 8:1:1 and then spread on a copper foil using a stainless-steel blade. The electrode was dried at 60 °C in a vacuum oven for 10 h. CR2032 coin cells then were assembled in an Ar-filled glovebox using the as-prepared carbon coated TiO₂@Fe₂O₃ anodes as working electrodes and lithium metal foil as counter electrodes. The electrolyte was 1 M LiPF₆ in the ethylene carbonate/ethyl methyl carbonate in 1:1 volume ratio. A Celgard 20 μm-thick monolayer polyethylene membrane was used as a separator.

3.2.6 Material Characterization

The morphology of sample was imaged with a Hitachi S-4800 scanning electron microscope (SEM) and a Hitachi H9000NAR transmission electron microscope (TEM). The crystal structure and phase state of obtained composites were determined by X-ray diffractometry (XRD) using Bruker D8 Discover A25 diffractometer with copper K_α radiation. Raman spectra were taken on a Reinshaw 1000B Raman spectrometer with a 632.8 nm He-Ne laser source. X-ray photoelectron spectroscopy (XPS) was employed to characterize the chemical states of prepared photocatalyst using Perkin Elemer PHI 5440 ESCA system with an Al K_α X-ray source. The

charge-discharge cycles were performed between 0.05-3 V at a current of 50 mAh g⁻¹ for 100 cycles with LANHE CT2001A (Land, China).

3.3 Results and discussion

3.3.1 Synthesis and characterization

The synthesis process of carbon coated TiO₂@Fe₂O₃ composite is straightforward, as schematically illustrated in Figure 3-1. 3DOM TiO₂ is firstly synthesized as nanostructured 3D substrate through CCT and sol-gel method. Then β-FeOOH nanospindles are spontaneously grown and assembled in microporous structure of 3DOM TiO₂ by hydrolysis of FeCl₃. After thermal dihydroxylation of β-FeOOH nanospindles on 3DOM TiO₂ at 400 °C, the resulting composite is coated with carbon using glucose as carbon source. A combination of techniques, described individually in detail in the Experimental Section, were used in the synthesis process, including CCT, sol-gel processing, hydrolysis.

The morphological characteristics of 3DOM TiO₂, TiO₂@Fe₂O₃ and carbon coated TiO₂@Fe₂O₃ are characterized using SEM, as shown in Figure 3-2. PMMA (330 nm) spheres are uniform in size and effectively packed into face-centered-cubic (FCC) structure. Each colloidal particle is connected with 6 surrounding particles through 6 bridges on the two-dimensional plane (Figure S2-1). 3DOM TiO₂ exhibits a highly ordered microporous structure, which replicate the three-dimensional closely-packed PMMA opals in Figure 3-2(a-b), with pore diameter about 210 nm and 25 nm wall thickness. The pore size of 3DOM TiO₂ is smaller than PMMA spheres (~330 nm) due to a shrinkage during the calcination. The small windows between the opal pores can be clearly observed in Figure 3-2(b), which replicates from the contact bridges between the neighboring PMMA spheres. The underlying layer of pores and porous walls can be clearly

observed, indicating that the sample possesses a three-dimensionally well-open, ordered and interconnected microporous network.

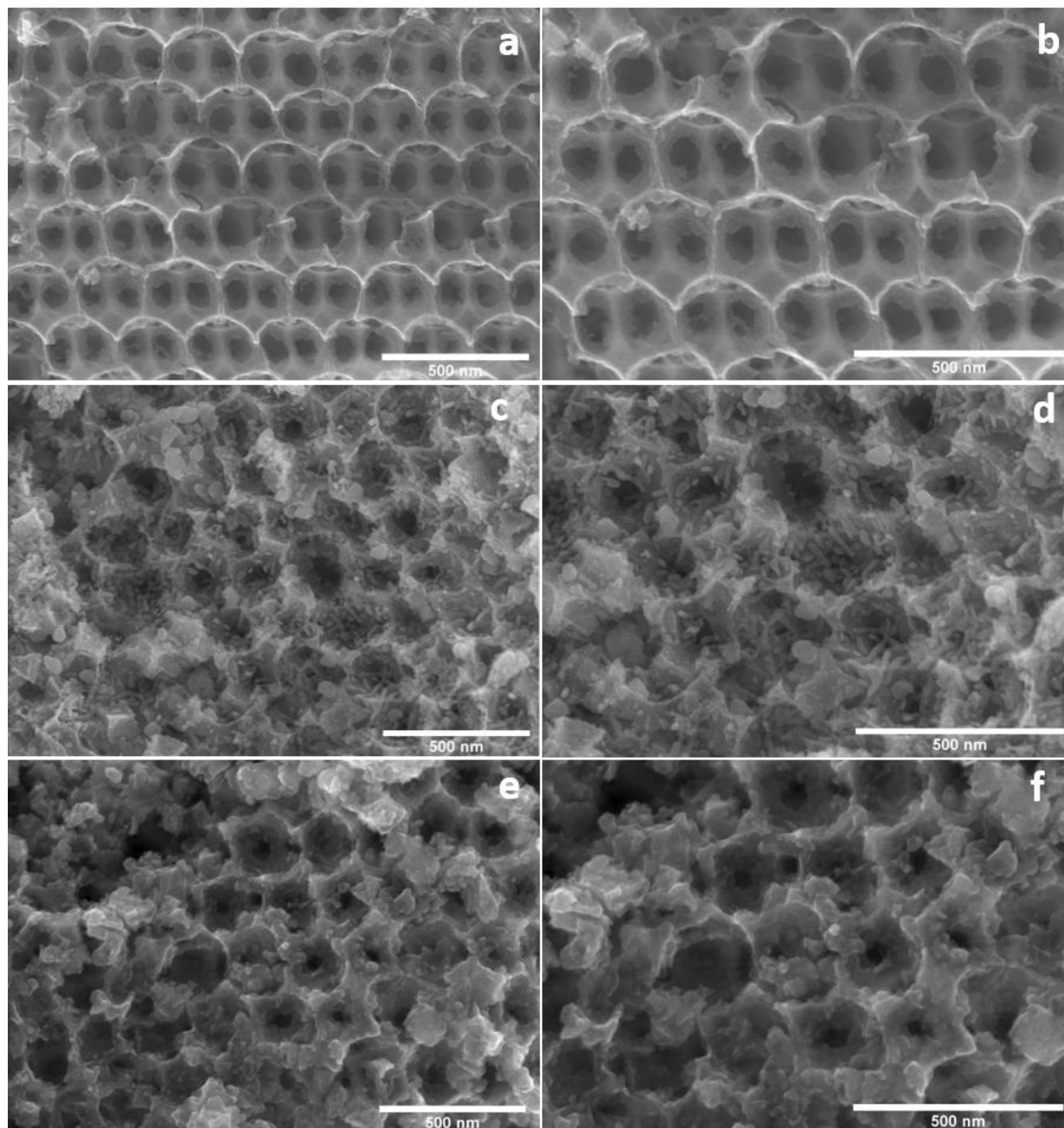


Figure 3-2 SEM images of (a)-(b) 3DOM TiO₂, (c)-(d) TiO₂@Fe₂O₃, (e)-(f) carbon coated TiO₂@Fe₂O₃

After the reaction of FeCl₃ solution and calcination, the surface of 3DOM TiO₂ is covered with large quantities of Fe₂O₃ nanospindles as a result of the hydrolysis of Fe³⁺ and simultaneously

heterogeneous growth of FeOOH on 3DOM TiO₂, as shown in Figure 3-2(c-d). The Fe₂O₃ nanospindles were with diameter about ~10 nm, while length varied from ~30 to ~100 nm. From magnified SEM image Figure 3-2(d), it can be seen that Fe₂O₃ nanospindles well dispersed on to TiO₂ macropores and walls, which provide open channels and more contact area for the transportation of lithium ions and electrons [119]. The TiO₂@Fe₂O₃ composite was further coated with a thin layer of amorphous carbon using glucose as carbon source, as seen in Figure 3-2(e-f), while the structure of Fe₂O₃ nanospindles and 3DOM TiO₂ can still be observed.

TEM analysis was also conducted to further investigate the morphology of TiO₂@Fe₂O₃ and carbon coated TiO₂@Fe₂O₃. From Figure 3-3(a) the macropores in hexagonal arrangement can be easily observed, and the porous skeleton of 3DOM TiO₂ are composed of many nanoparticles. In the pores of 3DOM TiO₂, well separated Fe₂O₃ nanospindles are grafted on the wall of pores, the size is consistent with observation in SEM images. HRTEM image (Figure 3-3(b)) shows the lattice fringes of both TiO₂ and Fe₂O₃, which indicates the highly crystalline nature of TiO₂ nanoparticles and Fe₂O₃ nanospindles. The lattice fringe with a d-spacing of 0.352 nm can be assigned to the (101) lattice plane of anatase TiO₂, and the fringe with d-spacing of 0.36 nm belongs to the (012) lattice plane of α -Fe₂O₃ nanospindles. After carbon coating, there is no apparent change in the morphology of the products, as shown in Figure 3-3(c). TEM characterization indicates that the entire surface of TiO₂@Fe₂O₃ composite has been covered with a uniform and continuous amorphous carbon over with a thickness of a few nanometers. HRTEM image (Figure 3-3(d)) shows a high crystallized nanospindle covered by a thin layer of amorphous carbon, the lattice fringe with d-spacing of 0.25 nm, which can be assigned to (110) lattice plane of α -Fe₂O₃ [111].

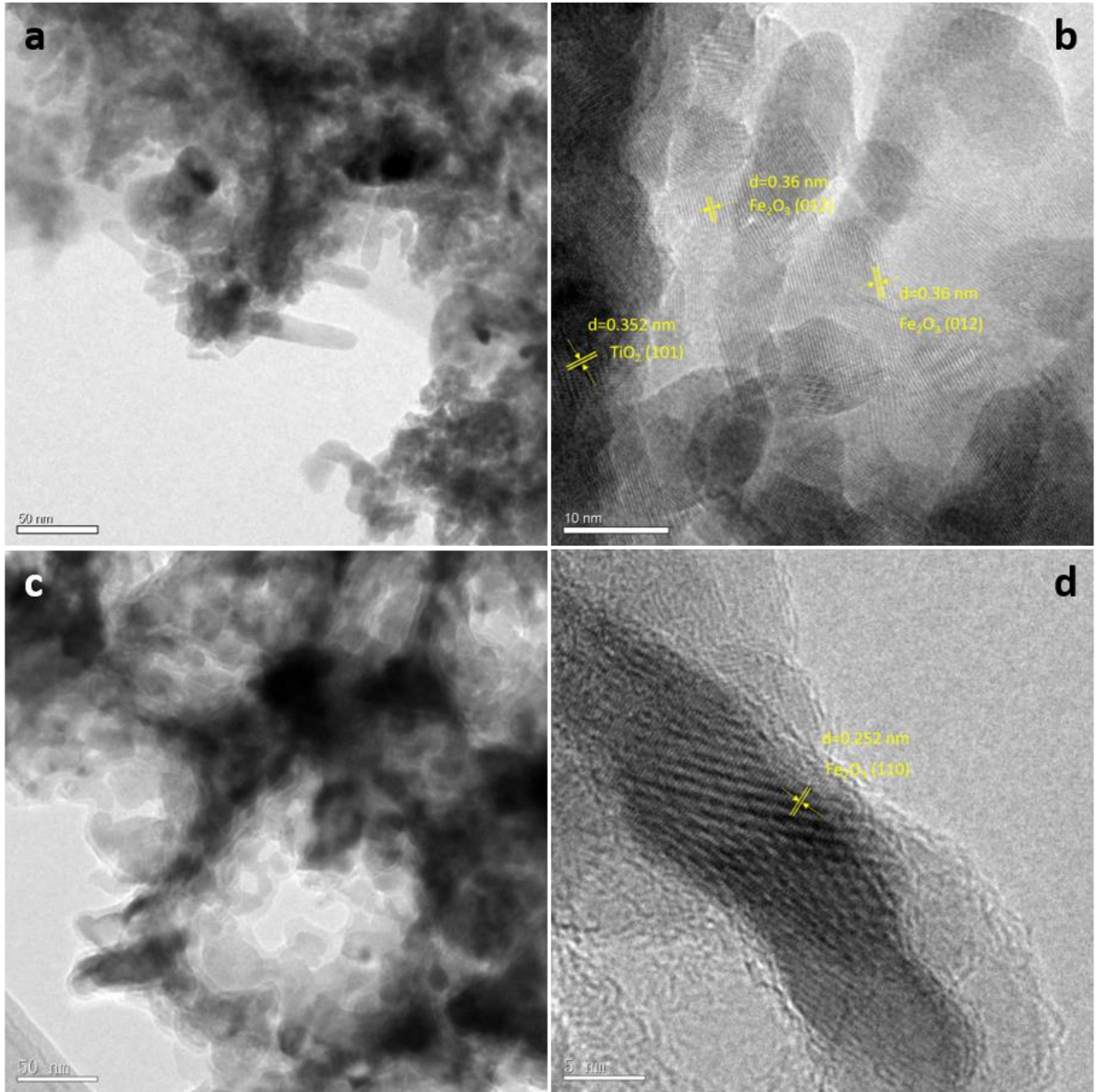


Figure 3-3 (a) TEM image and (b) HRTEM image of $\text{TiO}_2@Fe_2O_3$, (c) TEM image and (d) HRTEM image of carbon coated $\text{TiO}_2@Fe_2O_3$

The structure of obtained composites was characterized by XRD, as shown in Figure 3-4(a). XRD patterns show the main phase of TiO_2 in all samples are anatase (JCPDS 21-1272), characteristic peaks at 25.3° , 36.9° , 37.8° , 48.0° , 53.1° , 55.1° , 62.7° , 68.8° can be assigned to the plane (101), (004), (200), (105), (211), (204), (116) of anatase, respectively. After hydrolysis of Fe^{3+} ions, the new peaks are assigned to $\beta\text{-FeOOH}$ (JCPDS 75-1594), characteristic peaks at 11.9° ,

16.9°, 26.9°, 34.2°, 39.4°, 46.5°, 55.4° and 61.3° can be assigned to the plane (110), (200), (130), (400), (211), (301), (411) (620) and (002) of β -FeOOH, respectively. The transform from β -FeOOH to hematite (JCPDS 33-0664) was confirmed by XRD result, the peaks at 24.1°, 33.1°, 35.6°, 40.8°, 49.5°, 54.1°, 57.6°, 62.5° and 64.0°, which are corresponding to plane (012), (104) (110), (113), (024), (116), (018), (214) and (300) of hematite.

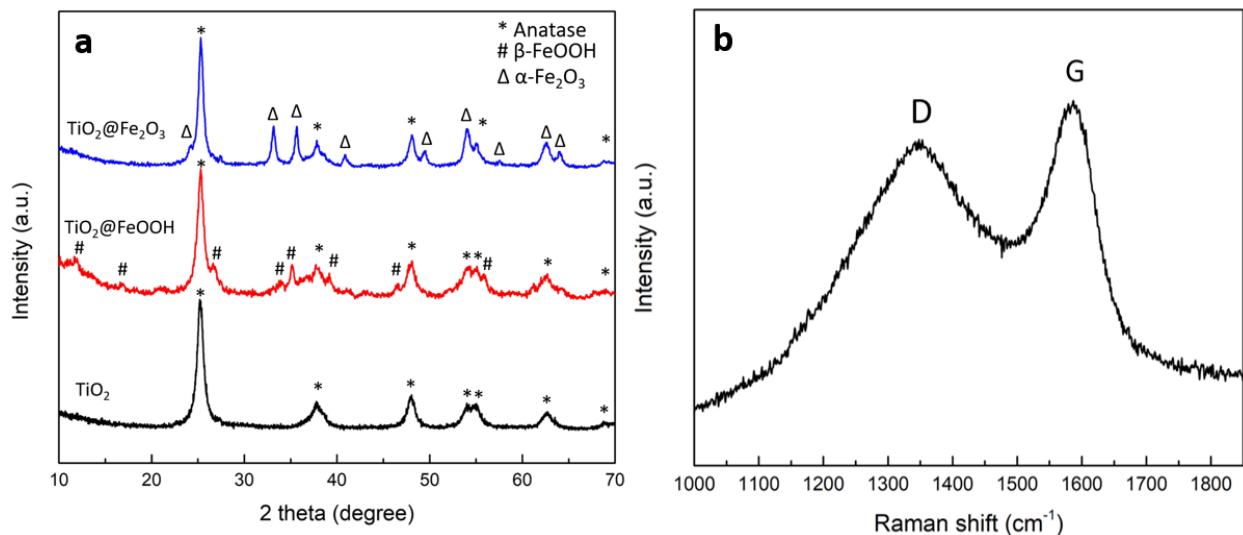


Figure 3-4 (a) XRD patterns of TiO_2 , $\text{TiO}_2@FeOOH$ and $\text{TiO}_2@Fe_2O_3$, (b) Raman spectrum of carbon coated $\text{TiO}_2@Fe_2O_3$

The Raman spectrum of carbon coated $\text{TiO}_2@Fe_2O_3$ shown in Figure 3-4(b) contains characteristic wide of carbon D and G bands of carbon at approximately 1350 and 1590 cm^{-1} [120, 121]. The D band is associated with disorder, allowing by zone edge modes of the graphite structure to become active due to the lack of long-range order in amorphous and quasi-crystalline forms of carbon materials. The G band corresponds to the stretching vibrations of sp^2 bonded carbon atoms in the basal plane of the crystalline graphite. From the Raman spectrum, the intensity of G band is higher than that of D band, showing the presence of sp^2 carbon in the carbon coating on surface of $\text{TiO}_2@Fe_2O_3$ composite [118]. The peak intensity ratio I_D/I_G can be used to evaluate

the degree of crystallinity of carbon materials [122]. The I_D/I_G obtained from Raman spectrum is 0.8, indicating of the high carbonization, which contributes to electronic conductivity.

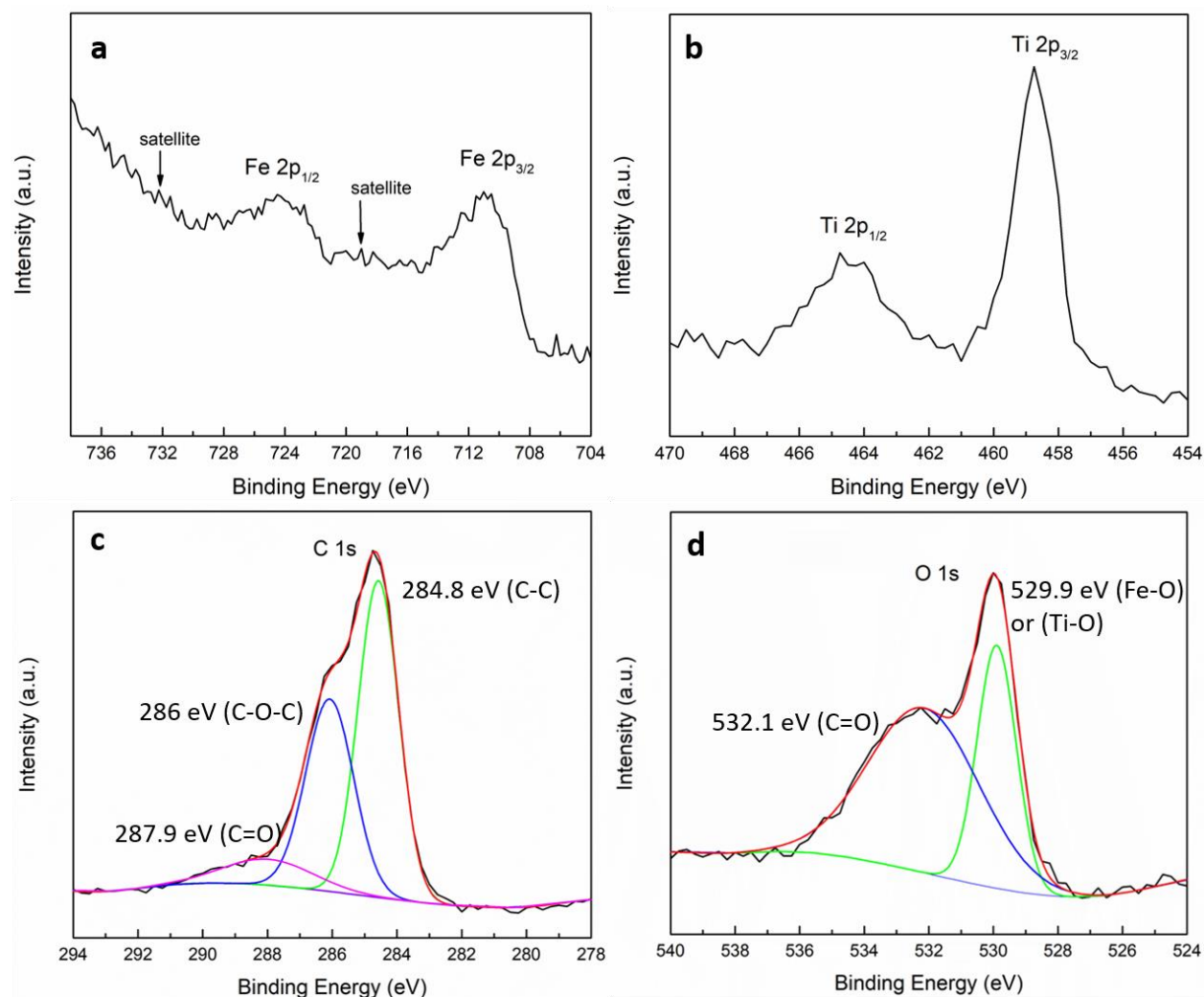


Figure 3-5 Fitted XPS spectra (a) Fe 2p, (b) Ti 2p, (c) C 1s and (d) O 1s of carbon coated $\text{TiO}_2@Fe_2O_3$ composite

To further characterization the chemical composition of the resulting carbon coated $\text{TiO}_2@Fe_2O_3$ composite, XPS was conducted. As exhibited in XPS spectrum (Figure 3-5(a)), the peaks at 710.6 and 724.1 eV in the Fe 2p spectrum are attributed to Fe 2p_{3/2} and Fe 2p_{1/2}, respectively [123, 124]. In addition, weak shakeup satellites are also observed at the higher binding energy side of the main peaks in the Fe 2p spectrum, as indicated by arrows in Figure 3-5(a), which is characteristic of Fe^{3+} in Fe_2O_3 [125]. Figure 3-5(b) shows the Ti 2p XPS spectrum, in which two

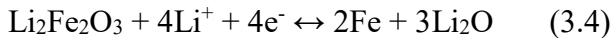
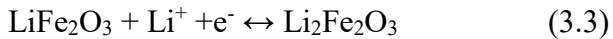
peaks at 458.7 and 464.6 eV can be assigned to Ti 2p_{3/2} and 2p_{1/2}, respectively [126]. The C 1s spectrum, shown as Figure 3-3(c), can be fitted into three component peaks centered at 284.5, 286.0 and 287.9 eV, corresponding to sp²-bonded carbon (C-C), epoxy/hydroxyls (C-O-C/C-O-H) carbon atoms and carbonyls carbon (C=O), respectively [120, 127]. As shown in Figure 3-5(d), the O 1s spectrum ranging from 536 to 528 eV can be deconvoluted into two components. The dominant peak at 529.9 can be assigned to lattice oxygen connected to Ti⁴⁺ and Fe³⁺. The peak at 532.1 eV can be assigned to C=O bond [128].

3.3.2 Battery performance

To evaluate the electrochemical performance of obtained composites, the electrodes were prepared following practical industrial procedures: mixed with conductor (carbon black) and binder, then coated onto copper foil using automatic thick film coater.

The principal reaction of reversible lithium insertion/extraction into anatase TiO₂ can be described as: TiO₂ + xLi⁺ + xe⁻ ↔ Li_xTiO₂ (3.1), with the maximum insertion coefficient *x* determined to be 0.5 due to its poor electronic conductivity and lithium ion diffusivity [129]. The theoretical charge storage capacity of anatase TiO₂ is estimated as 167.5 mAh g⁻¹ [130].

The electrochemical reactions involved in the above processes can be described as follows:



Cyclic voltammetry (CV) was used to examine the behavior for the lithium ion intercalation of obtained composites. Figure 3-6 displays the representative cyclic voltammograms (CVs) for the first four cycles of 3DOM TiO₂, TiO₂@Fe₂O₃ and carbon coated TiO₂@Fe₂O₃ electrodes, at a scan rate of 1 mV s⁻¹ in the voltage window of 0.05-3.2 V. In Figure 3-6(a), two

well defined current peaks of TiO_2 are observed at 1.55 V (cathodic sweep) and 2.2 V (anodic sweep). The peak at 1.55 V corresponds to the biphasic transition from tetragonal anatase to orthorhombic $\text{Li}_{0.5}\text{TiO}_2$ when the insertion coefficient x reaches ~ 0.5 . This result is consistent with the results reported in the literature [129-131]. For $\text{TiO}_2@\text{Fe}_2\text{O}_3$, the cathodic peaks (first sweep) located around 0.45 V and 1.25 V are observed, the peak at 1.25 eV corresponds to the lithium intercalation into Fe_2O_3 (Equation (3.1) and (3.2)), the second peak at 0.45 V is attributed to the further reduction of the $\text{Li}_2(\text{Fe}_2\text{O}_3)$ into Fe^0 and the formation of LiO_2 and SEI film [27, 119]. There are two oxidation peaks at 1.7 and 2.4 V corresponding to the extraction of Li ions from Fe_2O_3 and TiO_2 from $\text{TiO}_2@\text{Fe}_2\text{O}_3$ electrode. In the subsequent cycles, the reduction peak at 1.2 V disappears and the intensity of peak at 0.6V decreases, indicating the occurrence of some irreversible processes in the electrode materials in the first cycle ascribed to the formation of SEI film.

The CV curves of carbon coated $\text{TiO}_2@\text{Fe}_2\text{O}_3$ showed similar peaks to that of $\text{TiO}_2@\text{Fe}_2\text{O}_3$, as shown in Figure 3-6(c). At the first cycle, three reduction peaks at 0.4, 0.8 and 1.2 V are observed, corresponding to the insertion of lithium into the $\text{TiO}_2@\text{Fe}_2\text{O}_3$ and complete reduction of Fe_2O_3 to metallic Fe and SEI film formation, respectively [114]. The peaks at 1.7 and 2.2 V are ascribed to the restoration of iron oxides and the delithiation of TiO_2 . The slight shift of the two cathodic peaks to higher potentials after the first cycle is probably related to some possible activation process of the Li ion insertion in the first cycle. The subsequent curves show good reproducibility in the following cycle, demonstrating the good reversibility of the $\text{TiO}_2@\text{Fe}_2\text{O}_3$ electrode. The lithium storage mechanism in carbon coated $\text{TiO}_2@\text{Fe}_2\text{O}_3$ is similar to that in iron oxide and TiO_2 electrodes.

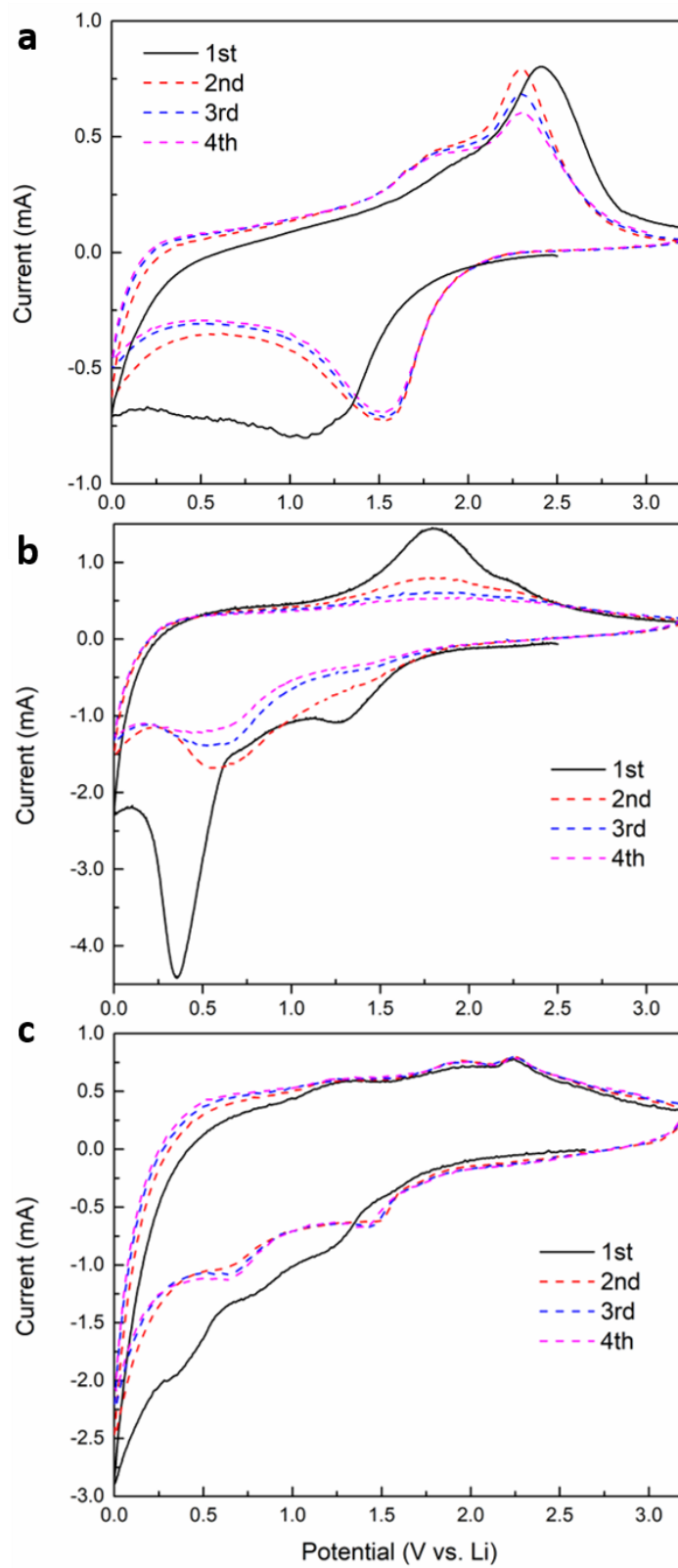


Figure 3-6 CVs at a scan rate of 1 mV s^{-1} for the first four cycles of (a) 3DOM TiO₂, (b) TiO₂@Fe₂O₃, (c) carbon coated TiO₂@Fe₂O₃ electrodes

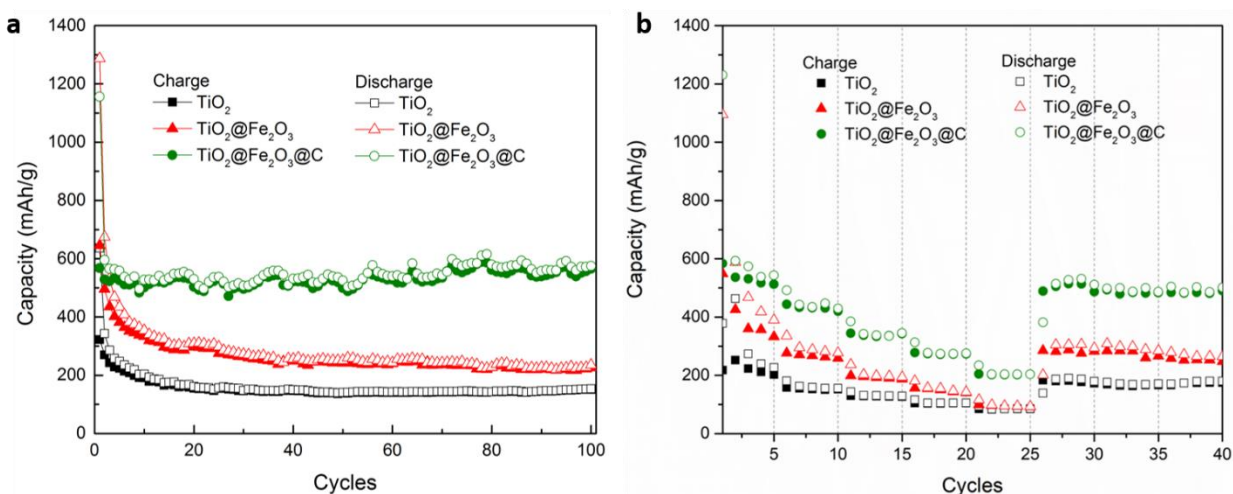


Figure 3-7 Lithium-ion battery performance of 3DOM TiO₂, TiO₂@Fe₂O₃ and carbon coated TiO₂@Fe₂O₃. (a) comparative cycling performance, taken between 0.05-3V at a current density of 50 mA g⁻¹, (b) rate capacity of electrodes at different current densities from 50 mA g⁻¹ to 800 mA g⁻¹

In order to test the applicability of the new composites in LIBs, the electrochemical lithium storage properties of carbon coated TiO₂@Fe₂O₃ were evaluated. The electrochemical properties of bare 3DOM TiO₂ and TiO₂@Fe₂O₃ were also investigated for comparison. Figure 3-7(a) shows the cycling performance of TiO₂, TiO₂@Fe₂O₃ and carbon coated TiO₂@Fe₂O₃ at a current density of 50 mA g⁻¹. The bare 3DOM TiO₂ electrode only delivers a low capacity with its initial discharge and charge capacity around 636 and 322 mAh g⁻¹, respectively. In the first 20 cycles, the discharge and charge capacity decreased to about 150 mAh g⁻¹. However, after 20 cycles the 3DOM TiO₂ electrode showed excellent cycling stability, which still delivered a capacity around 150 mAh g⁻¹. The TiO₂@Fe₂O₃ electrode on the one hand has relatively high initial discharge and charge capacities capacity around 1280 and 645 mAh g⁻¹, respectively, on the other hand, it suffered from degradation. As seen in Figure 3-7(a), the discharge capacity of the TiO₂@Fe₂O₃ electrode firstly decreased from 645 to 275 mAh g⁻¹ in 25 cycles. After the carbon coating, the cyclic stability was significantly enhanced. The carbon coated TiO₂@Fe₂O₃ electrode showed comparable initial discharge and charge capacities to that of TiO₂@Fe₂O₃, about 1155 and 570 mAh g⁻¹, respectively.

From the second cycle onwards, the discharge and charge capacity of carbon coated $\text{TiO}_2@\text{Fe}_2\text{O}_3$ retained about 575 and 565 mAh g^{-1} after 100 cycles, respectively. It is well known that the electrochemical performance is not only highly dependent on the intrinsic crystalline texture and surface properties, but also greatly related to the morphology and assembled structure of active materials. In carbon coated $\text{TiO}_2@\text{Fe}_2\text{O}_3$ structure, the Fe_2O_3 nanospindles are largely separated from each other because they are grown directly on the 3DOM TiO_2 , which improves the accessibility of lithium ions in the electrolyte [26]. The continuous and elastic amorphous carbon overlayer further strengthens the structural integrity of $\text{TiO}_2@\text{Fe}_2\text{O}_3$ structure, which will improve the cycle life.

In addition to the cycling performance, the high-rate capacity is another important parameter for LIB application, especially for high-power batteries. To further evaluate the rate capability, the batteries using TiO_2 , $\text{TiO}_2@\text{Fe}_2\text{O}_3$ and carbon coated $\text{TiO}_2@\text{Fe}_2\text{O}_3$ as active materials were tested under various current density from 50 mA g^{-1} to 800 mA g^{-1} , as Figure 3-7(b) presents. The carbon coated $\text{TiO}_2@\text{Fe}_2\text{O}_3$ electrode exhibits a reasonably good cycling response at various current rates. Even at a high current density of 800 mA g^{-1} , carbon coated $\text{TiO}_2@\text{Fe}_2\text{O}_3$ electrode can also deliver a reversible capacity of 250 mAh g^{-1} , which is much higher compared to $\text{TiO}_2@\text{Fe}_2\text{O}_3$ and TiO_2 ($\sim 100 \text{mAh g}^{-1}$). The improved performance is contributed to rationally designed hierarchical nanostructures, the excellent stability of TiO_2 and the presence of carbon coating.

Figure 3-8 presents the discharge-charge profiles of 3DOM TiO_2 , $\text{TiO}_2@\text{Fe}_2\text{O}_3$ and carbon coated $\text{TiO}_2@\text{Fe}_2\text{O}_3$ electrodes at a rate of 50 mA g^{-1} , at 1, 5, 10, 25, 50, 75, 100 cycles.

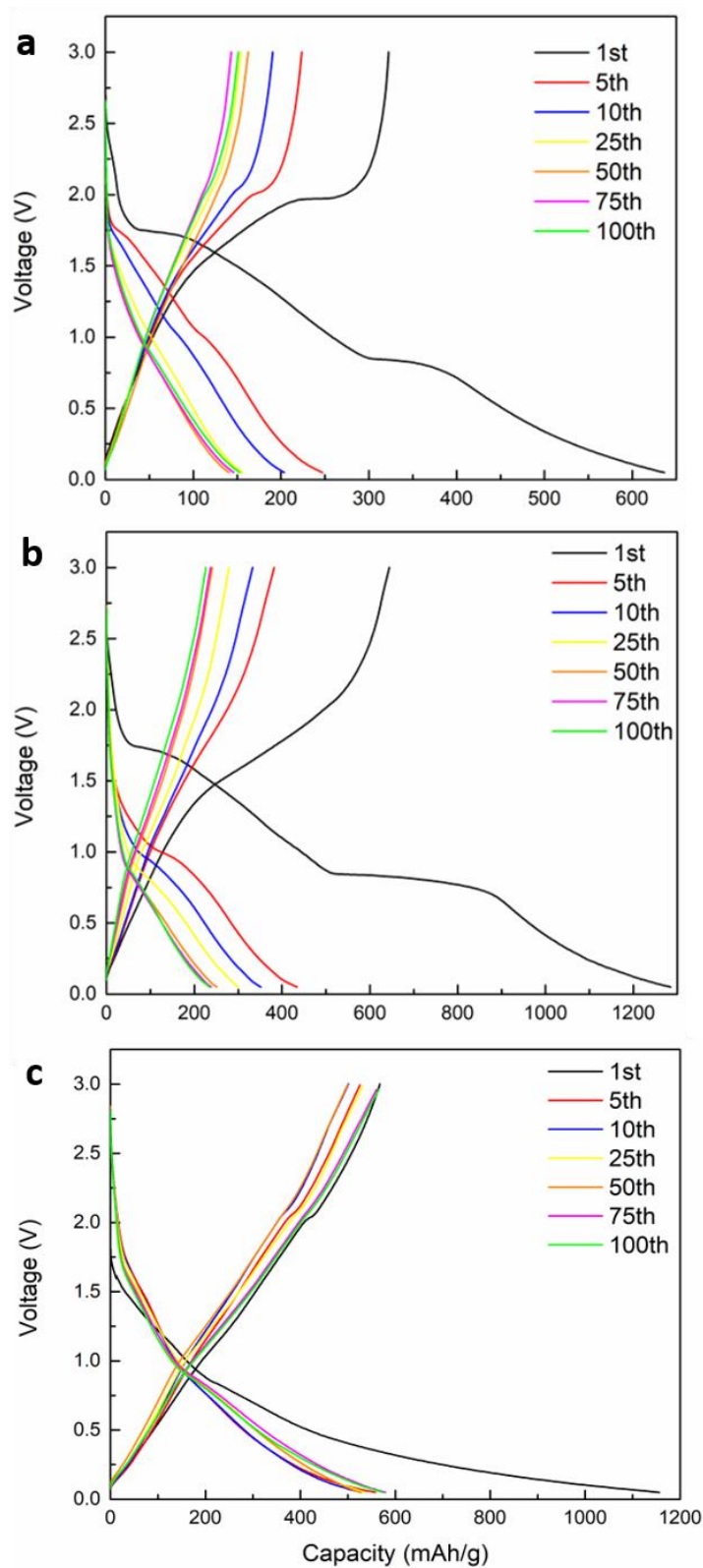


Figure 3-8 Galvanostatic discharge/charge profiles of (a) 3DOM TiO₂, (b) TiO₂@Fe₂O₃, (c) carbon coated TiO₂@Fe₂O₃ electrodes at a constant current density of 50 mA g⁻¹

For the 3DOM TiO₂ electrode, the first lithium insertion capacity is observed to be 635 mAh g⁻¹ from Figure 3-8(a). The larger capacity obtained may be ascribed to a shorter diffusion length for both the electron and Li⁺, and a larger electrode/electrolyte contact area of 3DOM TiO₂ compared with traditional materials, which facilitate the lithium ions' insertion and extraction. The discharge plateau in the discharge/charge curve can be attributed to the electrochemical behavior of the thin-film electrode [130].

As shown in Figure 3-8(b), in the discharge curve of the first cycles, there are three voltage plateaus (~1.75, ~0.8, ~0.6 V), resulting from the lithium reactions with TiO₂ and Fe₂O₃ nanomaterials [127]. The discharge-charge profiles are in good agreement of CV measurement. The first plateau at ~1.75 V is associated with the phase transition between the tetragonal TiO₂ and orthorhombic Li_xTiO₂ phases. The second plateau at ~0.8 V attributed to lithium insertion into the crystal structure of Fe₂O₃ and the formation of cubic LiFe₂O₃. An extended potential plateau appears at 0.6 V, corresponding to the reduction of Fe²⁺ to Fe⁰ and the formation of amorphous Li₂O. In the following delithiation process, a broad voltage plateau centered at ~1.7 V is observed, indicating the oxidation of Fe⁰ to Fe³⁺ [128]. It can be seen that the first discharge and charge capacities are ~1280 and ~645 mAh g⁻¹, respectively. The electrode suffered from discharge and charge capacity degradation during cycling. In the first 25 cycles, the capacities dropped fast and maintained at a lower capacity about 230 mAh g⁻¹.

In Figure 3-8(c), the plateau voltages of carbon coated TiO₂@Fe₂O₃ electrode in the first cycle are at (~0.4, ~0.8, ~1.2 V) were in good agreement with the oxidation and reduction peaks the CV curves (Figure 3-6(c)). The profiles of charge-discharge were rather different during the first cycles but became similar during the following cycling. Starting from the second cycle the discharge and charge capacities were stable at around 570 mAh g⁻¹.

3.4 Conclusion

A novel composite was successfully prepared by grafting Fe₂O₃ nanospindles onto 3DOM TiO₂, followed by carbon coating using glucose as carbon source. The carbon coated TiO₂@Fe₂O₃ material was applied as electrode materials in LIBs and showed good electrochemical performance. The composite exhibits a large reversible capacity about 570 mAh g⁻¹, which is about four times of the reversible capacity of 3DOM TiO₂. In addition to the high reversible capacity, the obtained material also exhibits good cycle performance and superior rate capacity. This rationally designed composite benefits from both good stability of TiO₂, high capacity of Fe₂O₃, and good electron conductivity of carbon.

CHAPTER 4 Adsorption removal of phosphorus by zirconium modified clays

4.1 Introduction

Wastewater from municipalities and industries may contain trace amounts of phosphate [59]. Phosphorus is an essential macronutrient that encourages the growth of photosynthetic algae and cyanobacteria. Excessive amounts of phosphorus entering water bodies could cause eutrophication and subsequently stimulate blue-green algae blooms under proper conditions [132]. The removal of phosphorus is essential to prevent eutrophication of natural water bodies, especially freshwaters.

As reviewed in Chapter 1, adsorption is one of the most effective method for the removal of phosphate in water, and nanosized metal oxides have been found wide environmental applications in the adsorptive removal of contaminants in water. Among a various of metal (hydr)oxides, zirconium (hydr)oxide has strong surface complexing ability for phosphate, which make it a superior adsorbent toward phosphate [61].

Defined by the joint nomenclature committees (JNCs), clay is naturally occurring material composed primarily of fine-grained minerals, which is generally plastic at appropriate water contents and will harden when dried or fired [133]. Clays are hydrous aluminosilicates broadly defined as those minerals that make up the colloid fraction ($<2\mu\text{m}$) of soil, sediments, rocks and water [134]. The particles of clay minerals may be crystalline or amorphous, platy or fibrous. Clay structure is layered with interlayer space and the layers may be electrically neutral or charged [135]. Large specific surface area, chemical and mechanical stability, layered structure, high cations exchange capacity (CEC), low-cost, an abundant availability, non-toxic nature, etc., have made the clays excellent adsorbent materials.

Clay minerals are phyllosilicates in which the individual layers are composed of a tetrahedral (T) and octahedral (O) sheet. The tetrahedral sheet is a silica tetrahedral layer in which the silicon atom is equidistant from four oxygens or possibly hydroxyls arranged in the form of a tetrahedron with the silicon atom in the center. These tetrahedrons are arranged to form a hexagonal network repeated infinitely in two horizontal directions to form the silica tetrahedral sheet, shown in Figure 4-1(a). The octahedral sheet is comprised of closely packed oxygens and hydroxyls in which aluminum, iron, and magnesium atoms are arranged in octahedral coordination Figure 4-2(b).

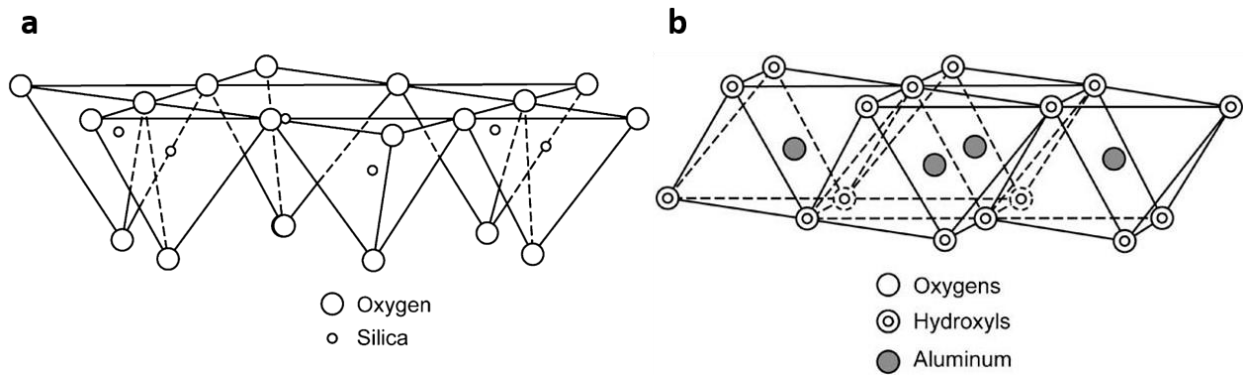


Figure 4-1 Diagrammatic sketch of the (a) tetrahedral sheet and (b) octahedral sheet

Table 4-1 Classification of clay minerals according to Grim [136]

Classification	Examples
I. Amorphous	Allophane group
II. Crystalline	
A. Two-layer type (sheet structures composed of units of one layer of silica tetrahedrons and one layer of alumina octahedrons)	Kaolinite group, halloysite group
B. Three-layer type (sheet structures composed of two layer of silica tetrahedrons and one central dioctahedral or trioctahedral layer)	Smectite group, Sodium montmorillonite, Calcium montmorillonite, Bedillite, Vermiculite, Illite group
C. Regular mixed-layer type (ordered stacking of alternate layers of different types)	Chlorite group
D. Chain-structure types (hornblende-like chains of silica tetrahedrons linked together by octahedral groups of oxygens and hydroxyls containing Al and Mg atoms)	Sepiolite, Palygorskite (attaoulgite)

Clays are divided into classes or groups such as semctites (montmorillonite, saponite), mica (illite), kaolinite, vermiculite, serpentine, pyrophyllite and sepiolite etc. Table 4-1 show Grim’s classification and lattice structure of clay minerals [136], which gives a basis for the nomenclature and differences between the various clay minerals [137]. The layer structures of different clays are shown as Figure 4-2. Interlayer space is identified as the space between two tetrahedral sheets which can be occupied by cations (such as Na^+ , Ca^{2+} , Mg^{2+}) and water.

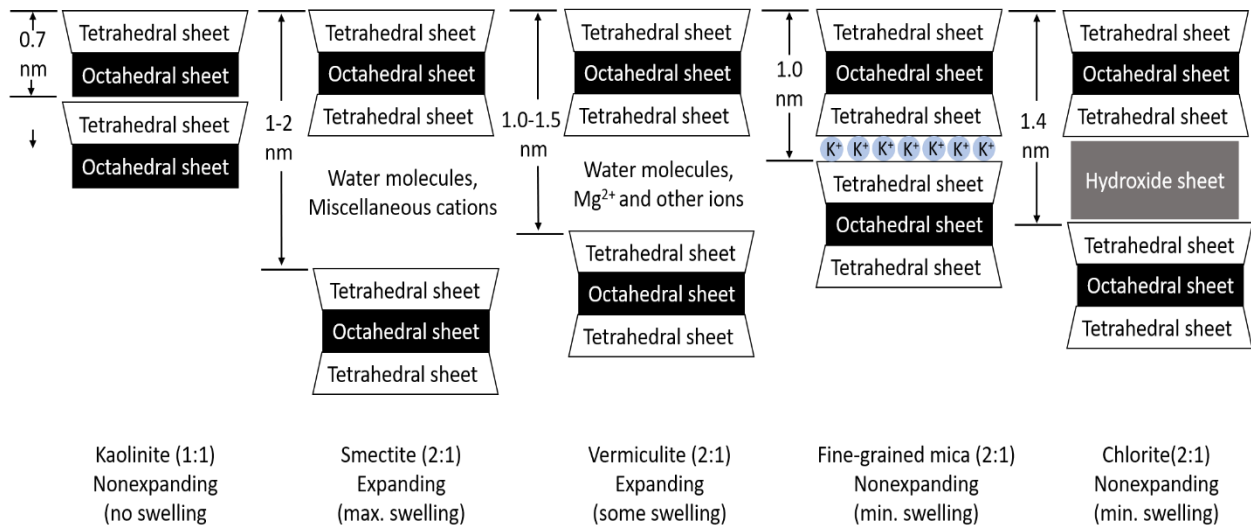


Figure 4-2 Classification of clays [138]

Modified clays have been extensively studied in various applications, including catalysts and adsorbents. Iron pillared clay was prepared by intercalation of low polymerization degree hydroxy-Fe ions into silicate layer of vermiculite [139]. The iron pillared vermiculite showed favorable photocatalytic properties and long-term stability as photo-Fenton catalyst for removal of synthetic dyes. Two zirconium pillared Portuguese clays were synthesized and studied for methane and carbon dioxide separation, both pillared clays presented high specific surface area and good thermal stability. The zirconium intercalated clays showed higher adsorbed amount of carbon dioxide, which were suitable for methane/carbon dioxide separation [140]. As for applications in water and wastewater treatment, zirconium pillared clay to remove phosphate, arsenic, dyes, and

heavy metals ions. A series of zirconium pillared montmorillonite with different zirconium contents were prepared, the formation of microporous system in the interlayer spaces improved the specific area, pore volume, and basal spacing. The modified montmorillonite was effective to remove arsenate with a high adsorption capacity of over 120 mg/g [141]. An inorganic modified bentonite with Fe ions in the interlayer space was prepared, the phosphate adsorption capacity was improved by ~350% compared to unmodified bentonite at neutral pH [132]. Montmorillonite was intercalated with aluminum and zirconium hydroxy-polycations, the resulting clays were evaluated as adsorbents for the removal of Orange II and methylene blue from aqueous solutions. These pillared clays showed potential as low-cost adsorbents for dye removal from aqueous solutions [65].

To understand the effect of clay structure as support of ZrO₂, three clays were chosen in this study: montmorillonite (MT, 2:1, max expansion), vermiculite (VT, 2:1, some expansion) and kaolinite (KT, 1:1, no expansion).

Montmorillonite is a three-layer (2:1) clay, which is composed of unites made up of two silica tetrahedral sheet with a central alumina octahedral sheet. The net layer charge of montmorillonite is -0.8 charge/unit cell, the resulting negative net charge is balanced by exchangeable cations adsorbed between the unit layers and around their edges. The bonding between two tetrahedral sheets is very weak, substitutions mainly take place in the octahedral sheets. Water and exchangeable ions can enter between the two tetrahedral sheets, where is separated from the interlayer spacing where cations balancing the excess negative charge are present [15].

Vermiculite also has a 2:1 type structure, with a medium shrink-swell capacity. Both montmorillonite and vermiculite have high cation exchange capacity due to the substitution of Si⁴⁺

and Al^{3+} [142]. In vermiculite, most of the cation substitutions take place in tetrahedral sheets, such arrangement limits the potential of this mineral to expand its interlayer space.

Kaolinite is a two-layer (1:1) clay, which consists of one tetrahedral sheet of SiO_4 and one octahedral sheet with Al^{3+} as the octahedral cation. Both the sheets combine to form a common layer such as the tips of the silica tetrahedra point towards the octahedral layer. There is no interlayer swelling of kaolinite, and the charges within the structural unit are balanced. There is very little substitution in the kaolinite lattice and kaolinite is the least reactive clay.

In this study, zirconium oxide modified clays with different zirconium oxide contents were prepared and characterized. The phosphate removal performance of zirconium modified clays was examined in detail by both the kinetics and equilibrium adsorption isotherm study, the differences in behavior of MT, VT and KT and their zirconium oxide derivatives towards adsorption of phosphate from aqueous solution.

4.2 Experimental

4.2.1 Chemicals and materials

Kaolinite (KT) was purchased from Millipore, Ca-rich montmorillonite (stx-1b, MT) was obtained from Clay Minerals Society, vermiculite (VT) was obtained from Palabora Mining Co. (South Africa). Zirconium oxychloride octahydrate ($\text{ZrOCl}_2 \cdot 8\text{H}_2\text{O}$, Alfa Aesar) was used as source of zirconium. Sodium dihydrogen phosphate (NaH_2PO_4 , Fisher Scientific), sodium hydroxide (NaOH), sodium carbonate (Na_2CO_3 , Sigma-Aldrich) were used as purchased without further purification. Humic acid (HA) was purchased from Alfa Aesar. All solution used were prepared with ultrapure water (resistance $> 18.2 \text{ m } \Omega$). Working solutions of NaH_2PO_4 were prepared from a stock solution of 100 mg P/L to give the required initial concentrations for each experiment.

4.2.2 Pretreatment of vermiculite

Vermiculite was pretreated followed reported method [143]. Briefly, 20 g vermiculite was added into 200 mL of 0.1 M HNO₃ solution, then the mixture was stirred at 90 °C for 3 h. The obtained solid was washed with water until neutral pH and then added into 200 mL of 8 g/L sodium carbonate solution, and kept at 80 °C with virous agitation for 3 h. The obtained Na-vermiculite (Na-VT) was washed by ultrapure water until neutral pH. Na-VT was dried at 105 °C and ground.

4.2.3 Preparation of Zirconium modified clays

Zirconium modified clay was prepared according to reported method [141]. Briefly, 5 g clay was firstly dispersed into 100 mL of ultrapure water and continuously stirred for 10 h to obtain a uniform clay aqueous mixture, and followed by adding desired amount of ZrOCl₂.8H₂O into suspension. The ratios between zirconium and clay were varied at 0.31 mmol/g, 0.62 mmol/g, 1.24 mmol/g and 2.48 mmol/g. The resulting suspension was stirred for 8 h. Then the pH of the suspension was adjusted to 8 by adding NaOH. After that, the suspension was stirred for another 12 h. The solid was separated by centrifugation and washed with ultrapure water, and dried in an oven at 60 °C and ground. Finally, clays modified with different Zr/clay ratios were obtained to study the effect of zirconium content on adsorption capacity. Zirconium modified clays are marked as Zr-MT, Zr-VT and Zr-KT. For example, montmorillonite with Zr/clay ratio 0.62 mmol/g was marked as Zr0.62-MT.

4.2.4 Material characterization

The morphology and of sample were imaged with scanning electron microscopy (SEM) using a Hitachi S-4800 SEM microscope. The interlayer structure of different absorbents was determined by X-ray diffractometry (XRD) using Bruker D8 Discover A25 diffractometer with copper K α radiation. Zeta-potential measurements were analyzed by a Malvern Zetasizer Nano ZS.

4.2.5 Adsorption experiments

Equilibrium adsorption isotherm experiments were carried out in a set of 52 mL polypropylene tubes at room temperature, 40 mL of NaH_2PO_4 solutions with different initial concentrations and 0.04 g (1 g/L) of adsorbent added to each solution. The NaH_2PO_4 solutions were kept on an orbital shaker at 300 rpm (Thermo Scientific) to ensure good contact between adsorbents and phosphate in water. The pH of phosphate solution was adjusted with HCl and NaOH. For equilibrium adsorption isotherm study, the initial phosphate concentration ranged from 1 to 20 mg P/L, the solution pH was about 7 and the contact time was 24 h. For kinetic study of phosphate adsorption on zirconium modified clays, 100 mL initial concentration of phosphate of 5 mg P/L was contained in 150 mL glass beaker with 0.1 g adsorbent, the solution pH was adjusted to 7 and magnetic stirred at 300 rpm. The contact time was from 0 h to 24 h. To invest the effect of pH on the phosphate adsorption capacities, 0.04 g of the adsorbent was added into 40 mL of 5 mg P/L phosphate solution of different initial pH values, ranging from 3.0 to 11.0. The initial pH of phosphate solution was adjusted with 1M NaOH or HCl solution. To study the effect of coexisting anions on the phosphate adsorption capacities, 0.04 g of the adsorbent was added into 40 mL of 5 mg P/L phosphate solution containing 5 mM and 10 mM coexisting ions, which were prepared by dissolving sodium salt forms of Cl^- , NO_3^- , SO_4^{2-} and CO_3^{2-} into 5 mg P/L phosphate solution. To study the effect of ionic strength on the phosphate adsorption capacities, 0.04 g of the adsorbent was added into 40 mL phosphate solution with same salinity of freshwater, brackish water and seawater, by adding certain amount of NaCl into 5 mg P/L phosphate solution.

After the adsorption experiment, the adsorbent was removed by a syringe filter (Millipore PES 0.22 μm membrane). Phosphate concentration in the supernatant solution was analyzed on SEAL AutoAnalyzer 3HR, Continuous segmented Flow Analyzer (SEAL Analytical).

The phosphorus adsorption capacity for zirconium modified clays at equilibrium (q_e , mg P/g) was calculated using the Equation (4.1):

$$q_e = \frac{(c_0 - c_e)V}{m} \quad (4.1)$$

where q_e is amount of phosphorus adsorbed on adsorbent at equilibrium (mg P/g),

c_0 is initial concentration of phosphorus solution (mg P/L),

c_e is concentration of phosphorus at equilibrium (mg P/L),

m is mass of adsorbent used (g),

V is volume of phosphorus solution (L).

4.3 Results and discussion

4.3.1 Characterization of adsorbents

The SEM images of MT, VT, KT and zirconium modified clays with Zr/clay ratio 0.62 mmol/g are shown in Figure 4-3. As shown in the SEM images, all original and zirconium modified clays had coarse and irregular surfaces. The clays remained in the primitive crystal form and crystalline size of original clays. The sample MT exhibits a typical lamellar morphology with a large amount of foliated flakes, well stacked layer structure of MT can be easily observed in some regions of SEM image (Figure 4-3(a)). After zirconium modification, the layer structure of MT appeared more obvious and smoother this may be attributed to the partial delamination of MT layers, after the Zr^{4+} exchange with interlayered cations. The morphology of raw VT and KT are similar to that of MT (Figure 4-3(b-c)), however, the surface of Zr0.62-VT and Zr0.62-KT appears rougher and covered by some large particles on the surface of both VT and KT, which are assumed to be deposition of ZrO_2 on clay surface.

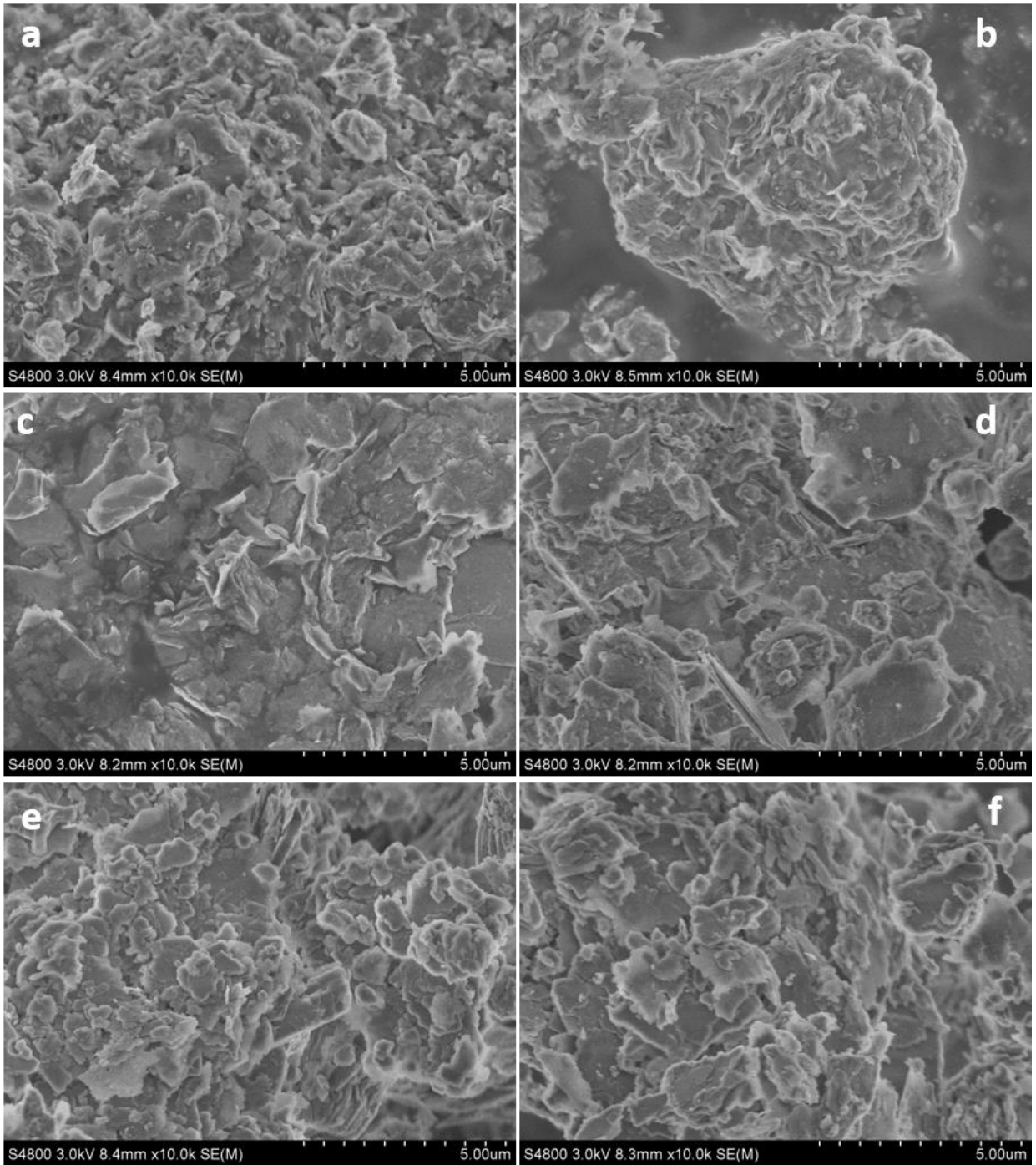


Figure 4-3 SEM images of (a) MT, (b) Zr_{0.62}-MT, (c) VT, (d) Zr_{0.62}-VT, (e) KT, (f) Zr_{0.62}-KT

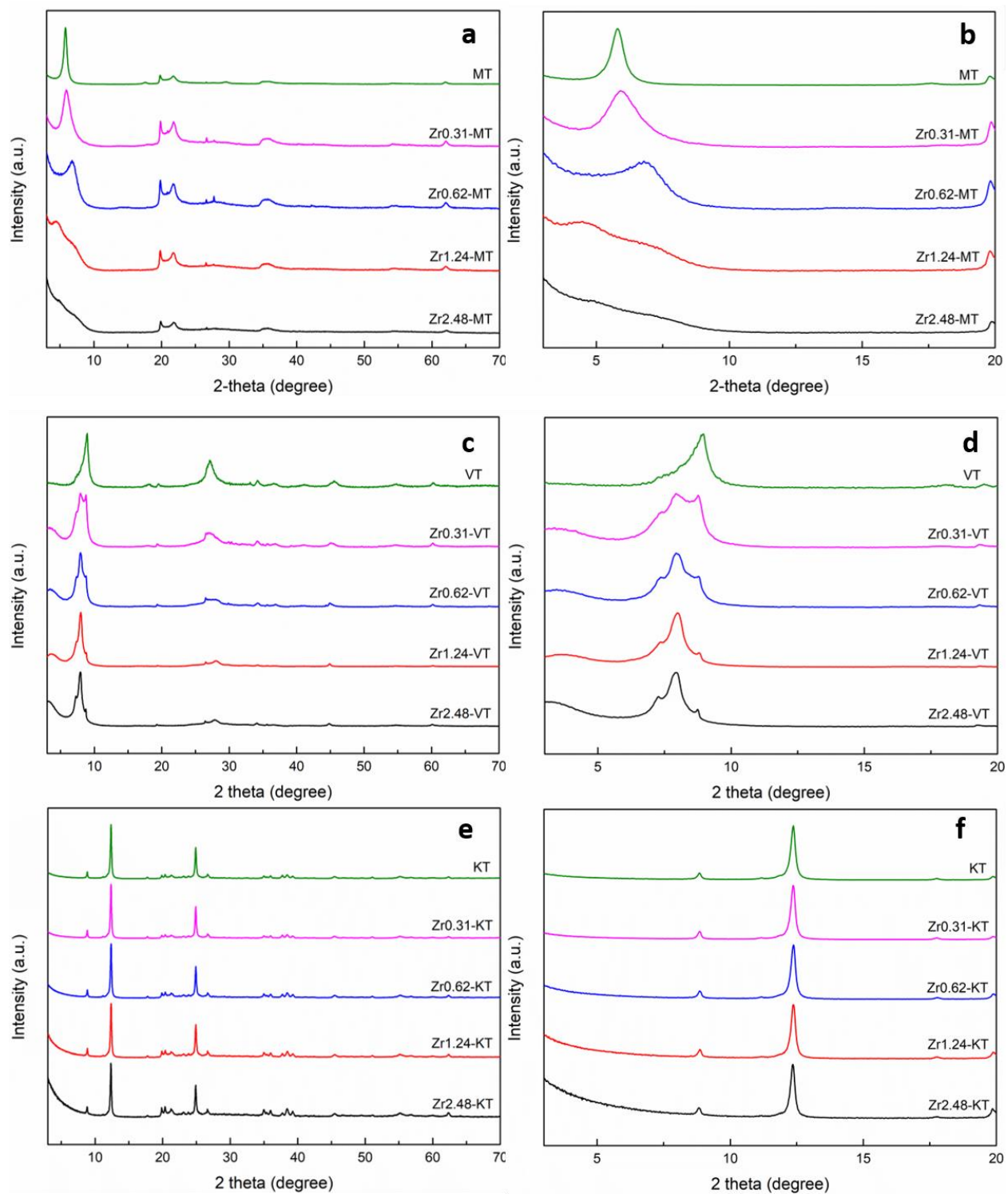


Figure 4-4 XRD patterns of zirconium modified (a) MT, (c) VT, (e) KT between 2 theta 3-70° and (b) MT, (d) VT, (f) KT between 2 theta 3-20°

The layer structures of zirconium modified MT, VT and KT were analyzed by XRD and the patterns of between 2 theta 3-70° and 3-20° are shown in Figure 4-4. For original MT, a diffraction peak at 5.8 ° was observed, which is attributable to the (001) reflection. The basal spacing (d_{001}) is 1.52 nm according to the Bragg equation ($2d \sin\theta=n\lambda$), which is normal for Ca-montmorillonite [143, 144]. The interlayer spacing was obtained by subtracting 0.96 nm, the thickness of the clay unit layer, from the XRD (001) basal spacing of clays [145, 146]. After loading with zirconium with Zr/clay ratio 0.31 mmol/g, the basal spacing of Zr0.31-MT slightly decreased to 1.50 nm, which may be caused by replacing Ca^{2+} ions with Zr^{4+} ions between clay layers. Since Zr^{4+} ion radius (0.086 nm) is smaller than Ca^{2+} ion radius (0.114 nm), the interlayer spacing decreased [147]. When Zr/clay ratio increased to 0.62, the basal spacing of Zr0.61-MT further decreased to 1.30 nm, which may be attributed to more Ca^{2+} ions replaced by Zr^{4+} ions in interlayers. For Zr1.24-MT, the main diffraction peaks became very broad and shifted to 4.33°. The corresponding basal spacing is 2.04 nm, the increase in basal spacing proves that zirconium species entered into the interlayer region of MT after the modification [148]. The intensity of (001) reflection indicates the extent of the long-range ordering of the stacking of the silicate layer [146]. With more loading of zirconium, the main peak was barely observed for Zr2.48-MT, indicating the disorder of clay layer structure after certain amount of zirconium intercalation. Other than the change of (001) reflection, no new peaks were visible after zirconium pillarization, suggesting no surface precipitation, at least crystalline forms were form [149].

Similar to MT, XRD pattern of original VT showed (001) reflection peak at 8.9°, which basal spacing was calculated as 0.99 nm. After zirconium modification, two new peaks showed up at 7.35° and 7.93° for all Zr/clay ratios, basal spacing are calculated as 1.2 nm and 1.11 nm, respectively. These two peaks are generated by zirconium species pillarized into the interlayer

region of VT after the modification. Moreover, the intensity of the peaks at 7.35° and 7.93° increase with increase of Zr/clay ratio from 0.31 to 2.48 mmol/g.

Different to MT and VT, there is no change in peak locations for KT before and after zirconium modification, and the basal spacing is 0.72 nm ($2\theta=12.25^\circ$), which is typical of kaolinite. Combining the non-expandable property of kaolinite as a 1:1 clay, it can be concluded that the modification of zirconium were all on the external surfaces of KT rather than intercalation between layers [137].

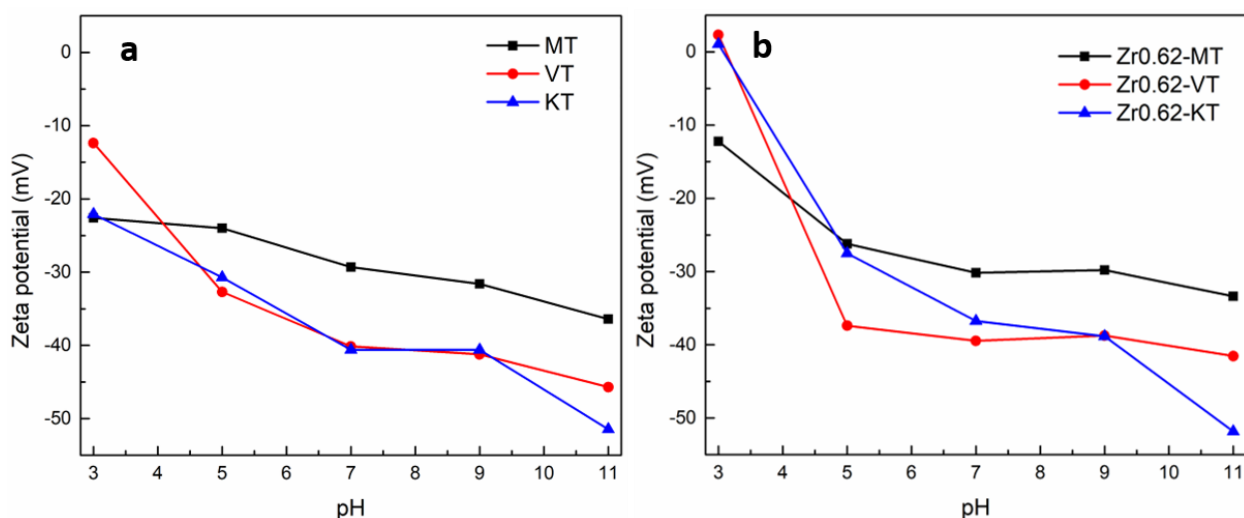


Figure 4-5 Zeta potentials of unmodified and zirconium modified clays

The zeta potentials of unmodified clays and zirconium modification clays with Zr/clay ratio 0.62 at various pH values are shown in Figure 4-5. Zeta-potential values are shown in Table 4-1. As can be seen from Figure 4-5(a), in the pH range from 3-11, MT, VT and KT are negatively charged, and the zeta potential values become more negative with increase of pH. After modified with zirconium, zeta-potential of modified clay increased within whole pH range from 3-11 due to the introduction of zirconium species, for all MT, VT and KT. Zeta-potential values of Zr0.62-MT remained below zero from pH 3-11. However, expect at pH 3, Zr0.62-VT and Zr0.62-KT showed zeta-potential above zero, these two modified clays remained below zero from pH 5-11. Thus,

under practical water and wastewater treatment conditions, the modified clays are mainly negatively charged.

Solution pH investigated in this study is 7, the dominate species of phosphate in the solution are H_2PO_4^- and HPO_4^{2-} . Zirconium modified clays have negative surface charge, thus the coulomb repulsive interaction between negatively charged adsorbents surface and the negatively charged phosphate could decrease the phosphate adsorption on zirconium modified clay.

Table 4-2 Zeta potentials of unmodified and zirconium modified clays

pH	MT	Zr0.62-MT	VT	Zr0.62-VT	KT	Zr0.62-KT
3	-22.60	-12.23	-12.36	2.33	-22.07	1.04
5	-24.00	-26.20	-32.70	-37.40	-30.70	-27.50
7	-29.33	-30.17	-40.13	-39.47	-40.60	-36.77
9	-31.60	-29.80	-41.23	-38.73	-40.60	-38.83
11	-36.40	-33.37	-45.70	-41.53	-51.47	-51.83

4.3.2 Equilibrium adsorption isotherm studies of on phosphorus adsorption by adsorbents

The adsorption capacity of zirconium modified clays on phosphorus was investigated by the equilibrium adsorption isotherm study, and the results are shown in Figure 4-6(a-c). Clays without zirconium modification showed very low phosphorus adsorption capacity with an initial phosphorus concentration of 20 mg P/L, for all three clays MT (0 mg P/g), VT (0 mg P/g) and KT (0.24 mg P/g). It clearly shows that all of the zirconium modified clays possess higher phosphorus removal capacities, as compared to untreated clays. Furthermore, adsorption isotherms of three clays followed the same trend with increase Zr content in resulting adsorbents. Take MT for example, the phosphorus uptake capacities increase from Zr0.31-MT to Zr2.48-MT, which is attributed to the greater Zr loading in the resulting adsorbents by increasing Zr/MT ratios in the initial synthetic solution.

To further evaluate the phosphorus adsorption capacity, the adsorption data was fitted with both Langmuir and Freundlich as given in Equation (4.2) and Equation (4.3) [150]:

$$q_e = \frac{q_{\max}K_Lc_e}{1+K_Lc_e} \quad (4.2)$$

$$q_e = K_Fc_e^{1/n} \quad (4.3)$$

where q_e is the amount (mg P/g) of phosphorus adsorbed at equilibrium,

c_e is the equilibrium phosphorus concentration (mg P/L) in the solution,

K_L is the Langmuir constant (L/mg), related to energy or net enthalpy of adsorption,

q_{\max} is the Langmuir monolayer adsorption capacity (mg P/g),

K_F is the Freundlich constant, related to adsorption capacity,

n is the Freundlich constant, measuring the adsorption intensity.

The parameters obtained in fitting the experimental data are summarized in Table 4-2. Three values agree with the two possible models of adsorption and they could be used to explain the significant capacity of the modified clays to quantify the adsorption. Overall, Langmuir model fitted the adsorption data better than Freundlich model, with most R^2 higher than 0.99. The Langmuir adsorption capacity (q_{\max}) for the same type of clay increased with higher Zr/clay ratio, For Zr2.48-MT, VT, KT was determined at about 15.50, 9.95 and 9.60 mg P/g. Zr2.48 -MT showed best phosphate adsorption performance, it can also be observed that the phosphate amount that Zr2.48-MT adsorbed at low equilibrium concentration was quite high. For example, when the equilibrium concentration was just 0.01 mg P/L, the phosphate amount that Zr2.48-MT adsorbed was about 9.77 mg P/g. Such a performance is beneficial to its potential applications in case the phosphate concentration is not very high.

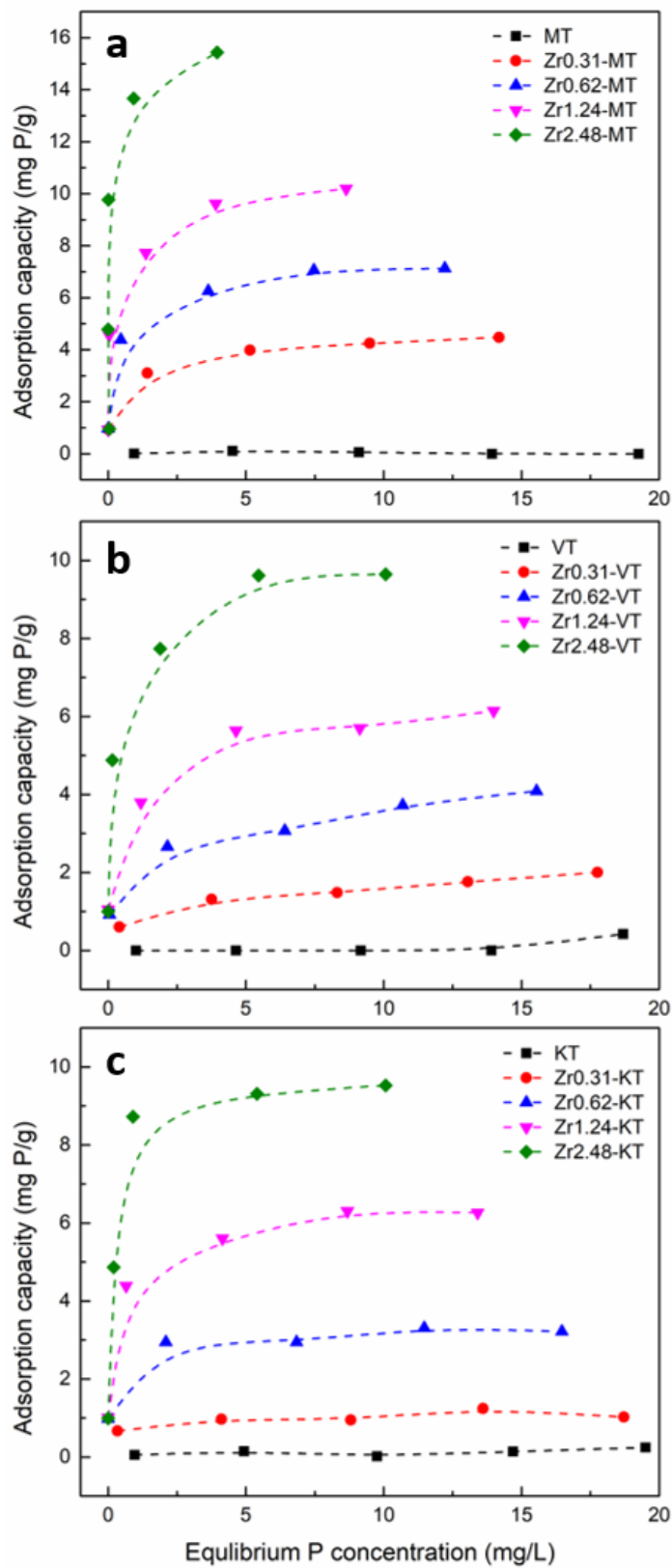


Figure 4-6 The adsorption equilibrium isotherm of phosphorus on zirconium modified clays at pH 7 and 25 °C. (a) MT, (b) VT, (c) KT (adsorbent dose 1g/L, pH 7, 25 °C)

Table 4-3 Langmuir and Freundlich isotherm constants for phosphorus adsorption on zirconium modified clays at pH 7 and T about 25 °C

Adsorbents	Langmuir coefficients			Freundlich coefficients		
	R ²	K _L (L/mg)	q _{max} (mg P/g)	R ²	1/n	K _F
MT	-	-	-	-	-	-
Zr0.31-MT	0.997	2.23	4.54	0.9961	0.20	2.76
Zr0.62-MT	0.9985	3.88	7.25	0.9768	0.25	4.37
Zr1.24-MT	0.9974	5.78	10.30	0.9225	0.26	6.93
Zr2.48-MT	0.999	26.88	15.50	0.9994	0.08	13.83
VT	-	-	-	-	-	-
Zr0.31-VT	0.9765	0.48	2.11	0.9903	0.31	0.81
Zr0.62-VT	0.9816	0.90	4.19	0.9932	0.26	2.02
Zr1.24-VT	0.9962	2.23	6.22	0.9938	0.21	3.68
Zr2.48-VT	0.9984	3.31	9.95	0.9882	0.17	6.84
KT	-	-	-	-	-	-
Zr0.31-KT	0.9743	2.98	1.09	0.8243	0.13	0.78
Zr0.62-KT	0.9975	4.63	3.27	0.9831	0.13	2.40
Zr1.24-KT	0.9985	4.24	6.37	0.9776	0.13	4.66
Zr2.48-KT	0.9997	9.65	9.60	0.7726	0.16	7.16

4.3.3 Kinetic studies on phosphorus adsorption by adsorbents

The kinetics of the phosphorus adsorption from aqueous solution onto zirconium modified clays are shown in Figure 5. It is apparent that the adsorption process could be divided into two stages, a rapid stage at the very beginning followed by a gradually slower stage until the adsorption equilibrium was achieved with the increase of the adsorption time. For example, the adsorption rate of phosphorus on Zr1.24-MT at very beginning was fast. Within just 1 h, about 92.3% phosphorus was adsorbed onto zirconium modified MT, and the remaining phosphorus concentration dropped to about 0.37 mg/L, which satisfied the discharge requirement of 0.5-1.0 mg/L. With Zr/clay ratio 0.62, phosphorus adsorption capacity was in order MT>KT>VT. With Zr ratio increased to 1.24, zirconium modified MT and KT showed similar adsorption kinetics, due to increase of q_{max}. From the kinetic study, it could be seen that 8 h was adequate for the adsorption

equilibrium to occur on Zr/clay ratio 1.24. For Zr/clay 0.68, it took longer to reach equilibrium, however, after 8 h contact time the phosphorus uptake became very close to those at equilibrium.

The adsorption kinetic data could be fitted into various rate models to provide the understanding of the adsorption mechanism. The linear pseudo-first-order rate equation could be given as Equation (4.4):

$$\log(q_e - q_t) = \log q_e - \frac{k_1 t}{2.303} \quad (4.4)$$

And the pseudo-second-order rate equation could be expressed as Equation (4.5):

$$\frac{t}{q_t} = \frac{1}{k_2 q_e^2} + \frac{t}{q_e} \quad (4.5)$$

where t is the contact time (h), q_e and q_t are the amount of phosphorus adsorbed at equilibrium and at time t , respectively. And k_1 (h^{-1}) and k_2 ($\text{g mg}^{-1} \text{h}^{-1}$) are the rate constants for pseudo-first-order and pseudo-second-order adsorption processes, respectively. The fitting curves by the pseudo-second-order rate model were demonstrated in Figure 4-7(b) and Figure 4-7(d), for Zr/clay ratio 0.62 and 1.24, respectively. The kinetics parameters obtained in fitting the experimental data are summarized in Table 4-3. It was found that the kinetics of phosphorus adsorption onto zirconium modified clays could be better fitted into the pseudo-second-order model than pseudo-first-order.

The pseudo-second-order rate model indicates a chemisorption occurred between phosphate and zirconium modified clays, involving valency forces through sharing or exchange of electrons between sorbent and sorbate, such as the replacement of -OH by phosphate [16, 148]. The initial high rate of phosphorus adsorption as shown in Figure 4-7, may be attributed to the existence of the bare surface. As the coverage increases, the number of available surface sites for adsorption decreases and the rate decreases until it reaches equilibrium [135].

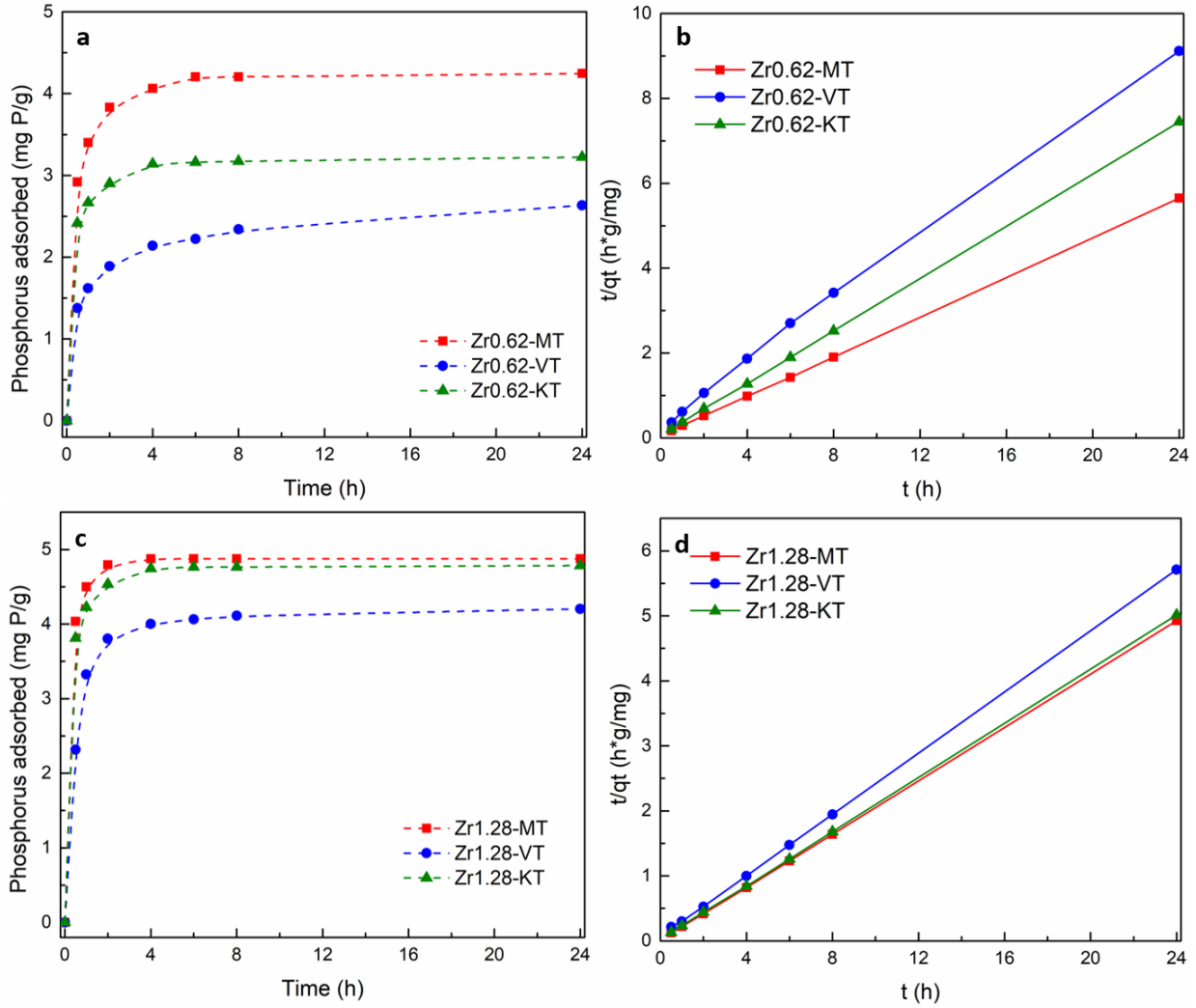


Figure 4-7 The phosphorus uptake of zirconium modified clays with the change of contact time, (a) Zr/clay ratio 0.62 mmol/g, (c) Zr/clay ratio 1.24 mmol/g. The fitting curves by the pseudo-second-order rate model of the kinetic study (b) Zr/clay ratio 0.62 mmol/g, (d) Zr/clay ratio 1.24 mmol/g (adsorbent dose at 1g/L, pH 7, 25 °C)

Table 4-4 The kinetic model parameters for the adsorption of phosphorus on zirconium modified clays at pH 7 and T about 25 °C

Adsorbents	Pseudo-first-order model			Pseudo-second-order model		
	R^2	$k_1(h^{-1})$	$q_e (mg P/g)$	R^2	$k_2(g mg^{-1} h^{-1})$	$q_e (mg P/g)$
Zr0.62-MT	0.987	2.176	4.10	1	1.103	4.29
Zr1.24-MT	0.9974	3.441	4.83	1	3.949	4.89
Zr0.62-VT	0.932	1.385	2.29	0.9985	0.408	2.71
Zr1.24-VT	0.997	1.657	4.07	0.9999	0.792	4.26
Zr0.62-KT	0.982	2.679	3.10	1	1.631	3.25
Zr1.24-KT	0.992	3.107	4.69	1	2.080	4.81

4.3.4 Influence of solution chemistry on phosphorus adsorption

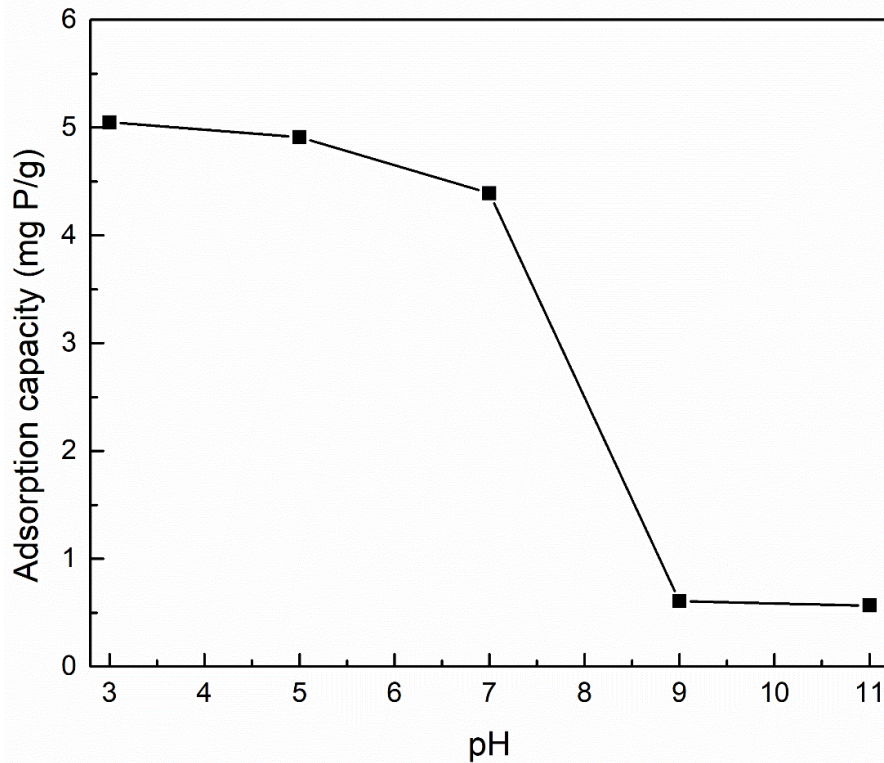
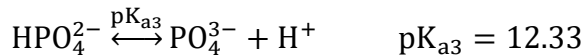
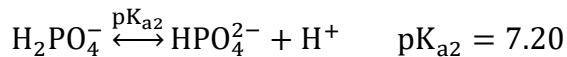
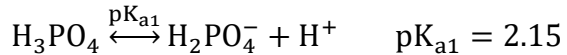


Figure 4-8 Effect of pH on phosphorus adsorption by Zr0.62-MT (initial phosphorus concentration at 5 mg P/g, adsorbent dose at 1 g/L, 25 °C, contact time 24 h)

The solution pH effect on phosphorus adsorption by Zr0.62-MT was demonstrated in Figure 4-8. The phosphate adsorption on Zr0.62-MT was dependent on solution pH. Over the examined pH range from 3.0 to 11.0, increasing pH led to monotonically decreased phosphate adsorption. It is known that phosphate acid can dissociate to form different ionic species of H_2PO_4^- , HPO_4^{2-} and PO_4^{3-} , depending on the pH of solution [61, 150, 151]. In the test pH range (3.0-11.0), H_2PO_4^- and HPO_4^{2-} are the dominant anionic species.



In the pH range from 3.0 to 7.0, the phosphate adsorption capacity of Zr0.62-MT slightly decreased from 5.0 mg P/g to 4.39 mg P/g, indicating the suitability of Zr0.62-MT as an efficient phosphate adsorbent in a wide pH range. In the acidic pH region, the protonation of adsorbent surface is favored, which could enhance the electrostatic attraction between the adsorbent surface and the phosphate anions to facilitate the phosphate adsorption. The phosphate adsorption on Zr0.62-MT is a chemisorption dominated process, and the electrostatic attraction is not a major contributor in the adsorption process. When the pH value of solution increased from 7.0 to 9.0, the phosphate adsorption capacity decreased sharply from 4.39 mg P/g to 0.61 mg P/g. At pH 11.0, the phosphate adsorption capacity decreased slightly to 0.57 mg P/g, which is 89% lower than that at pH 3.0. In the pH range from neutral to basic region, the surface charge becomes more negative with pH increases, the coulomb repulsive interaction between negatively charged Zr0.62-MT surface and negatively charged phosphate species could decrease the phosphate adsorption. Moreover, at alkaline pH, OH⁻ ions might compete phosphate ions for the adsorption sites on Zr0.62-MT surface [59, 148]. So, less adsorption occurred at higher pH region.

Coexisting anions, such as Cl⁻, NO₃⁻, SO₄²⁻ and CO₃²⁻, generally present and may interfere with phosphate adsorption in natural water and wastewater. Figure 4-9 shows the effects of coexisting, including Cl⁻, NO₃⁻, SO₄²⁻ and CO₃²⁻, on the phosphate adsorption capacity of Zr0.62-MT anions at two concentrations (5 mM and 10 mM). Among the four anions, CO₃²⁻ has strongest effect on the phosphate adsorption, in the presence of 5 mM and 10 mM CO₃²⁻, the phosphate adsorption capacity of Zr0.62-MT reduced by 7% and 44%, respectively. Conversely, the presence of Cl⁻, NO₃⁻, SO₄²⁻, slightly facilitates phosphate adsorption, even at very high concentrations compared with that of phosphate (30 times as 5 mM and 60 times as 10 mM). Thus, Zr0.62-MT

could remove phosphate effectively when competing anions existed, which is beneficial to potential industrial applications.

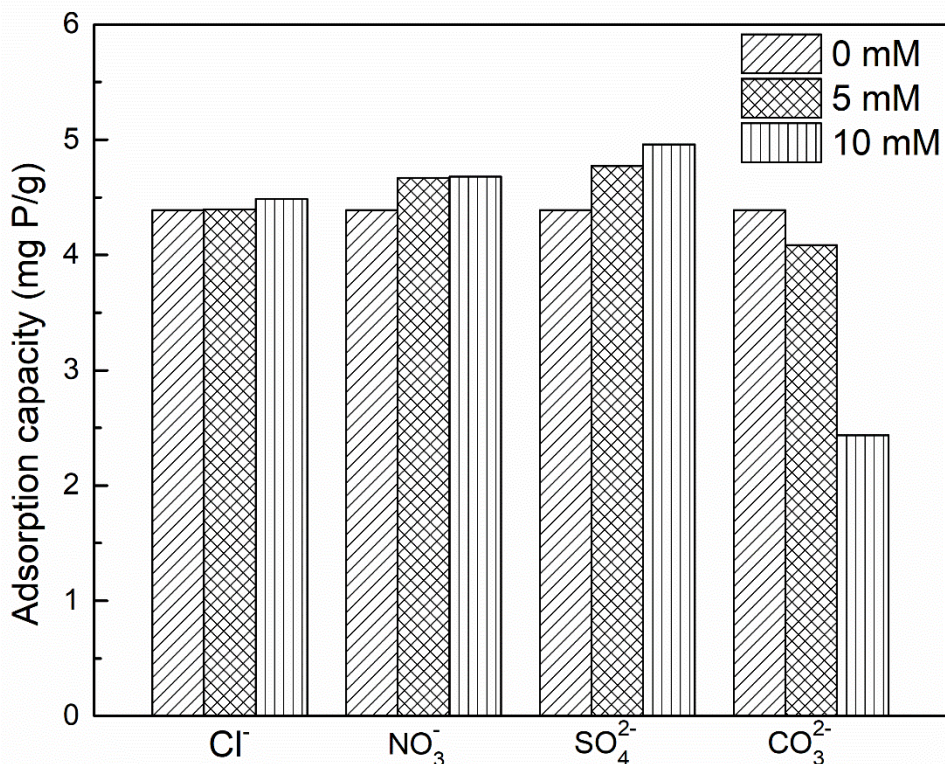


Figure 4-9 Effect of coexisting anions on the phosphorus adsorption by Zr_{0.62}-MT with phosphorus concentration at 5 mg P/L, adsorbent dose at 1 g/L, pH 7, contact time 24 h

The effect of ionic strength was also studied by adding NaCl into 5 mg P/L solution to the NaCl concentration at 8.5, 85 and 600 mM. These values simulate salinities in freshwater, brackish water and seawater, respectively. As demonstrated in Figure 4-10, the phosphate adsorption increased with the increase of the solution ionic strength. Similar observations have been reported in literature for the phosphate adsorption on ZrO₂ based absorbent [59, 61]. If phosphate form outer-sphere surface complexes through electrostatic forces, the adsorption of phosphate would decrease with the increase of ionic strength. In this study, the adsorption of phosphate would either not change or increase with the increase of ionic strength, suggesting that phosphate is removed from forming inner-sphere complexes at the absorbent surface [16, 59].

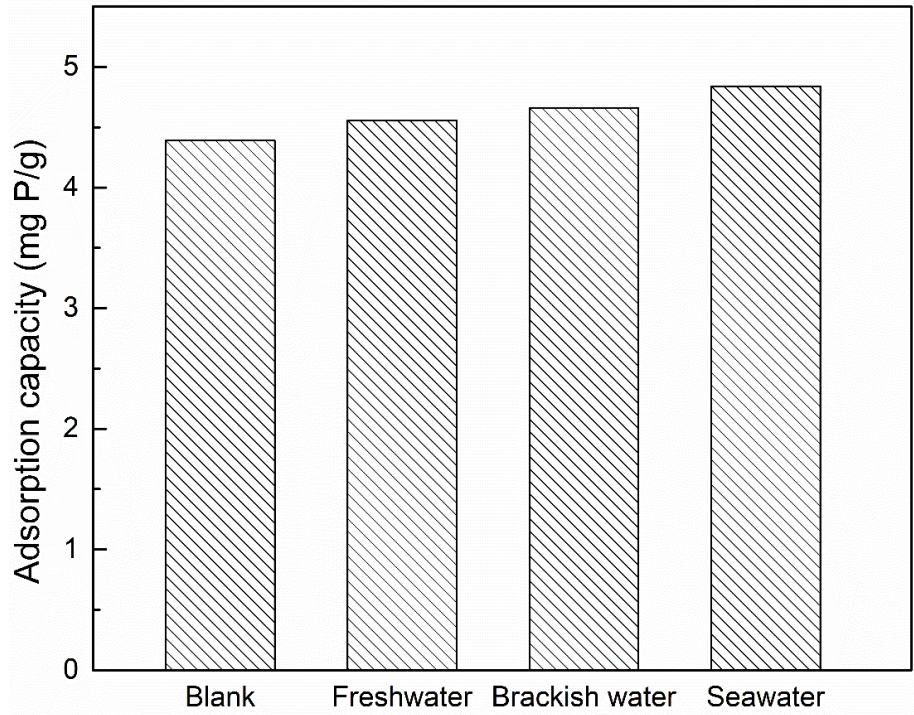


Figure 4-10 Effect of ionic strength on phosphorus adsorption by Zr_{0.62}-MT, with phosphorus concentration at 5 mg P/L, adsorbent dose at 1 g/L, pH 7, contact time 24 h

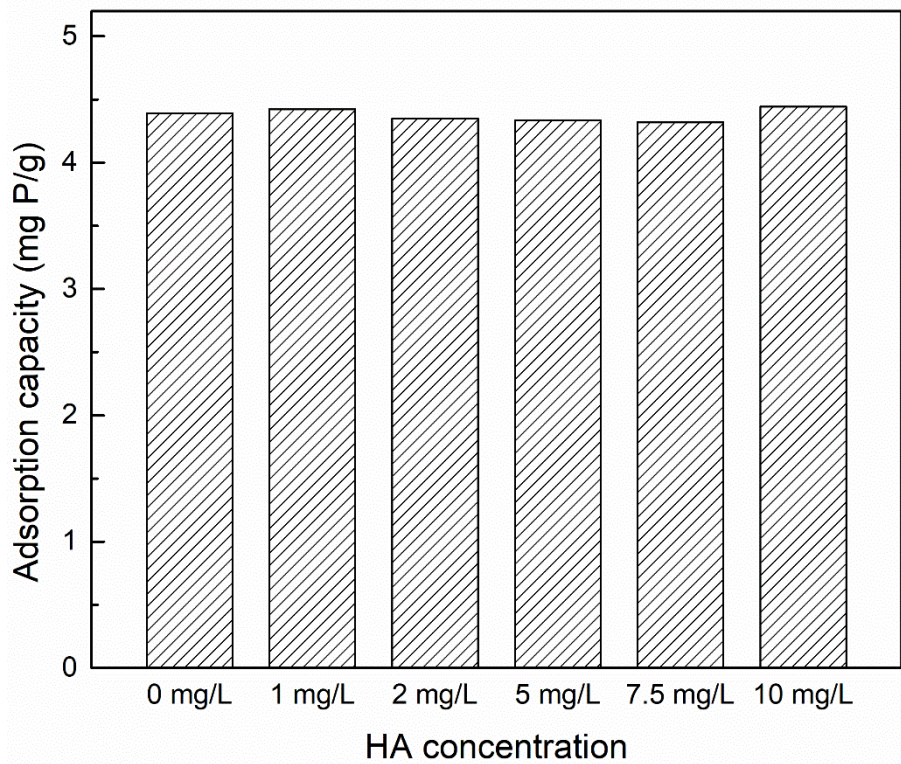


Figure 4-11 Effect of humic acid concentration on phosphorus adsorption by Zr_{0.62}-MT, with phosphorus concentration at 5 mg P/L, adsorbent dose at 1 g/L, pH 7, contact time 24 h

Phoslock (CSIRO, Australia), a commercial lanthanum ion-exchanged bentonite clay, is effective for phosphate removal from water and among the main commercial restoration products in Europe. As Dithmer et al. reported, the presence of dissolved organic carbon (DOC) interferences with the binding capacity of Phoslock. Since DOC can possibly form complexes with La^{3+} , DOC has a negatively influence on phosphate removal by Phoslock [152]. In water containing DOC, Phoslock is capable to bind less phosphate than theoretical value. To study the influence of DOC on phosphate removal on zirconium modified clays, humic acid (HA) was added into 5 mg P/L solution to concentration from 1-10 mg/L. As demonstrated in Figure 4-11, with increase of HA concentration, the phosphate adsorption capacity of Zr0.62-MT almost retained the same. Thus, this model adsorption study indicates that DOC has barely influence on zirconium modified clay adsorption capacity. It can be concluded that unlike lanthanum-based adsorbent, zirconium modified clays are favorable for phosphate removal in water containing DOC.

4.4 Conclusion

In summary, zirconium modified clays have been prepared and studied for phosphate adsorptive removal from aqueous solution. Comparing three clays, zirconium modified MT (2:1), VT (2:1) and KT (1:1) exhibit different structure and surface properties, and thus performance differently toward phosphate adsorption. MT with 2:1 layer structure and highly expansibility served best as substrate of amorphous ZrO_2 . The adsorption kinetics data of phosphate on zirconium modified clays could be well described by the pseudo-second-order model, indicating that the adsorption was through chemisorption. The experimental equilibrium data of phosphate adsorption on modified clays were fitted better by Langmuir isotherm model than the Freundlich, implying monolayer adsorption. Based on the Langmuir isotherm model, the maximum phosphate adsorption capacity for Zr2.48-MT was determined as 15.5 mg P/g. The different behaviors of

three clays were observed, yet the understanding of the mechanism is still not enough. Future work can be done on interaction between zirconium ions and different clays. The phosphate adsorption capacity is pH dependent, which is favorable in acidic and neutral pH range. Co-existing anions like Cl^- , NO_3^- , SO_4^{2-} have no significant influence on phosphate removal, but the presence of CO_3^{2-} decreases the adsorption capacity at high concentration. Unlike lanthanum-based phosphate restoration products, DOC has no significant effect on phosphate adsorption capacity on zirconium modified clays, the obtained clays can be studied for practical water treatment.

CHAPTER 5 Summary of research work and proposed future work

5.1 Summary of research work

Nanostructured metal oxide materials have offered new opportunities to design novel materials in applications of water treatment and LIBs. The objective of this study is to demonstrate high performance TiO_2 based materials as photocatalyst and anode material, and ZrO_2 based absorbents.

1. *Pt/rGO-TiO₂ photocatalyst for photodegradation of MO*

By incorporating Pt nanoparticles and rGO with 3DOM TiO_2 , a new effective photocatalyst was facilely synthesized. The composite material was thoroughly characterized by various techniques, including SEM, TEM, XRD, Raman, DRS and the photocatalytic activity was tested under visible light. The excellent charge-separation property and high adsorption capacity of rGO increased the charge carrier lifetime and affinity to organic molecules. The introduction of Pt nanoparticles increased spectral response to visible light through surface plasmon resonance and suppressed charge recombination. The synergism between rGO and Pt nanoparticles results in the novel ternary photocatalyst effective to remove MO under visible light, the photodegradation rate toward MO of resulting material is 6 times higher than 3DOM TiO_2 . Moreover, the photocatalysis process is stable and reusable, making it a promising photocatalyst for practical water treatment.

2. *Carbon coated TiO₂@Fe₂O₃ nanocomposite for LIBs*

$\text{TiO}_2@Fe_2O_3$ was synthesized through hydrolysis of $FeCl_3$ in solution, and the composite was carbon coated using glucose as carbon source. The carbon coated $\text{TiO}_2@Fe_2O_3$ material was applied as electrode materials in LIBs and showed good electrochemical performance. The composite exhibits a large reversible capacity about 570 mAh g^{-1} , which is about four times of the reversible capacity of 3DOM TiO_2 . In addition to the high reversible capacity, the obtained material also

exhibits good cycle performance and superior rate capacity. This rationally designed composite benefits from both good stability of TiO₂, high capacity of Fe₂O₃, and good electron conductivity of carbon.

3. Adsorption removal of phosphors by zirconium modified clays

In summary, zirconium modified clays have been prepared and studied for phosphate adsorptive removal from aqueous solution. Comparing three clays, zirconium modified MT (2:1), VT (2:1) and KT (1:1) exhibit different structure and surface properties, and thus performance differently toward phosphate adsorption. The adsorption kinetics data of phosphate on zirconium modified clays could be well described by the pseudo-second-order model, indicating that the adsorption was through chemisorption. The experimental equilibrium data of phosphate adsorption on modified clays were fitted better by Langmuir isotherm model than the Freundlich, implying monolayer adsorption. Based on the Langmuir isotherm model, the maximum phosphate adsorption capacity for Zr_{2.48}-MT was determined as 15.5 mg P/g.

5.2 Future work

In this thesis, three different novel nanomaterial have been demonstrated in applications of water treatment and LIBs through rational design of metal oxides. However, the synthesis process/methods are still far from satisfaction to meet the practical applications. Therefore, there is a plenty of room for discovering the new synthesis methods and optimizing existing procedures towards scale-up phase. Some recommendations for future works are summarized as following:

- 3DOM TiO₂ possess unique optimal and electrochemical properties, however, the synthesis process needs involving preparation and removal of sacrificial template, which increases cost and time towards preparation process. More works can be done to

balance cost and effort in production process and performance of the TiO₂ based materials.

- Three clays have been studied as support of ZrO₂ for adsorbents to remove phosphate in aqueous solution. The different behaviors of three clays were observed, yet the understanding of the mechanism is still not enough. Future work can be done on interaction between zirconium ions and different clays. And the obtained clays can be studied for practical water treatment.

References

1. OECD Environmental Outlook to 2050. 2012.
2. Climate change 2014: Impacts, Adaptation, and Vulnerability Intergovernmental panel on climate change. 2014, IPCC.
3. WHO/UNICEF, Meeting the MDG Drinking Water and Sanitation Target A Mid-Term Assessment of Progress. 2004, WHO: Geneva.
4. Shannon, M.A., et al., Science and technology for water purification in the coming decades. *Nature*, 2008. **452**(7185): p. 301-10.
5. Zularisam, A.W., A.F. Ismail, and R. Salim, Behaviours of natural organic matter in membrane filtration for surface water treatment — a review. *Desalination*, 2006. **194**(1-3): p. 211-231.
6. Qu, X., et al., Nanotechnology for a safe and sustainable water supply: enabling integrated water treatment and reuse. *Acc Chem Res*, 2013. **46**(3): p. 834-43.
7. Davis, M., *Water and Wastewater Engineering*. 2010: McGraw-Hill Education. 928.
8. Singh, S., K.C. Barick, and D. Bahadur, Functional Oxide Nanomaterials and Nanocomposites for the Removal of Heavy Metals and Dyes. *Nanomaterials and Nanotechnology*, 2013. **3**: p. 1.
9. Qu, X., P.J. Alvarez, and Q. Li, Applications of nanotechnology in water and wastewater treatment. *Water Res*, 2013. **47**(12): p. 3931-46.
10. World energy demand and economic outlook, in U.S. Energy Information Administration, *International Energy Outlook 2016*.
11. Omer, A.M., Energy, environment and sustainable development. *Renewable and Sustainable Energy Reviews*, 2008. **12**(9): p. 2265-2300.
12. Etacheri, V., et al., Challenges in the development of advanced Li-ion batteries: a review. *Energy & Environmental Science*, 2011. **4**(9): p. 3243.
13. Resources 2016 summary. World energy council.
14. *Reverse Osmosis and Nanofiltration - Manual of Water Supply Practices*. Second ed. 2007: American Water Works Association (AWWA).
15. Uddin, M.K., A review on the adsorption of heavy metals by clay minerals, with special focus on the past decade. *Chemical Engineering Journal*, 2017. **308**: p. 438-462.
16. Su, Y., et al., Strong adsorption of phosphate by amorphous zirconium oxide nanoparticles. *Water Res*, 2013. **47**(14): p. 5018-26.

17. Kilduff, J.E., et al., Photochemical modification of poly(ether sulfone) and sulfonated poly(sulfone) nanofiltration membranes for control of fouling by natural organic matter. *Desalination*, 2000. **132**(1-3): p. 133-142.
18. Plakas, K.V., et al., A study of selected herbicides retention by nanofiltration membranes—The role of organic fouling. *Journal of Membrane Science*, 2006. **284**(1-2): p. 291-300.
19. Yoon, Y., et al., Nanofiltration and ultrafiltration of endocrine disrupting compounds, pharmaceuticals and personal care products. *Journal of Membrane Science*, 2006. **270**(1-2): p. 88-100.
20. Radjenovic, J., et al., Rejection of pharmaceuticals in nanofiltration and reverse osmosis membrane drinking water treatment. *Water Res*, 2008. **42**(14): p. 3601-10.
21. Benitez, F.J., et al., Nanofiltration processes applied to the removal of phenyl-ureas in natural waters. *J Hazard Mater*, 2009. **165**(1-3): p. 714-23.
22. Bhatkhande, D.S., V.G. Pangarkar, and A.A.C.M. Beenackers, Photocatalytic degradation for environmental applications - a review. *Journal of Chemical Technology & Biotechnology*, 2002. **77**(1): p. 102-116.
23. Linsebigler, A.L., G. Lu, and J.T. Yates, Photocatalysis on TiO₂ Surfaces: Principles, Mechanisms, and Selected Results. *Chemical Reviews*, 1995. **95**(3): p. 735-758.
24. Hua, M., et al., Heavy metal removal from water/wastewater by nanosized metal oxides: a review. *J Hazard Mater*, 2012. **211-212**: p. 317-31.
25. Zhu, R., et al., Adsorbents based on montmorillonite for contaminant removal from water: A review. *Applied Clay Science*, 2016. **123**: p. 239-258.
26. Wang, Z., et al., Assembling carbon-coated α -Fe₂O₃ hollow nanohorns on the CNT backbone for superior lithium storage capability. *Energy Environ. Sci.*, 2012. **5**(1): p. 5252-5256.
27. Luo, J., et al., Rationally Designed Hierarchical TiO₂@Fe₂O₃ Hollow Nanostructures for Improved Lithium Ion Storage. *Advanced Energy Materials*, 2013. **3**(6): p. 737-743.
28. Ji, L., et al., α -Fe₂O₃ nanoparticle-loaded carbon nanofibers as stable and high-capacity anodes for rechargeable lithium-ion batteries. *ACS Appl Mater Interfaces*, 2012. **4**(5): p. 2672-9.
29. Liu, J., et al., Carbon/ZnO Nanorod Array Electrode with Significantly Improved Lithium Storage Capability. *The Journal of Physical Chemistry C*, 2009. **113**(13): p. 5336-5339.
30. Wang, W., et al., Enhanced photocatalytic activity of hierarchical macro/mesoporous TiO₂-graphene composites for photodegradation of acetone in air. *Applied Catalysis B: Environmental*, 2012. **119-120**: p. 109-116.

31. Du, J., et al., Hierarchically ordered macro-mesoporous TiO₂-graphene composite films: improved mass transfer, reduced charge recombination, and their enhanced photocatalytic activities. *ACS Nano*, 2011. **5**(1): p. 590-6.
32. Cheng, X., et al., Preparation of graphene film decorated TiO₂ nano-tube array photoelectrode and its enhanced visible light photocatalytic mechanism. *Carbon*, 2014. **66**: p. 450-458.
33. Venkatachalam, N., M. Palanichamy, and V. Murugesan, Sol-gel preparation and characterization of nanosize TiO₂: Its photocatalytic performance. *Materials Chemistry and Physics*, 2007. **104**(2-3): p. 454-459.
34. Dotzauer, D.M., et al., Catalytic membranes prepared using layer-by-layer adsorption of polyelectrolyte/metal nanoparticle films in porous supports. *Nano Lett*, 2006. **6**(10): p. 2268-72.
35. Rajesh, S., et al., Preparation and performance evaluation of poly (amide-imide) and TiO₂ nanoparticles impregnated polysulfone nanofiltration membranes in the removal of humic substances. *Colloids and Surfaces A: Physicochemical and Engineering Aspects*, 2013. **418**: p. 92-104.
36. Zhang, X., et al., TiO₂ nanowire membrane for concurrent filtration and photocatalytic oxidation of humic acid in water. *Journal of Membrane Science*, 2008. **313**(1-2): p. 44-51.
37. Zhang, Q., et al., Novel anti-fouling Fe₂O₃/TiO₂ nanowire membranes for humic acid removal from water. *Chemical Engineering Journal*, 2015. **271**: p. 180-187.
38. Mustafa, G., et al., Novel grafting method efficiently decreases irreversible fouling of ceramic nanofiltration membranes. *Journal of Membrane Science*, 2014. **470**: p. 369-377.
39. Kim, S.H., et al., Design of TiO₂ nanoparticle self-assembled aromatic polyamide thin-film-composite (TFC) membrane as an approach to solve biofouling problem. *Journal of Membrane Science*, 2003. **211**(1): p. 157-165.
40. Oyanedel-Craver, V.A. and J.A. Smith, Sustainable Colloidal-Silver-Impregnated Ceramic Filter for Point-of-Use Water Treatment. *Environmental Science & Technology*, 2008. **42**(3): p. 927-933.
41. Lv, Y., et al., Silver nanoparticle-decorated porous ceramic composite for water treatment. *Journal of Membrane Science*, 2009. **331**(1-2): p. 50-56.
42. Wu, J.J., et al., The synthesis of nano-silver/polypropylene plastics for antibacterial application. *Current Applied Physics*, 2012. **12**: p. S89-S95.
43. Zhou, W., et al., Ag₂O/TiO₂ nanobelts heterostructure with enhanced ultraviolet and visible photocatalytic activity. *ACS Appl Mater Interfaces*, 2010. **2**(8): p. 2385-92.

44. Tang, Y., et al., Efficient removal of herbicide 2,4-dichlorophenoxyacetic acid from water using Ag/reduced graphene oxide co-decorated TiO₂ nanotube arrays. *J Hazard Mater*, 2012. **241-242**: p. 323-30.
45. Chakrabarti, S., et al., Photo-reduction of hexavalent chromium in aqueous solution in the presence of zinc oxide as semiconductor catalyst. *Chemical Engineering Journal*, 2009. **153(1-3)**: p. 86-93.
46. Zhang, X., et al., Coupling surface plasmon resonance of gold nanoparticles with slow-photon-effect of TiO₂ photonic crystals for synergistically enhanced photoelectrochemical water splitting. *Energy & Environmental Science*, 2014. **7(4)**: p. 1409.
47. Sordello, F., et al., Photocatalytic metamaterials: TiO₂ inverse opals. *Chem Commun (Camb)*, 2011. **47(21)**: p. 6147-9.
48. Jiao, J., et al., AuPd/3DOM-TiO₂ catalysts for photocatalytic reduction of CO₂: High efficient separation of photogenerated charge carriers. *Applied Catalysis B: Environmental*, 2017. **209**: p. 228-239.
49. Wu, M., et al., High photocatalytic activity enhancement of titania inverse opal films by slow photon effect induced strong light absorption. *Journal of Materials Chemistry A*, 2013. **1(48)**: p. 15491.
50. Wu, M., et al., Three-dimensionally ordered macroporous titania with structural and photonic effects for enhanced photocatalytic efficiency. *ChemSusChem*, 2011. **4(10)**: p. 1481-8.
51. Jin, J., et al., Design of new anode materials based on hierarchical, three dimensional ordered macro-mesoporous TiO₂ for high performance lithium ion batteries. *Journal of Materials Chemistry A*, 2014. **2(25)**: p. 9699.
52. Petkovich, N.D., et al., Control of TiO₂ grain size and positioning in three-dimensionally ordered macroporous TiO₂/C composite anodes for lithium ion batteries. *Inorg Chem*, 2014. **53(2)**: p. 1100-12.
53. Collins, G., et al., Three-Dimensionally Ordered Hierarchically Porous Tin Dioxide Inverse Opals and Immobilization of Palladium Nanoparticles for Catalytic Applications. *Chemistry of Materials*, 2013. **25(21)**: p. 4312-4320.
54. Cui, H., et al., Strong adsorption of arsenic species by amorphous zirconium oxide nanoparticles. *Journal of Industrial and Engineering Chemistry*, 2012. **18(4)**: p. 1418-1427.
55. Lee, W.-J. and W.H. Smyrl, Zirconium Oxide Nanotubes Synthesized via Direct Electrochemical Anodization. *Electrochemical and Solid-State Letters*, 2005. **8(3)**: p. B7.
56. Kumari, L., et al., Synthesis, microstructure and optical characterization of zirconium oxide nanostructures. *Ceramics International*, 2009. **35(6)**: p. 2401-2408.

57. Pan, B., et al., Enhanced removal of fluoride by polystyrene anion exchanger supported hydrous zirconium oxide nanoparticles. *Environ Sci Technol*, 2013. **47**(16): p. 9347-54.
58. Hang, C., et al., As(III) and As(V) Adsorption by Hydrous Zirconium Oxide Nanoparticles Synthesized by a Hydrothermal Process Followed with Heat Treatment. *Industrial & Engineering Chemistry Research*, 2011. **51**(1): p. 353-361.
59. Liu, H., et al., Removal of phosphate by mesoporous ZrO₂. *J Hazard Mater*, 2008. **151**(2-3): p. 616-22.
60. Wang, W., et al., ZrO₂-functionalized magnetic mesoporous SiO₂ as effective phosphate adsorbent. *J Colloid Interface Sci*, 2013. **407**: p. 442-9.
61. Tang, Y., et al., Zirconia functionalized SBA-15 as effective adsorbent for phosphate removal. *Microporous and Mesoporous Materials*, 2012. **155**: p. 192-200.
62. Chen, L., et al., Preferable removal of phosphate from water using hydrous zirconium oxide-based nanocomposite of high stability. *J Hazard Mater*, 2015. **284**: p. 35-42.
63. Zong, E., et al., Adsorptive removal of phosphate ions from aqueous solution using zirconia-functionalized graphite oxide. *Chemical Engineering Journal*, 2013. **221**: p. 193-203.
64. Suzuki, T.M., et al., Adsorption and removal of oxo-anions of arsenic and selenium on the zirconium(iv) loaded polymer resin functionalized with diethylenetriamine-N,N,N',N'-polyacetic acid. *Journal of Environmental Monitoring*, 2000. **2**(6): p. 550-555.
65. Gil, A., et al., Removal of dyes from wastewaters by adsorption on pillared clays. *Chemical Engineering Journal*, 2011. **168**(3): p. 1032-1040.
66. Guerra, S.R., et al., Alkylation of benzene with olefins in the presence of zirconium-pillared clays. *Catalysis Today*, 2008. **133-135**: p. 223-230.
67. Guerra, D.L., et al., Adsorptive, thermodynamic and kinetic performances of Al/Ti and Al/Zr-pillared clays from the Brazilian Amazon region for zinc cation removal. *J Hazard Mater*, 2008. **155**(1-2): p. 230-42.
68. Abate, G. and J.C. Masini, Adsorption of atrazine, hydroxyatrazine, deethylatrazine, and deisopropylatrazine onto Fe(III) polyhydroxy cations intercalated vermiculite and montmorillonite. *J Agric Food Chem*, 2005. **53**(5): p. 1612-9.
69. Cottet, L., et al., Adsorption characteristics of montmorillonite clay modified with iron oxide with respect to methylene blue in aqueous media. *Applied Clay Science*, 2014. **95**: p. 25-31.
70. Wang, C., et al., Platinum-nanoparticle-modified TiO₂ nanowires with enhanced photocatalytic property. *ACS Appl Mater Interfaces*, 2010. **2**(11): p. 3373-7.

71. Chen, J.I., et al., Synergy of slow photon and chemically amplified photochemistry in platinum nanocluster-loaded inverse titania opals. *J Am Chem Soc*, 2008. **130**(16): p. 5420-1.
72. An, X. and J.C. Yu, Graphene-based photocatalytic composites. *RSC Advances*, 2011. **1**(8): p. 1426.
73. Kumar, D., et al., Ultrafast and Efficient Transport of Hot Plasmonic Electrons by Graphene for Pt Free, Highly Efficient Visible-Light Responsive Photocatalyst. *Nano Lett*, 2016. **16**(3): p. 1760-7.
74. Zhang, Z., et al., Direct evidence of plasmon enhancement on photocatalytic hydrogen generation over Au/Pt-decorated TiO₂ nanofibers. *Nanoscale*, 2014. **6**(10): p. 5217-22.
75. Zheng, Z., et al., Facile in situ synthesis of visible-light plasmonic photocatalysts M@TiO₂ (M = Au, Pt, Ag) and evaluation of their photocatalytic oxidation of benzene to phenol. *Journal of Materials Chemistry*, 2011. **21**(25): p. 9079.
76. Zhang, N., et al., Near-field dielectric scattering promotes optical absorption by platinum nanoparticles. *Nature Photonics*, 2016. **10**(7): p. 473-482.
77. Liang, H., Y. Zhang, and Y. Liu, Three-dimensionally ordered macro-porous Pt/TiO₂ catalyst used for water-gas shift reaction. *Journal of Natural Gas Chemistry*, 2008. **17**(4): p. 403-408.
78. Boppella, R., et al., Plasmon-Sensitized Graphene/TiO₂ Inverse Opal Nanostructures with Enhanced Charge Collection Efficiency for Water Splitting. *ACS Appl Mater Interfaces*, 2017. **9**(8): p. 7075-7083.
79. Zhang, H., et al., P25-graphene composite as a high performance photocatalyst. *ACS Nano*, 2010. **4**(1): p. 380-6.
80. Lee, J.S., K.H. You, and C.B. Park, Highly photoactive, low bandgap TiO₂ nanoparticles wrapped by graphene. *Adv Mater*, 2012. **24**(8): p. 1084-8.
81. Xia, B.Y., et al., Sandwich-structured TiO₂-Pt-graphene ternary hybrid electrocatalysts with high efficiency and stability. *Journal of Materials Chemistry*, 2012. **22**(32): p. 16499.
82. Lightcap, I.V., T.H. Kosel, and P.V. Kamat, Anchoring semiconductor and metal nanoparticles on a two-dimensional catalyst mat. Storing and shuttling electrons with reduced graphene oxide. *Nano Lett*, 2010. **10**(2): p. 577-83.
83. Zou, D., et al., Model filled polymers. V. Synthesis of crosslinked monodisperse polymethacrylate beads. *Journal of Polymer Science Part A: Polymer Chemistry*, 1992. **30**(1): p. 137-144.
84. Iida, H. and A. Igarashi, Characterization of a Pt/TiO (rutile) catalyst for water gas shift reaction at low-temperature. *Applied Catalysis A: General*, 2006. **298**: p. 152-160.

85. Gong, H.H., et al., Facile and scalable fabrication of transparent and high performance Pt/reduced graphene oxide hybrid counter electrode for dye-sensitized solar cells. *International Journal of Precision Engineering and Manufacturing*, 2014. **15**(6): p. 1193-1199.
86. Morales-Torres, S., et al., Graphene oxide-P25 photocatalysts for degradation of diphenhydramine pharmaceutical and methyl orange dye. *Applied Surface Science*, 2013. **275**: p. 361-368.
87. Wu, J., et al., Solvothermal synthesis and characterization of sandwich-like graphene/ZnO nanocomposites. *Applied Surface Science*, 2010. **256**(9): p. 2826-2830.
88. Gao, X., et al., A multilayered silicon-reduced graphene oxide electrode for high performance lithium-ion batteries. *ACS Appl Mater Interfaces*, 2015. **7**(15): p. 7855-62.
89. Zhai, C., et al., Visible-light-assisted electrocatalytic oxidation of methanol using reduced graphene oxide modified Pt nanoflowers-TiO₂ nanotube arrays. *ACS Appl Mater Interfaces*, 2014. **6**(20): p. 17753-61.
90. Cheng, P., et al., TiO₂-graphene nanocomposites for photocatalytic hydrogen production from splitting water. *International Journal of Hydrogen Energy*, 2012. **37**(3): p. 2224-2230.
91. Xiang, Q., J. Yu, and M. Jaroniec, Enhanced photocatalytic H₂-production activity of graphene-modified titania nanosheets. *Nanoscale*, 2011. **3**(9): p. 3670-8.
92. Wang, T., et al., A facile one-step synthesis of three-dimensionally ordered macroporous N-doped TiO₂ with ethanediamine as the nitrogen source. *Journal of Materials Chemistry A*, 2014. **2**(37): p. 15611.
93. Cheng, J., et al., Photoelectrocatalytic reduction of CO₂ into chemicals using Pt-modified reduced graphene oxide combined with Pt-modified TiO₂ nanotubes. *Environ Sci Technol*, 2014. **48**(12): p. 7076-84.
94. Xing, M., et al., Highly-dispersed boron-doped graphene nanosheets loaded with TiO₂ nanoparticles for enhancing CO₂ photoreduction. *Sci Rep*, 2014. **4**: p. 6341.
95. Dai, Y., et al., Graphene-wrapped TiO₂ nanofibers with effective interfacial coupling as ultrafast electron transfer bridges in novel photoanodes. *J. Mater. Chem. A*, 2014. **2**(4): p. 1060-1067.
96. Wei, Y., et al., 3D ordered macroporous TiO₂-supported Pt@CdS core-shell nanoparticles: design, synthesis and efficient photocatalytic conversion of CO₂ with water to methane. *J. Mater. Chem. A*, 2015. **3**(20): p. 11074-11085.
97. Chen, X., et al., Enhanced incident photon-to-electron conversion efficiency of tungsten trioxide photoanodes based on 3D-photonic crystal design. *ACS Nano*, 2011. **5**(6): p. 4310-8.

98. Schroden, R.C., et al., Optical Properties of Inverse Opal Photonic Crystals. *Chemistry of Materials*, 2002. **14**(8): p. 3305-3315.
99. Zhang, Y. and C. Pan, TiO₂/graphene composite from thermal reaction of graphene oxide and its photocatalytic activity in visible light. *Journal of Materials Science*, 2010. **46**(8): p. 2622-2626.
100. Lu, Y., et al., Integrating plasmonic nanoparticles with TiO₂ photonic crystal for enhancement of visible-light-driven photocatalysis. *Environ Sci Technol*, 2012. **46**(3): p. 1724-30.
101. Zhang, N., et al., Synthesis of M@TiO₂ (M = Au, Pd, Pt) Core–Shell Nanocomposites with Tunable Photoreactivity. *The Journal of Physical Chemistry C*, 2011. **115**(18): p. 9136-9145.
102. Wang, Y., et al., Microwave-assisted hydrothermal synthesis of graphene based Au–TiO₂ photocatalysts for efficient visible-light hydrogen production. *Journal of Materials Chemistry A*, 2014. **2**(11): p. 3847.
103. Gao, P., et al., High quality graphene oxide–CdS–Pt nanocomposites for efficient photocatalytic hydrogen evolution. *J. Mater. Chem.*, 2012. **22**(5): p. 2292-2298.
104. Kim, Y.K. and H. Park, Light-harvesting multi-walled carbon nanotubes and CdS hybrids: Application to photocatalytic hydrogen production from water. *Energy Environ. Sci.*, 2011. **4**(3): p. 685-694.
105. Wang, P., et al., The fundamental role and mechanism of reduced graphene oxide in rGO/Pt–TiO₂ nanocomposite for high-performance photocatalytic water splitting. *Applied Catalysis B: Environmental*, 2017. **207**: p. 335-346.
106. Zalfani, M., et al., BiVO₄/3DOM TiO₂ nanocomposites: Effect of BiVO₄ as highly efficient visible light sensitizer for highly improved visible light photocatalytic activity in the degradation of dye pollutants. *Applied Catalysis B: Environmental*, 2017. **205**: p. 121-132.
107. Ge, L., C. Han, and J. Liu, Novel visible light-induced g-C₃N₄/Bi₂WO₆ composite photocatalysts for efficient degradation of methyl orange. *Applied Catalysis B: Environmental*, 2011. **108-109**: p. 100-107.
108. Nguyen-Phan, T.-D., et al., The role of graphene oxide content on the adsorption-enhanced photocatalysis of titanium dioxide/graphene oxide composites. *Chemical Engineering Journal*, 2011. **170**(1): p. 226-232.
109. Lui, G., et al., Flexible, three-dimensional ordered macroporous TiO₂ electrode with enhanced electrode–electrolyte interaction in high-power Li-ion batteries. *Nano Energy*, 2016. **24**: p. 72-77.

110. Zhang, L., H.B. Wu, and X.W.D. Lou, Iron-Oxide-Based Advanced Anode Materials for Lithium-Ion Batteries. *Advanced Energy Materials*, 2014. **4**(4): p. 1300958.
111. Sun, B., et al., Synthesis of Mesoporous α -Fe₂O₃ Nanostructures for Highly Sensitive Gas Sensors and High Capacity Anode Materials in Lithium Ion Batteries. *The Journal of Physical Chemistry C*, 2010. **114**(44): p. 18753-18761.
112. Reddy, M.V., et al., α -Fe₂O₃ Nanoflakes as an Anode Material for Li-Ion Batteries. *Advanced Functional Materials*, 2007. **17**(15): p. 2792-2799.
113. Lin, Y.-M., et al., α -Fe₂O₃ Nanorods as Anode Material for Lithium Ion Batteries. *The Journal of Physical Chemistry Letters*, 2011. **2**(22): p. 2885-2891.
114. Yu, L., et al., TiO₂ nanotube arrays grafted with Fe₂O₃ hollow nanorods as integrated electrodes for lithium-ion batteries. *J. Mater. Chem. A*, 2013. **1**(1): p. 122-127.
115. Zhou, G., et al., A nanosized Fe₂O₃ decorated single-walled carbon nanotube membrane as a high-performance flexible anode for lithium ion batteries. *Journal of Materials Chemistry*, 2012. **22**(34): p. 17942.
116. Wang, G., et al., Synthesis and evaluation of carbon-coated Fe₂O₃ loaded on graphene nanosheets as an anode material for high performance lithium ion batteries. *Journal of Power Sources*, 2013. **239**: p. 37-44.
117. Han, F., et al., Rationally designed carbon-coated Fe₃O₄ coaxial nanotubes with hierarchical porosity as high-rate anodes for lithium ion batteries. *Nano Research*, 2014. **7**(11): p. 1706-1717.
118. Cai, X., et al., Facile synthesis of porous iron oxide rods coated with carbon as anode of high energy density lithium ion battery. *Electrochimica Acta*, 2016. **191**: p. 767-775.
119. Gao, L., et al., Hierarchical 3D TiO₂@Fe₂O₃ nanoframework arrays as high-performance anode materials. *Nanoscale*, 2014. **6**(12): p. 6463-7.
120. Chai, X., et al., Carbon-coated Fe₂O₃ nanocrystals with enhanced lithium storage capability. *Applied Surface Science*, 2015. **347**: p. 178-185.
121. Brandt, A. and A. Balducci, Ferrocene as precursor for carbon-coated α -Fe₂O₃ nanoparticles for rechargeable lithium batteries. *Journal of Power Sources*, 2013. **230**: p. 44-49.
122. Cho, J.S., Y.J. Hong, and Y.C. Kang, Design and Synthesis of Bubble-Nanorod-Structured Fe₂O₃-Carbon Nanofibers as Advanced Anode Material for Li-Ion Batteries. *ACS Nano*, 2015. **9**(4): p. 4026-35.
123. Challagulla, S., et al., Acrylate-based Polymerizable Sol–Gel Synthesis of Magnetically Recoverable TiO₂ Supported Fe₃O₄ for Cr(VI) Photoreduction in Aerobic Atmosphere. *ACS Sustainable Chemistry & Engineering*, 2016. **4**(3): p. 974-982.

124. Fei, H., et al., Preparation of carbon-coated iron oxide nanoparticles dispersed on graphene sheets and applications as advanced anode materials for lithium-ion batteries. *Nano Research*, 2015. **7**(4): p. 502-510.
125. Kontos, A.I., et al., Self-Organized Anodic TiO₂Nanotube Arrays Functionalized by Iron Oxide Nanoparticles. *Chemistry of Materials*, 2009. **21**(4): p. 662-672.
126. Xia, H., et al., Hierarchical TiO₂-B nanowire@ α -Fe₂O₃ nanothorn core-branch arrays as superior electrodes for lithium-ion microbatteries. *Nano Research*, 2014. **7**(12): p. 1797-1808.
127. Luo, Y., et al., Seed-assisted synthesis of highly ordered TiO₂@ α -Fe₂O₃ core/shell arrays on carbon textiles for lithium-ion battery applications. *Energy & Environmental Science*, 2012. **5**(4): p. 6559.
128. Zhu, Q., et al., Improving the lithium storage properties of Fe₂O₃@C nanoparticles by superoleophilic and superhydrophobic polysiloxane coatings. *Journal of Materials Chemistry*, 2012. **22**(31): p. 15894.
129. Chen, J.S., et al., Constructing hierarchical spheres from large ultrathin anatase TiO₂ nanosheets with nearly 100% exposed (001) facets for fast reversible lithium storage. *J Am Chem Soc*, 2010. **132**(17): p. 6124-30.
130. Bing, Z., et al., Electrochemical Characterization of a Three Dimensionally Ordered Macroporous Anatase TiO₂ Electrode. *Electrochemical and Solid-State Letters*, 2006. **9**(3): p. A101.
131. Xu, J., et al., Electrochemical properties of anatase TiO₂ nanotubes as an anode material for lithium-ion batteries. *Electrochimica Acta*, 2007. **52**(28): p. 8044-8047.
132. Zamparas, M., et al., Removal of phosphate from natural waters using innovative modified bentonites. *Applied Clay Science*, 2012. **62-63**: p. 101-106.
133. Valášková, M. and G.S. Martynková, Vermiculite: Structural Properties and Examples of the Use, *Clay Minerals in Nature - Their Characterization, Modification and Application*, D.M. Valaskova, Editor. 2012, InTech.
134. Bhattacharyya, K.G. and S.S. Gupta, Adsorption of a few heavy metals on natural and modified kaolinite and montmorillonite: a review. *Adv Colloid Interface Sci*, 2008. **140**(2): p. 114-31.
135. Bhattacharyya, K.G. and S.S. Gupta, Kaolinite, montmorillonite, and their modified derivatives as adsorbents for removal of Cu(II) from aqueous solution. *Separation and Purification Technology*, 2006. **50**(3): p. 388-397.
136. Grim, R.E., *Applied Clay Mineralogy*. 1962: McGraw Hill Press.

137. Murray, H.H., Chapter 2 Structure and Composition of the Clay Minerals and their Physical and Chemical Properties. 2006. **2**: p. 7-31.
138. Brady, N.C. and R.R. Weil, The nature and properties of soils. 15 ed. 2002: Pearson Education.
139. Chen, Q., et al., Iron pillared vermiculite as a heterogeneous photo-Fenton catalyst for photocatalytic degradation of azo dye reactive brilliant orange X-GN. Separation and Purification Technology, 2010. **71**(3): p. 315-323.
140. Pereira, P.R., J. Pires, and M. Brotas de Carvalho, Zirconium Pillared Clays for Carbon Dioxide/Methane Separation. 1. Preparation of Adsorbent Materials and Pure Gas Adsorption. Langmuir, 1998. **14**(16): p. 4584-4588.
141. Xianjia Peng, et al., Zirconia Pillared Montmorillonite for Removal of Arsenate from Water. Journal of Environmental Science and Health, Part A, 2010. **40**(5): p. 1055-1067.
142. Abollino, O., et al., Interaction of metal ions with montmorillonite and vermiculite. Applied Clay Science, 2008. **38**(3-4): p. 227-236.
143. Du, Z., et al., Selective and Fast Adsorption of Perfluorooctanesulfonate from Wastewater by Magnetic Fluorinated Vermiculite. Environ Sci Technol, 2017. **51**(14): p. 8027-8035.
144. Ren, X., et al., Adsorption of arsenic on modified montmorillonite. Applied Clay Science, 2014. **97-98**: p. 17-23.
145. Ohtsuka, K., Y. Hayashi, and M. Suda, Microporous zirconia-pillared clays derived from three kinds of zirconium polynuclear ionic species. Chemistry of Materials, 1993. **5**(12): p. 1823-1829.
146. Suzuki, K., et al., Preparation and Property of Zirconia-Pillared Montmorillonite Having Different Pillar Populations. Bulletin of the Chemical Society of Japan, 1991. **64**(2): p. 732-734.
147. Shannon, R.D., Revised effective ionic radii and systematic studies of interatomic distances in halides and chalcogenides. Acta Crystallographica Section A, 1976. **32**(5): p. 751-767.
148. Lin, J., et al., Evaluation of sediment amendment with zirconium-reacted bentonite to control phosphorus release. Environmental Earth Sciences, 2016. **75**(11).
149. Sun, K., et al., Modification of clays and zeolites by ionic liquids for the uptake of chloramphenicol from water. Chemical Engineering Journal, 2017. **313**: p. 336-344.
150. Huang, W.-Y., et al., Kinetics, isotherm, thermodynamic, and adsorption mechanism studies of La(OH)₃-modified exfoliated vermiculites as highly efficient phosphate adsorbents. Chemical Engineering Journal, 2014. **236**: p. 191-201.

151. Tian, S., et al., Enhanced adsorption removal of phosphate from water by mixed lanthanum/aluminum pillared montmorillonite. *Chemical Engineering Journal*, 2009. **151**(1-3): p. 141-148.
152. Dithmer, L., et al., Characterization of phosphate sequestration by a lanthanum modified bentonite clay: a solid-state NMR, EXAFS, and PXRD study. *Environ Sci Technol*, 2015. **49**(7): p. 4559-66.

Appendix: Supporting information for Chapter 2

Bragg reflection peak estimation

$$\lambda_{max} = \frac{2D\sqrt{2}}{\sqrt{3}} \sqrt{n_{eff}^2 - \sin^2\theta}$$

λ_{max} (nm) is stopband position for 1st order Bragg diffraction

n_{eff} is the average refractive index of photonic crystal.

D is pore size of 3DOM TiO₂

Assume incident angle of incident light with respect to surface normal, $\theta=0^\circ$.

$$n_{eff} = \sqrt{fn_{TiO_2}^2 + (1-f)n_{air}^2}$$

f is TiO₂ phase volume percentage, generally taken as 0.26

n_{TiO_2} is refractive index of TiO₂, for anatase taken as 2.5

n_{air} is refractive index of air, taken as 1.

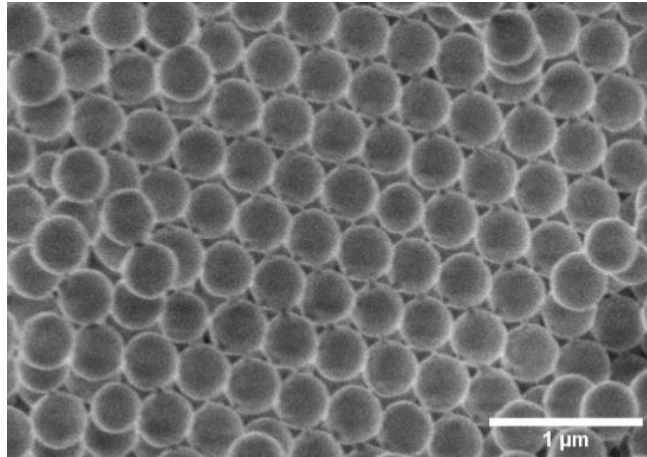


Figure S2-1 SEM image of PMMA template

PMMA (330 nm) spheres are uniform in size and effectively packed into face-centered-cubic (FCC) structure. Each colloidal particle is connected with 6 surrounding particles through 6 bridges on the two-dimensional plane.

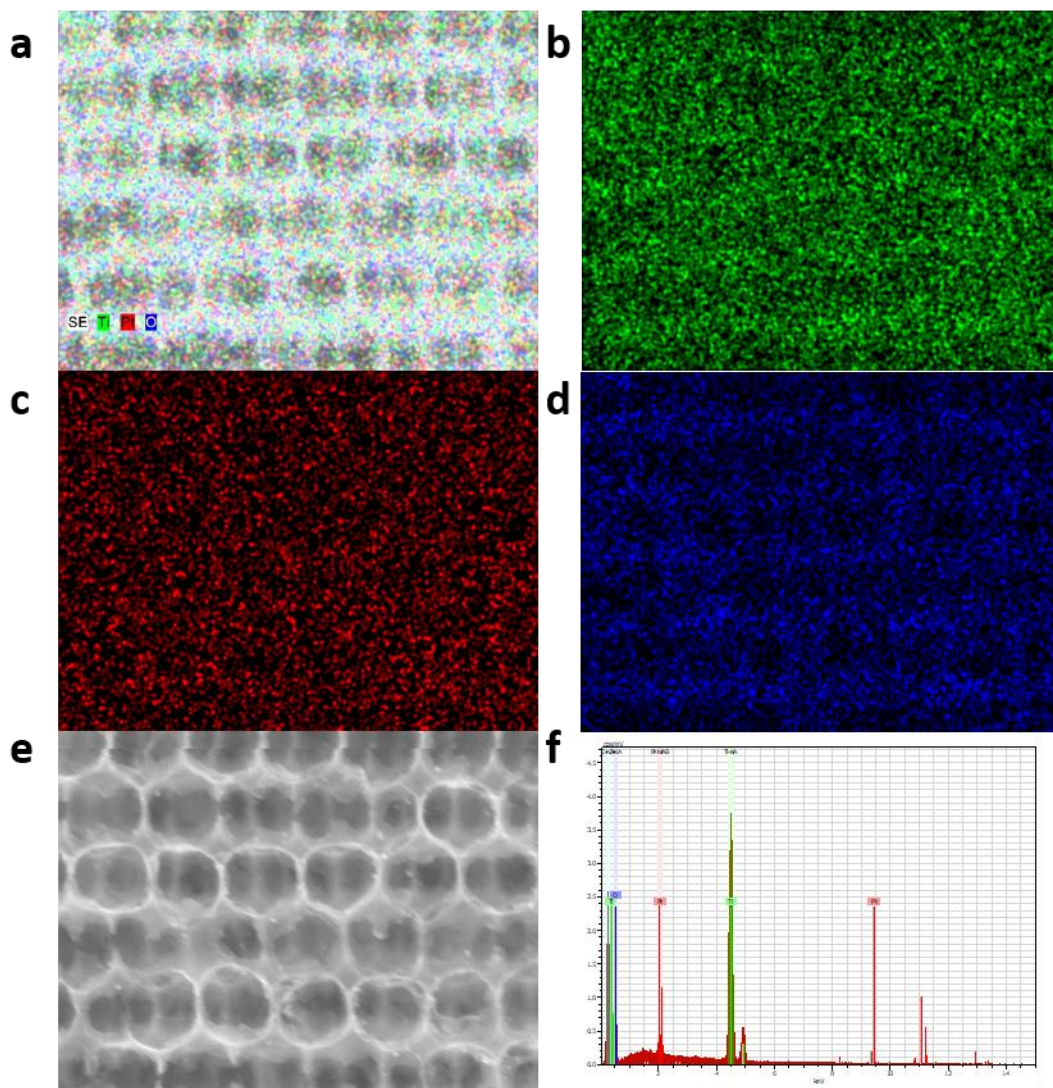


Figure S2-2 Elemental mapping of the Pt-TiO₂ composite. (a) Ti, Pt and O element mapping images, (b)-(d) Ti, Pt and O dispersion, respectively, (e) SEM image of Pt-TiO₂, (f) EDS element spectrum of Pt-TiO₂.

First order kinetic model

Table S2-1 Parameters of first order kinetic model for degradation of MO

Catalysts		Rate constant, $k \times 10^3$, min^{-1}	R^2
TiO ₂	$y=0.0021x+0.0037$	2.1	0.989
Pt-TiO ₂	$y=0.0032x+0.0291$	3.2	0.9783
rGO-TiO ₂	$y=0.0062x+0.0706$	6.2	0.9747
Pt/rGO-TiO ₂	$y=0.0129x+0.0762$	12.9	0.9925

Curriculum Vitae

Jingwan Huo

EDUCATION

- **University of Wisconsin-Milwaukee, Milwaukee, Wisconsin, USA**
Ph.D. Major in Mechanical Engineering, Minor in Civil Engineering 2018.5
Selected Courses: Intermediate Fluid Mechanics; Transport in Porous Media; Thermal Radiation and Conduction; Electron Microscopy Laboratory (SEM, TEM).
- **University of Wisconsin-Milwaukee, Milwaukee, Wisconsin, USA**
M.S. Major in Mechanical Engineering 2012.12
Selected Courses: Introduction to Water and Sewage Treatment; Freshwater Engineering; Water Quality Assessment; Transition Metal/organometallic.
- **Huazhong University of Science and Technology, Wuhan, Hubei, China**
B.S. Major in Chemical Engineering 2009.9

TECHNICAL SKILLS:

- **Material background:** Polymer, metal oxide, liquid, ceramic films, graphene, composite
- **Synthesis processes:** Atomic Layer Deposition (ALD); Solution processing (polymerization, hydrothermal, sol-gel, anodization)
- **Characterization:** Gas chromatography (GC, Agilent 7890A); X-ray diffractometer (XRD); Scanning electron microscopy (SEM)/Energy-dispersive X-ray Spectroscopy (EDS); Transmission electron microscopy (TEM); Raman spectrum; Inductively coupled plasma (ICP); UV-Vis Spectrometer; Scanning Mobility Particle Sizer Spectrometer (SMPS); High-performance Liquid Chromatography-Mass Spectrometer (HPLC-MS).
- **Computer based skills:** PTC Cero; LabView; Microsoft Office software.

RESEARCH EXPERIENCES:

Research Assistant University of Wisconsin-Milwaukee, Milwaukee, USA 2011.1 - Present

- Real time monitoring nanoparticle emissions from Al₂O₃ ALD process from Savannah S100 ALD system using SMPS. Optimization of operation conditions such as pulsing & purging time and temperature to minimize nanoparticles emissions and improve utilization of reaction precursors.
- Designed and synthesized novel TiO₂-based hybrid nanomaterials as photo-catalyst for dye photodegradation and anti-fouling membrane under visible-light illumination.
- Research on economic friendly inexpensive phosphorous adsorbent using clay and metal oxide- modified clay.
- Explored hybrid nanostructures alternative materials as anode for Lithium-ion batteries. By growing Fe₂O₃ on porous TiO₂, attained good cyclability and rate capability for Li-ion batteries.

Teaching Assistant University of Wisconsin-Milwaukee, Milwaukee, USA 2011.9 – 2017.5

- Experienced instructor in fundamental engineering labs, including Engineering Fundamentals I and II lab; How things works: Understanding Technology lab; and

Mechanical Engineering Experimentation lab. Students and instructors of classes were satisfied about the course and lab instruction.

- Hands-on helping student understanding basic engineering disciplines, data collection and analysis, sensor calibration, and software including Microsoft office, Matlab, PTC Cero, and LabView. Guide student through experiment design & planning and complete industrial projects from companies such as Master Lock.

Chemical Analyst Oil Crops Research Institute, Chinese Academy of Agricultural Science, Wuhan, China 2010.6 – 2010.12

- In charge of determination the composition of various fatty acids in rapeseeds, through esterification and extraction fatty acids and quantifying with Gas Chromatography (GC);
- Explored the method to determine molecular structure of fatty acids in rapeseeds using HPLC-MS;
- Be familiar with operations of GC and HPLC-MS.

Research Assistant Huazhong University of Science and Technology, Wuhan, China 2009.2 – 2010.6

- Modified multi-walls carbon nanotubes (MWCNs) by inorganic-coating (MgO and SiO₂) through sol-gel method. Improved heat conductivity of epoxy for ~200% by integrating inorganic-coated MWCNs into composites.
- Designed and research on SiO₂/polyacrylate paint nano-hybrid for abrasion-resistant paint.
- Characterization of inorganic-polymer hybrids using FTIR (especially Temperature-Dependant FTIR), DSC, TG, SEM, rheometer, abrasion test.

SELECTED PUBLICATIONS:

- **Huo, J.W.**, Lin, X., Yuan, C.* “Real-time Nano-particle Emission Measurement from Atomic Layer Depositions Nano-Manufacturing System”, Proceedings of 2012 ASME International Manufacturing Science and Engineering Conference, June 4-8, 2012, Notre Dame, IN.
- **Huo, J.W.**, Yuan, C.* “Nano-particle Emissions from Atomic Layer Deposition”, Abstract, Proceedings of IEEE Intl. Symposium on Sustainable Systems & Technology, May 16-18, 2012, Boston, MA.
- Gao, X.F., Guan, D.S., **Huo, J.W.**, Chen J.H., Yuan, C.* “Free Standing TiO₂ Nanotube Array Electrodes with Ultra Thin Al₂O₃ Barrier Layer and TiCl₄ Surface Modification for High Efficiency Dye Sensitized Solar Cells”, *Nanoscale*, 5, 2013, 10438-10446.